Exploring Topology and Shape Optimisation Techniques in Underground Excavations

Kazem Ghabraie
M.Sc., B.Sc.

A thesis submitted in fulfilment of the requirements for the degree of Doctor of Philosophy

School of Civil, Environmental and Chemical Engineering
Science, Engineering and Health (SEH) Portfolio
RMIT University

August 2009

یک چند به کودکی به استاد شدیم　　یک چند به استادی خود شاد شدیم

پایان سخن شنو که ما را چه رسید　　از خـاک بر آمدیم و بر باد شـــدیم

حکیم عمر خیام

Once attending schools as students
Once being proud of becoming teachers
But: coming from dust and going with wind
Are our stories' common rigid features.

Omar Khayyám (1048–1131 AD):
Iranian mathematician, astronomer, philosopher, physician, and poet

Translated by: Kazem Ghabraie

Declaration

I certify that except where due acknowledgement has been made, the work is that of the author alone; the work has not been submitted previously, in whole or in part, to qualify for any other academic award; the content of the thesis is the result of work which has been carried out since the official commencement date of the approved research program; any editorial work, paid or unpaid, carried out by a third party is acknowledged; and, ethics procedures and guidelines have been followed.

Kazem Ghabraie

August 14, 2009

Acknowledgements

I would like to deeply thank my dear mother and my dear father for their devotional support throughout my life from the very first second to the present moment. I would like to sincerely thank my dear wife for her support and her patience during my course of study which covers all of our mutual life till now.

I wish to express my warm thanks to my senior supervisor, Professor Mike Xie, who helped me not only in my research but also in stabilising a new life in a new country. Special thanks should go to Dr. Abbas Mohajerani for his invaluable support and advice. I would like to warmly thank Dr. Xiaodong Huang, my second supervisor, for the beneficial discussions we had. I also wish to thank Dr. Gang Ren, for his helpful advice.

I would like to gratefully acknowledge the financial support of the RMIT University.

Finally, I wish to thank a group of people whom I never met but have widely used their products, the Gnu team, the Ubuntu team, the LaTeXgroup, the Inkscape group, the Octave team, among the others who are providing free open source software packages to the community.

Contents

Nomenclature

Scalars

$\hat{\alpha}_i$	Filtered sensitivity numbers
α_i	Sensitivity number of the i-th element
ν	Poisson's ratio
ϕ	Friction angle of soil
ϕ_d	Friction angle for discontinuities
ψ	Dilation angle of soil
ρ_i	Relative density of the i-th element
$\bar{\sigma}$	Mean principal compressive stress
σ_i^{vm}	Von Mises stress in the i-th element
σ_1	Maximum principal stress
σ_2	Medium principal stress
σ_3	Minimum principal stress
σ_n	Normal stress

σ_{th}	Threshold stress level in the ESO method
τ	Shear stress
θ_i	Orientation of the hole in the i-th microcell
a_i	Size of the hole in the i-th microcell
b_i	Size of the hole in the i-th microcell
c	Cohesion of soil
m	Move limit
m_s	Stabilisation move limit
p	Penalty factor in the power-law material interpolation scheme
q	Penalty factor in the alternative material interpolation scheme
r_f	Filtering radius
x_i	i-th design variable
E	Young's modulus (the modulus of elasticity)
E^O	Modulus of elasticity of the original rock
E^R	Modulus of elasticity of the reinforced rock
E^V	Modulus of elasticity of a very weak material representing voids
$E^{(1)}$	Modulus of elsticity of the first material
$E^{(2)}$	Modulus of elsticity of the second material

E_i Modulus of elasticity of the i-th material

ER Evolution rate in the ESO method

G Shear modulus

I_{slp} Slippage indicator for cracked elements

I_{spr} Separation indicator for cracked elements

K Iteration number

N Number of elements

PI Performance index in the ESO and BESO methods

RL Rejection level in the proposed ESO method

RR Rejection ratio in the ESO method

$\bar{V}$ Maximum allowable volume of materials in a design

$\bar{V}_R$ Predefined volume of the reinforced area in the rock mass

$\bar{V}_V$ Predefined volume of the opening

V_i Volume of the i-th element

VR Volume removal rate in the ESO method

Fields

ρ Field of relative densities

f Body forces field

t Displacement field

u Surface tractions field

x Field of topological design variables

Functions

c Mean compliance function

f General function, The yield function

g General function, The plastic potential function

h Floor heave

v Tunnel convergence

$\mathfrak{L}$ Lagrangian functional

Operators

$|\cdot|$ Absolute value of a parameter

$\cdot^T$ Transpose of a vector or matrix

$\nabla\cdot$ Gradient of a function with respect to design variables

Sets

Ω Part of the design domain filled with material

Ω' Void part of the design domain

$\mathcal{A}$ Active set

$\mathcal{B}_h$ Boundary of the opening

$\mathcal{B}_s$ Smoothed boundary segments

$\mathcal{F}$ Front layer

$\mathcal{M}$ Set of solid elements

$\mathbb{R}$ Set of all real numbers

$\mathcal{U}$ Space of kinematically admissible displacement fields

$\mathcal{V}$ Set of void elements

$\mathcal{X}$ Set of admissible design variables

Tensors

ϵ_{ij} Linearised strain tensor

σ_{ij} Stress tensor

$\bar{E}_{ijkl}$ Elasticity tensor of the base material

E^H_{ijkl} Homogenised elasticity coefficients of microcells

E_{ijkl} Stiffness tensor

Vectors and Matrices

ξ Geometrical coordination

$\mathbf{f}$ Nodal force vector

$\tilde{\mathbf{f}}$ Auxiliary force vector used to define the floor heave or tunnel convergence functions

$\mathbf{u}$ Nodal displacement vector

$\mathbf{u}_i$ Nodal displacement vector of the i-th element

$\mathbf{x}$ Vector of design variables

$\hat{\mathbf{K}}_i$ Global level stiffness matrix of the i-th element

$\mathbf{K}$ Stiffness matrix of the system

$\mathbf{K}_i$ Local level stiffness matrix of the i-th element

Abbreviations

BESO Bidirectional Evolutionary Structural Optimisation

GSI Geological Strength Index

KKT Karush-Kuhn-Tucker conditions

OCR Overconsolidation Ratio

Q Tunnelling Quality Index

RMR Rock Mass Rating

RQD Rock Quality Designation

SCB Short Cantilever Beam

SIMP Solid Isotropic Microstructures (Material) with Penalisation

Abstract

Topology optimisation techniques help designers to find the best layout of structural members. When followed by shape and sizing optimisation, these techniques result in far greater savings than shape and sizing optimisation alone. During the last three decades extensive research has been carried out in the topology optimisation area. Consequently topology optimisation techniques have been considerably improved and successfully applied to a range of physical problems. These techniques are now regarded as invaluable tools in mechanical, aerostructural and structural design.

In spite of great potential in geomechanical problems, however, the application of topology optimisation techniques in this field has not been studied thoroughly. This thesis explores the state-of-the-art topology and shape optimisation methods in excavation design. The main problems of concern in this thesis are to find the optimum shape of an underground opening and to optimise the reinforcement distribution around it. To tackle these problems, new formulations for some topology optimisation techniques are proposed in this thesis to match the requirements in excavation problems.

Although linear elastic material models have limited applications in excavation design, these models are used in the first part of this thesis to introduce the proposed optimisation technique and to verify it. Simultane-

ous shape and reinforcement optimisation is considered as well. Using the proposed optimisation techniques, it is shown that the computational effort needed for this mixed optimisation problem is almost the same as the effort required to solve each of shape or reinforcement optimisation problems alone.

In the next part of this thesis, reinforcement optimisation of tunnels in massive rocks is addressed where the behaviour of the rock mass is influenced by few major discontinuities. Although discontinuities exist in the majority of rock masses, due to its complexities, optimising the excavations in these types of rocks has not been considered by any other researcher before. A method for reinforcement optimisation of tunnels in such rock masses is proposed in this thesis and its capability is demonstrated by means of numerical examples.

Lastly, shape optimisation of excavations in elasto-plastic soil is addressed. In this problem the excavation sequence is also taken into account. A stress-based parameter is defined to evaluate the efficiency of the soil elements assuming Mohr-Coulomb material model. Some examples are solved to illustrate and verify the application of the proposed technique.

Being one of the first theses on the topic, this work concentrates on the theoretical background and the possibility of applying topology optimisation techniques in excavation designs. It has been demonstrated that a properly tailored topology optimisation technique can be applied to find both the optimum shape and the optimum reinforcement design of openings. Optimising the excavations in various types of grounds including elastic homogeneous rock masses, massive rocks, and elasto-plastic soil and rock media have been considered. Different objective functions, namely, mean compliance, floor heave, and tunnel convergence have been selected and successfully

minimised using the proposed techniques. The results obtained in this thesis illustrate that the proposed topology optimisation techniques are very useful for improving excavation designs.

CHAPTER 1

Introduction

The goal of engineering is economical; its method is scientific. The goal and the method clearly place engineering in a position between economics and science.

Greber 1966

1.1 Optimisation and engineering

Science's goal is understanding natural phenomena and ultimately predicting future of a system given its current situation. In scientist's point of view when such a prediction is possible the problem is no more a problem. However in the engineering world it is just after this level when comes the *real* engineering task: dealing with problems like environmental considerations, practicability, and profitability. which all are directly or indirectly connected to economical issues. In the world, the resources are limited while the demand is increasing. Nowadays unlike old ages, economical considerations limit us more than our shortage of knowledge. If we don't construct a 5000m tall sky-scraper it is usually not because we don't know how to design it but mainly because of economical, social, and environmental issues which can all be translated in a

form of "cost".

In translating physical phenomena to mathematical language one usually ends up with a partial differential equation or simply a PDE. Economical considerations in engineering, on the other hand, usually manifest themselves as optimisation problems. In design process the engineer should seek for the best possible solutions which need the least resources, yet respond well. This process can be translated as a constrained optimisation where the goal is to minimise or maximise a function or a group of functions subject to some limitations. Solving optimisation problems are hence at the very heart of engineering practise. Optimisation problems do not appear only in designing. An engineer might come across optimisation problems in other engineering practises such as construction and maintenance as well.

In civil engineering, just like the other fields of engineering, optimisation has been widely used to improve designs. Selecting the best route for a road between two cities, designing the stiffest structure under certain loading conditions, and finding the best system to support a pre-stressed concrete bridge, are few examples of the application of optimisation in civil engineering discipline.

Dating back to the time of Newton, optimisation is not a new field. However the development of the state-of-the-art optimisation techniques is due to the revolutionary advancement of the high-speed computers (Rao 1996). Nowadays there are several optimisation techniques available, each having its own benefits and limitations, is suitable for special kind of problems. Genetic algorithms (GA) for instance, can usually yield the global optimum, but are computationally very expensive to implement. Linear programming

techniques, as another example, although fast and easy to implement, are only suitable for a very limited type of problems. Therefore deciding which method to use is an important part of solving an optimisation problem.

1.2 Different levels of optimisation

Pahl and Beitz (1988) divide the design process into four main phases, namely: Clarification of the task, Conceptual design, Embodiment design, and Detail design.

The first phase involves information collection and defining specifications and/or requirements. In conceptual design stage one should establish the function structure, combine suitable solution principles into concept variants, and finally select the best solution concept. In embodiment design phase, starting from the concept, the designer should select the best preliminary layout and then provide a definitive layout by optimising the forms. The final stage consists of selecting the best dimensions, arrangements, and forms of individual components (Pahl and Beitz 1988).

Similar to design process, the optimisation process can also be divided into different levels. In the conceptual and embodiment design phases one may use *Topology Optimisation*. Topology optimisation aims to find the best topology, layout or configuration of the members within a basic design domain fulfilling some constraints and limitations. After this level one can employ *Shape Optimisation* methods in order to find the best shapes and forms of the components of the system within the predefined topology which

has been found in previous stages. In detail design stage *Sizing Optimisation* methods can be found useful in order to find the optimum dimensions of the components whose shapes have already been selected (Hassani and Hinton 1999).

In simple words, sizing optimisation tries to find the best dimensions of members with fixed shapes. Shape optimisation helps the designers to find the best shape of members within a fixed topology. And topology optimisation tries to find the best topology within a design domain. A schematic illustration of the concept of these three levels of optimisation in a structural system is depicted in Figure 1.1.

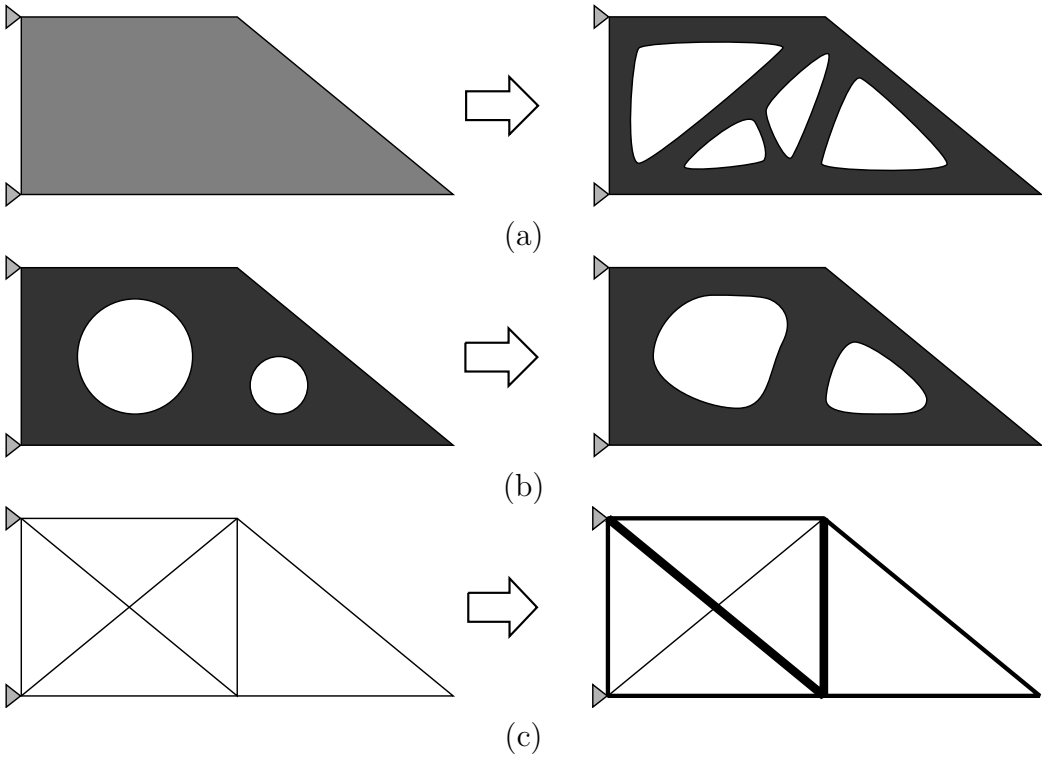

Figure 1.1 The three levels of optimisation: a) Topology optimisation; b) Shape optimisation; c) Sizing optimisation.

The considerable improvements in computational abilities of digital computers has changed the traditional trial and error design process drastically. Several numerical optimisation techniques have since been developed and improved continuously (Hassani and Hinton 1999; Ghabraie 2005). In structural design, among different levels of optimisation, sizing optimisation problems have been studied earlier. Finding the best cross area of a member in a truss or optimising the dimensions of the cross section of an I beam are examples of applying sizing optimisation in structural design. This was followed by research studies on shape optimisation techniques. Problems like finding the best shape of a hole in a loaded plate have been tackled by implementing shape optimisation techniques. Topology optimisation techniques, due to the complexity of the topology optimisation problems, have been developed more recently. Nevertheless in the past 20 years these techniques have attracted great attention and numerous research papers have been published in this area. Finding the best topology of a short cantilever beam in a rectangular design domain is one of the classical problems that can be solved by state-of-the-art topology optimisation techniques in structural design. Apart from structural engineering, topology optimisation techniques have been also used in material design, designing MicroElectroMechanical Systems (MEMS), and wave propagation problems among others (Bendsøe and Sigmund 2003). Most of the topology optimisation techniques can also be applied to shape optimisation or even sizing optimisation problems.

1.3 Topology optimisation in geomechanics

In geomechanical design there are many cases where topology or shape optimisation may be found helpful. Finding the best shape of an underground excavation to maximise stability, optimising the shape of the clay core of an earth dam to minimise seepage, and finding the best layout of piles in a raft-pile foundation minimise settlement are just few examples showing the potential applicability of topology and shape optimisation techniques in geomechanical engineering. Despite this great potential, however, only a few works have explored the application of these optimisation methods in geomechanics.

In underground excavations, just recently, a few attempts have been made to optimise the shape of the opening or the reinforcement around it. Ren et al. (2005) employed the Evolutionary Structural Optimisation (ESO) method to optimise the shape of underground openings. Yin et al. (2000) optimised the reinforcement topology around an underground tunnel using a method called the homogenisation method. Yin and Yang (2000a) used another topology optimisation method named Solid Isotropic Material with Penalisation (SIMP) to find the best reinforcement design of tunnels in layered geological structures. This approach was also used by Yin and Yang (2000b) to minimise tunnel heaves. Liu et al. (2008) addressed a similar problem using a different method. They implemented fixed grid finite element framework and used Bidirectional Evolutionary Structural Optimisation (BESO) technique to solve their optimisation problem. A review of these research works is presented in Chapter 3. Before that, the numerical methods used in these

studies are covered in detail in Chapter 2.

Applying topology and shape optimisation techniques to geomechanical design problems is not as straightforward as in structural design problems. The complex behaviour of natural materials like rock and soil, compared to well-known behaviour of manufactured materials, introduces modelling problems in finite element analysis. The existence of discontinuities such as joints, fractures, and bedding planes makes the rock mass anisotropic and inhomogeneous. The loading sequence can also be quite different in geotechnical problems in comparison to structural design. In structural design the members are manufactured into their final shapes before being installed and taking the loads. In excavation design, on the other hand, a change in the shape of the opening, during the excavation process, causes stress relief in the surrounding ground and thus alters loading conditions.

There are also some convergency and stability issues in topology and shape optimisation techniques especially when one deals with two-material design problems. This is the case for reinforcement optimisation of a tunnel where the two material phases are the host rock and the reinforced rock. Controlling these numerical instabilities can be difficult and need special considerations.

In this thesis these difficulties are addressed and some approaches are proposed to overcome them. Attempts are made to improve the shortcomings of the aforementioned initial research works and possibly take a further step in applying the state-of-the-art topology and shape optimisation techniques in geotechnics. However this area is still very new and this work is not claiming to cover the whole or even a major part of it. Geotechnical engineers

might find the numerical models too simplified or the optimisation methods too theoretical for practical use. It needs to be noted, however, that in the first step one has no choice rather than dealing with the most simplified problems leaving the complicated ones to after further studies. This thesis tries to propose a systematic approach to tackle the complexities involved in excavation design problems. The author believes that following the proposed approach it is possible to optimise more complicated and detailed models. It is hoped that this work will open a path to more comprehensive and more practical research studies in this area in the future.

1.4 Layout of the thesis

The next chapter introduces the state-of-the-art topology and shape optimisation techniques. Different methods in the literature are explained with special emphasis on the more commonly used material distribution based methods. The chapter addresses advantages and disadvantages of different techniques.

The third chapter provides an overview of underground excavation design. The usual techniques are reviewed and the issues regarding the numerical modelling of the problems are discussed. At the end of the chapter the previous works in applying topology optimisation techniques in underground excavation design are reviewed.

The fourth chapter discusses the special requirements in excavation design problems and proposes a topology optimisation techniques tailored to

match these requirements. Some improvement to overcome numerical instabilities in multi-material design problems are presented in this chapter. Considerations for shape optimisation problems are discussed. The effect of different algorithmic parameters are investigated as well.

The remaining chapters are devoted to the results achieved by implementing the proposed techniques. This starts from the simplest problems and gradually some complexities are introduced. Shape and reinforcement optimisation of tunnels in linear elastic ground, reinforcement optimisation of excavations in massive rocks with discontinuities, and optimising the shape of underground openings in elaso-plastic soil are the key problems which are covered.

CHAPTER 2

Topology optimisation techniques

The art of structure is how and where to put holes.

Le Ricolais 1973

2.1 Brief history

Topology optimisation techniques can be divided into two groups (Rozvany 2001; Eschenauer and Olhoff 2001):

- ▷ Topology optimisation of truss-like structures where the material volume is far smaller compared to the size of the design domain (low volume fractions) and the design domain is of discrete nature
- ▷ Topology optimisation of continuum structures where the material volume is a considerable ratio of the design domain (higher volume fractions) and the design domain is continuous

The earlier studies were focused on the former class. Dating some one and a half century back, Culmann (1866) tried to find the optimum layout of trusses to carry specified loads (Prager 1974). More than a hundred years back Michell (1904) laid down the principles of topology optimisation of structures

with very low volume fractions. His theory describes the optimum layouts of a truss-like continuum with infinite bars of infinitesimal size minimising the weight. After nearly seven decades Michell's theory was generalised and significantly improved by works of Prager (1969, 1974), Rozvany (1972a,b), and Rozvany and Prager (1976).

Layout optimisation in continuum structures started with works of Cheng and Olhoff (1981) on solid elastic plates. This was followed by some research studies on optimising elastic perforated plates by e.g. Lurie et al. (1982) and Kohn and Strang (1986). In these works non-homogeneous perforated microstructures were used to model the design domain. The material characteristics and orientation of these microstructures were taken as control variables.

Yet no practical approach to topology optimisation was proposed until two decades ago when Bendsøe and Kikuchi (1988) introduced their method. They used the homogenised properties of microstructures in finite element analysis and reduced the topology optimisation problem to a sizing optimisation problem. A different and simple FE-based topology optimisation technique was then proposed by Xie and Steven (1993). This method employed an evolutionary procedure to gradually remove the inefficient parts of the design domain. These two works started a new era in state-of-the-art topology optimisation and attracted numerous researchers to the field. Since then topology optimisation techniques have been developed and grown rapidly until now.

In geomechanical problems the design domain is a continuum, hence topology optimisation of truss-like structures will not be used or explained

in this thesis.

2.2 Defining topology

In topology optimisation the topology of the design domain should change. This means the produced shapes should have the freedom to be not homeomorphic to each other. Hence using conventional methods in shape optimisation, like changing the boundaries, can not be used in topology optimisation. In topology optimisation of continuum structures the design variables are selected in such a way that without the need of substantial re-meshing different topologies can be achieved by changing these variables. To define the topology of continuum structures, two approaches are mainly used (Ghabraie 2005). The first approach is to use material properties as control variables. In this case the topology can be defined by the material distribution. In the second approach a surface (or a hyper-surface in three dimensional problems) is defined over the design domain. A cut-off plane will pass this surface at a certain level. The topology is then defined as the projection of the parts of the surface above the cut-off plane on the design domain. These approaches are discussed in the next two sections.

2.2.1 Topology as material distribution

Defining topology as material distribution was the first and is still the most common approach to define the topology. The first two pioneering works of Bendsøe and Kikuchi (1988) and Xie and Steven (1993) were both based on

this approach.

In this approach a function or a group of functions are defined on a fixed design domain. These functions specify the material properties (usually modulus of elasticity) of every point in this fixed domain based on the values of design variables. We refer to these functions as *material distribution functions*. In special cases these functions may be referred to as *material interpolation schemes* (Bendsøe and Sigmund 1999; Stolpe and Svanberg 2001). If modulus of elasticity of a point approaches zero it can be deduced that there is no material in that point. Or there is a hole in that location. Hence this approach has the ability to change the topology of the design domain without re-meshing. In this approach, modifications in design variables will change the material distribution over the domain of interest. That is why this approach is known as material distribution.

Different classes of topologies can be achieved via material distribution definition. Rozvany (2001) has divided these topologies into three categories, i.e. Isotropic-Solid/Empty (ISE), Anisotropic-Solid/Empty (ASE), and Isotropic-Solid/Empty/Porous (ISEP) topologies.

ISE topologies

Suppose that a given domain is discretised into a finite number of cells. In an ISE topology each of these cells can either be empty or filled with an isotropic material. There are also the cases of multi-material design problems where the filling material can be chosen from two or more available materials. Note that within a domain containing a finite number of elements, the number of

possible ISE topology designs is a finite number.

Figure 2.1 shows some possible ISE topologies for a simple design domain. The domain consists of 3×5 similar elements. The 5 elements on the left edge have their left nodes fixed. A vertical point load is applied on the mid-point of the right edge of the middle element in the right side of the domain (Fig. 2.1a). The amount of material to be used is restricted to one-third of the domain's size (or 5 elements). The objective is to minimise the displacement of the loaded point.

The solution depicted in Figure 2.1b is infeasible as it will not transmit the load to the given support. Solutions illustrated in Figure 2.1c-f are all feasible and Figure 2.1c is the optimal solution.

The mathematical expression of this minimisation problem can be stated as

$$\min_{x_1,x_2,\ldots,x_N} \quad u_2^f \tag{2.1a}$$

$$\text{such that} \quad \sum_{i=1}^{N} x_i v_e = 5v_e; \tag{2.1b}$$

$$E_i = x_i E_m, \qquad i = 1, 2, \ldots, N \tag{2.1c}$$

$$x_i \in \{0, 1\}, \qquad i = 1, 2, \ldots, N \tag{2.1d}$$

where u_2^f is the second component (vertical component) of the displacement at the loaded point (the objective function). N is the number of elements (here 15). The statement in (2.1d) states that the design variables $x_1, x_2, \ldots, x_N$ can take binary values of 0 or 1. In (2.1c) E_m is the modulus of elasticity of the considered isotropic material. Here the modulus of elasticity

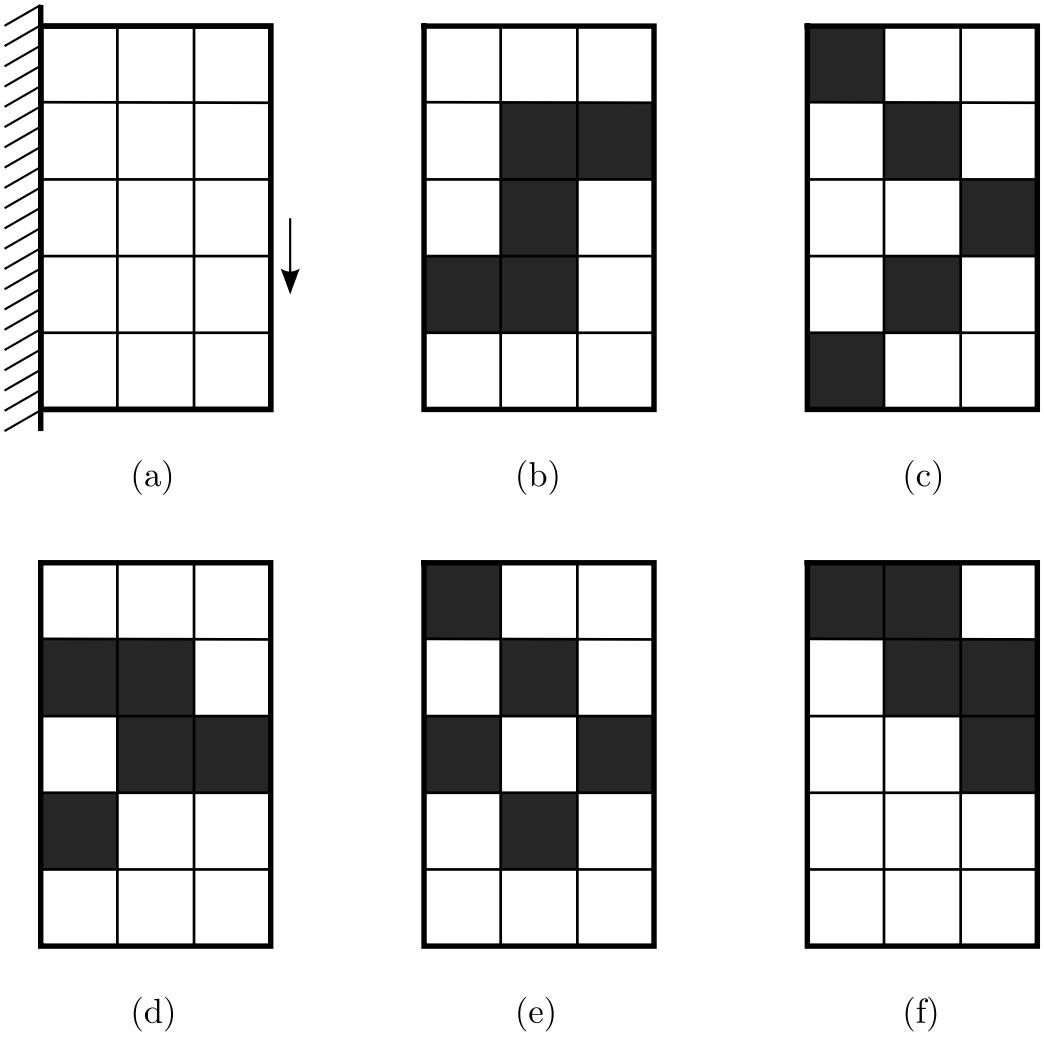

Figure 2.1 An example showing some possible ISE topologies for a simple problem: a) problem statement; b) an infeasible design; c) optimal design; d-f) three feasible but non-optimal solutions.

of the i-th element (E_i) is defined as a function of the element's design variable (x_i). This function is the material distribution function in this problem. By looking at (2.1c) and (2.1d) one can state that the values of 0 and 1 for the design variables are associated to void and filled elements respectively. The equality condition in (2.1b) restricts the volume of the using material to the volume of 5 elements. In this expression v_e is the volume of a single element.

ASE topologies

If the material in use is not isotropic, one will end up in an ASE topology. In this class the number of changing material properties within each element are more than one. The material orientation and the components of the rigidity tensor E_{ijkl} need to be specified in each solid element. A schematic ASE solution for the simple problem in Figure 2.1a is illustrated in Figure 2.2.

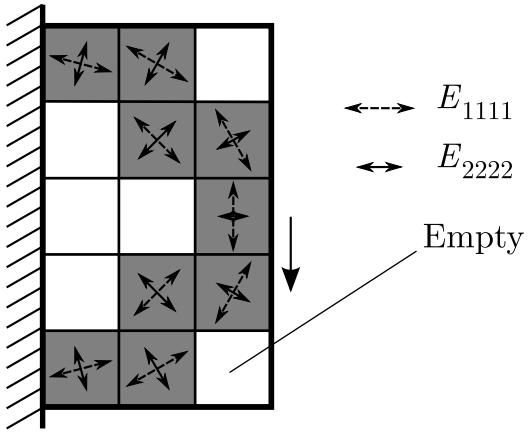

Figure 2.2 An example showing an ASE topology.

The mathematical expression of the problem involving ASE topologies

will take the following form

$$\min_{\substack{x_1,x_2,\ldots,x_N \\ y_1,y_2,\ldots,y_N \\ z_1,z_2,\ldots,z_N}} u_2^f \tag{2.2a}$$

$$\text{such that} \quad \sum_{i=1}^{N} v_i \leq \bar{v}; \tag{2.2b}$$

$$E^i_{klmn} = f_{klmn}(x_i, y_i, z_i), \qquad i = 1, 2, \ldots, N \tag{2.2c}$$

$$\theta^i = g(x_i, y_i, z_i), \qquad i = 1, 2, \ldots, N \tag{2.2d}$$

$$\begin{cases} x_i \in [x_{min}, x_{max}] \\ y_i \in [y_{min}, y_{max}] \\ z_i \in [z_{min}, z_{max}] \end{cases}, \qquad i = 1, 2, \ldots, N \tag{2.2e}$$

In ASE class the number of design variables are greater than the number of elements. Here for any element i three independent design variables have been assumed (i.e. x_i, y_i, z_i). The volume constraint is defined in (2.2b). An inequality condition has been used which states that the volume of the material used should not exceed the predefined value of $\bar{v}$. The equations (2.2c) and (2.2d) define the material distribution functions. θ^i is the orientation of the material within element i and E^i_{klmn} are entries of the element's rigidity tensor. Note that in general case any material property in an element is a function of all design variables of that element. However it is straightforward to assume that each design variable is controlling a specific material property. For example one can assume $E^i_{1111} = f_1(x_i)$, $E^i_{2222} = f_2(y_i)$, and $\theta^i = g(z_i)$. The conditions in (2.2e) are usually referred to as *box constraints*. These conditions define the minimum and maximum of each controlling variable.

In ASE topologies at least one variable (orientation) need to change continuously. Hence the number of definable ASE topologies for a problem (even with finite number of elements) is infinite.

ISEP topologies

One might use an isotropic material to build some *microstructures* with some holes inside them. Then instead of filling elements with the solid material these porous microstructures can be used as filling material. In this case the mechanical properties of the filled elements can be calculated through *homogenisation theory*. Apparently the elements in macroscopic scale will not be necessarily isotropic any more. The resulted topology is then an ISEP topology. An example of ISEP topologies is shown in Figure 2.3.

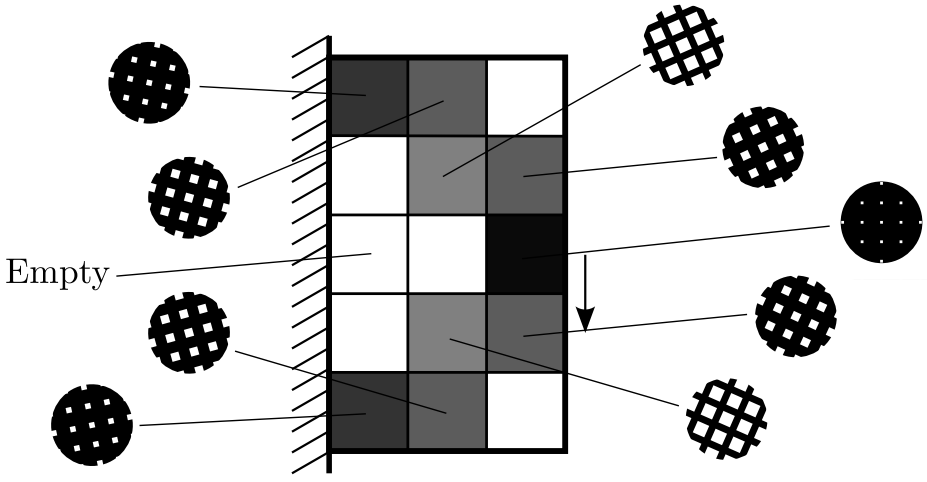

Figure 2.3 An example showing an ISEP topology.

In this figure it is assumed that the microscale holes are of square shape.

The mathematical representation of the problem then can be expressed as

$$\min_{\substack{a_1,a_2,\ldots,a_N \\ \theta_1,\theta_2,\ldots,\theta_N}} u_2^f \tag{2.3a}$$

$$\text{such that} \quad \sum_{i=1}^{N} v_i \leq \bar{v}; \tag{2.3b}$$

$$E^i_{klmn} = f_{klmn}(a_i), \qquad i = 1, 2, \ldots, N \tag{2.3c}$$

$$\begin{cases} a_i \in [0, \bar{a}] \\ \theta_i \in [-\frac{\pi}{2}, \frac{\pi}{2}] \end{cases}, \qquad i = 1, 2, \ldots, N \tag{2.3d}$$

where a_i and θ_i are the microscale hole dimension and the orientation of the microstructures in the i-th element respectively. Here the orientations themselves have been taken as design variables. The material distribution functions are defined in (2.3c). In the box constraints (2.3d) the lower limit of 0 for a represents the solid case. The upper limit $\bar{a}$ is associated to the case when the hole expands to the whole microstructure and hence represents void. In intermediate values a porous material will be resulted. Note that in ISEP topologies the design variables are continuous, so like ASE class, an infinite number of topologies are imaginable.

2.2.2 Topology as a level set

Another way of defining topology is using level set model (Wang et al. 2003; Yulin and Xiaoming 2004; Belytschko et al. 2003). Having a scalar function ϕ a *level set* of this function is a set defined by $L_f(k) = \{x|\phi(x) = k\}$ where k is a constant. In a three dimensional domain $\phi : \mathbb{R}^3 \mapsto \mathbb{R}$ and any level set

defines a surface which is referred to as iso-surface, implicit surface, or level set surface. k is known as iso-value (Wang et al. 2003).

Suppose that the function ϕ is defined on the domain $\mathcal{D}$. For any value of k the related iso-surface can divide this domain into a partition. For $k = 0$ one can write

$$\begin{aligned} \Omega &= \{x|\phi(x) < 0\} \\ \partial\Omega &= \{x|\phi(x) = 0\} \\ \Omega' &= \{x|\phi(x) > 0\} = \mathcal{D} \setminus (\Omega \cup \partial\Omega) \end{aligned} \tag{2.4}$$

The area covered by Ω is filled with a material while Ω' represents void. The surface (or curve in two dimensional cases) defines the boundary of the solid part. Now by defining ϕ as a function (implicitly or explicitly) of design variables, a change in these variables can result in a different topology. Figure 2.4 shows the idea of using level sets to define different topologies.

In level set approach materials in use are usually isotropic. Theoretically ISE topologies can be also obtained by using level sets (Fig. 2.5). However note that in this case the function ϕ is not continuous over the design domain.

Compared to level sets approach, defining topology using material distribution is much easier to implement. The variety of topologies covered by material distribution approach and the flexibility of this approach in dealing with different types of materials can also be considered as an important advantage. Moreover topology optimisation techniques based on material distribution are more developed and more practical. Most of these techniques can be easily linked to available finite element analysis packages. On

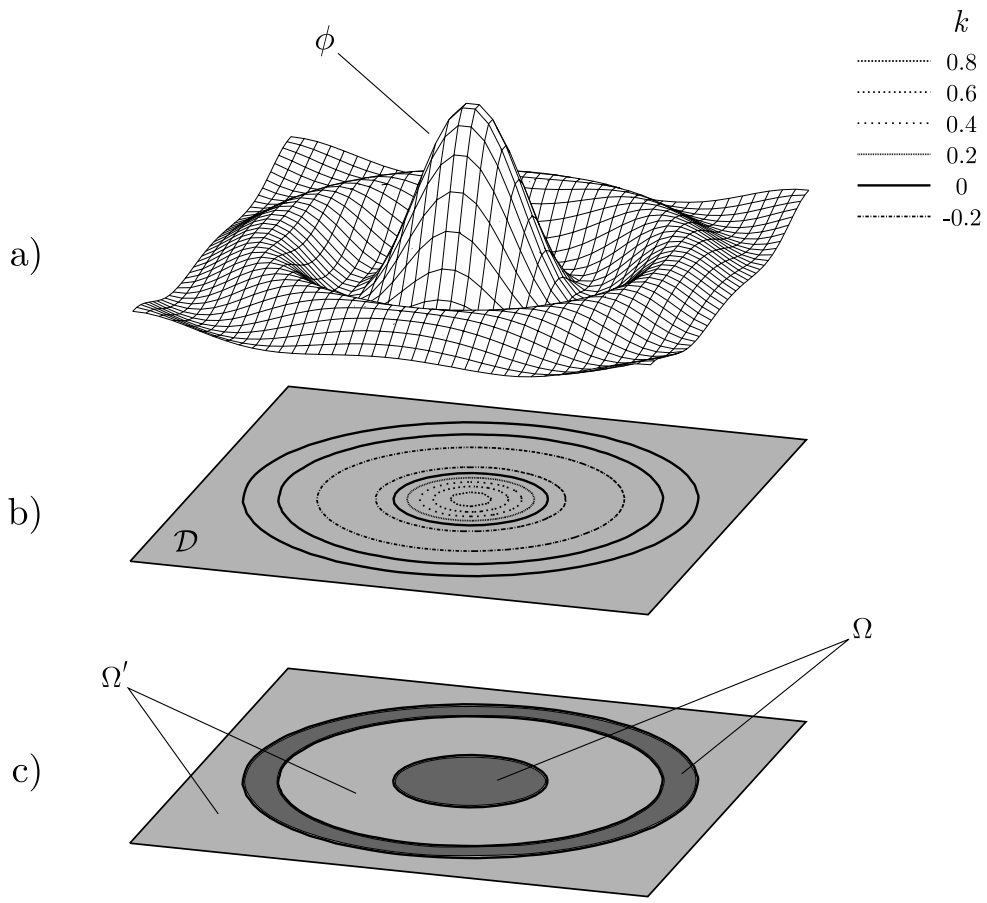

Figure 2.4 Defining topology using a level set model: a) the function ϕ; b) the domain $\mathcal{D}$ and the level sets for different iso-values; c) the sets Ω and Ω' and the final topology

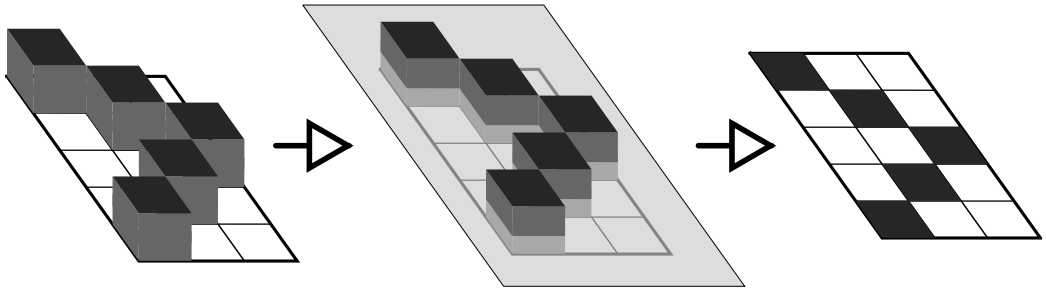

Figure 2.5 Defining an ISE topology using level set approach: a) the *noncontinuous* function ϕ; b) the level set is the intersection of $z = \phi$ and $z = k$; c) the final topology.

the other hand level set methods are relatively complex and have more limitations. Because of these reasons in this thesis the material distribution approach is followed. Some very popular topology optimisation techniques which all treat the topology problem using material distribution approach are presented later in this chapter. But before that we look at solution methods for topology optimisation problems.

2.3 Solution methods for optimal topology problems

Using material distribution approach the topology optimisation problem can be converted into a sizing optimisation problem over a fixed design domain (Bendsøe and Sigmund 2003). However the number of design variables in topology optimisation problems are substantially larger compared to usual sizing optimisation problems.

Suppose that a given domain is discretised into n (a finite number) cells.

In an ISE topology each of these cells can either be empty or filled with an isotropic material. Thus there will be 2^n different designs possible in ISE topology class. Restricting the maximum volume of materials to m elements, the number of possible ISE designs will be reduced to $\binom{n}{m}$. Apparently not all of these designs are feasible, but even after subtracting infeasible ones the number of possible designs will be a huge number. For the sake of illustration in case of a domain size of 500 elements where the volume ratio of material is restricted to 26%, the number of possible ISE designs with one material will be $\binom{500}{130}$, something above 1.1×10^{123}. This is more than the number of protons which can be fitted in the observable universe.* In a normal practical case one might deal with a finite element mesh of order of 10,000 or even 100,000 elements. So the feasible space of the topology optimisation problem can be *really* huge. To deal with such a great number of design variables the usual optimisation techniques are not applicable.

A common approach to solve these large-scale problems is via *optimality criteria methods*. Unlike mathematical programming techniques, optimality criteria methods solve the optimisation problem indirectly. In these methods a set of criteria are satisfied which are related to the optimality condition of the system (Hassani and Hinton 1998c). These criteria can be selected intuitively. An example of intuitive optimality criteria is the so-called *fully stressed design* which assumes that a structure is optimum when all of its components are fully stressed. Another possible approach is to derive optimality criteria mathematically. These types of optimality criteria are mostly

*The diameters of the proton and the observable universe are taken as 10^{-15}m and 10^{26}m respectively (Ford 1991). The volume of the observable universe divided by the volume of a proton is thus equals to 10^{123}.

based on Karush-Kuhn-Tucker (KKT) optimality conditions (Karush 1939; Kuhn and Tucker 1951). The KKT conditions state the necessary conditions for optimality of a solution.

Karush-Kuhn-Tucker conditions

A general optimisation problem can be stated as

$$\begin{aligned} \min_{\mathbf{x}\in\mathbb{R}^n} \quad & f(\mathbf{x}) \\ \text{such that} \quad & g_i(\mathbf{x}) \leq 0,\ i = 1,\dots,n \\ & h_j(\mathbf{x}) = 0,\ j = 1,\dots,m \end{aligned} \tag{2.5}$$

where $f : \mathbb{R}^n \mapsto \mathbb{R}$, $g_i : \mathbb{R}^n \mapsto \mathbb{R}$ and $h_j : \mathbb{R}^n \mapsto \mathbb{R}$. Let $\mathbf{x}^*$ be a regular point in $\mathbb{R}^n$. This means at this point the gradients of all active constraints are linearly independent. Also assume that all functions in (2.5) are continuously differentiable at $\mathbf{x}^*$. The KKT conditions state that if $\mathbf{x}^*$ is a local minimum, there exists constants μ_i and ν_j such that

$$\begin{cases} \nabla f(\mathbf{x}^*) + \sum_{i=1}^m \mu_i \nabla g_i(\mathbf{x}^*) + \sum_{j=1}^m \nu_j \nabla h_j(\mathbf{x}^*) = 0, \\ h_j(\mathbf{x}^*) = 0, \quad \forall j = 1,\dots,m, \\ g_i(\mathbf{x}^*) \leq 0, \quad \mu_i g_i(\mathbf{x}^*) = 0, \quad \mu_i \geq 0, \quad \forall i = 1,\dots,n \end{cases} \tag{2.6}$$

2.3.1 Minimum compliance design

A fairly common objective function selected in structural topology optimisation is the *mean compliance*. For a general linear elasticity problem depicted in Figure 2.6, the mean compliance can be defined as

$$l(u) = \int_{\Omega} fu\mathrm{d}\Omega + \int_{\Gamma_t} tu\mathrm{d}\Gamma, \tag{2.7}$$

with u representing displacement field and f and t standing for body forces and surface tractions respectively. Ω represents the whole domain and Γ_t is that part of boundary where surface tractions apply. Another part of boundary Γ_u is fixed (Fig. 2.6). It can be seen in (2.7) that the mean compliance is equivalent to the external work.

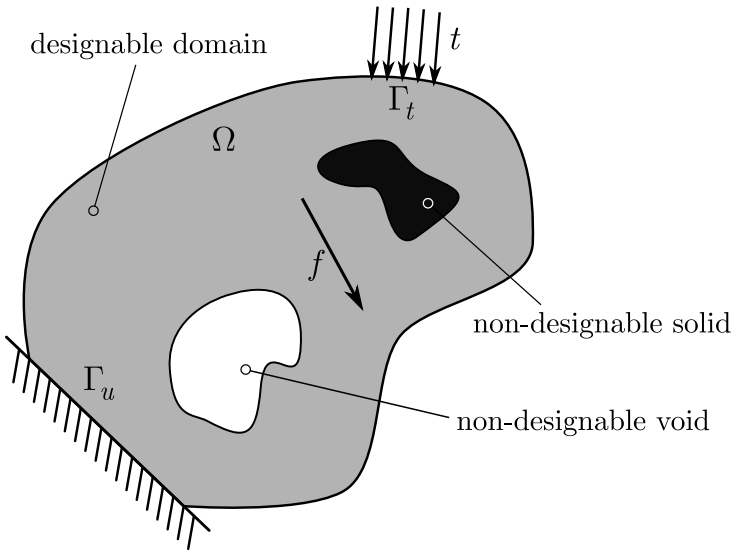

Figure 2.6 A general topology optimisation problem in a two-dimensional domain.

The internal energy for an arbitrary virtual displacement v at the equi-

librium u can be expressed as

$$a(u,v) = \int_\Omega E_{ijkl}(\xi)\epsilon_{ij}(u)\epsilon_{kl}(v)\mathrm{d}\Omega \tag{2.8}$$

where $E_{ijkl}(\xi)$ is the stiffness tensor which can vary with location ξ. $\epsilon_{ij}(u) = \frac{1}{2}(u_{i,j} + u_{j,i})$ are linearised strains. The minimum compliance problem can thus be expressed as

$$\min_{u\in\mathcal{U},x} \quad l(u) \tag{2.9a}$$

$$\text{such that} \quad a_x(u,v) = l(v), \quad \forall v \in \mathcal{U}, \tag{2.9b}$$

$$x \in \mathcal{X} \tag{2.9c}$$

Here x denotes the field of topological design variables. The notation $a_x(u,v)$ means the stiffness tensor E_{ijkl} in (2.8) is a function of design variables. In other words, $E_{ijkl} = E_{ijkl}(x)$ where $x = x(\xi)$. The first condition (2.9b) is the equilibrium condition expressed in the form of virtual work. In this equation $\mathcal{U}$ is the space of kinematically admissible displacement fields. The second condition (2.9c) expresses the design restrictions. Here $\mathcal{X}$ is the set of admissible design variables.

In (2.9b) if one substitutes $v = u$, one will get $a(u,u) = l(u)$. Noting that $\frac{1}{2}a(u,u)$ is the strain energy, one can conclude that mean compliance is twice the strain energy.

It should be noted that in (2.9) two fields (x and u) are of interest. If one discretises both of these fields with the same finite element mesh, the

problem (2.9) can be rewritten as (Bendsøe and Sigmund 2003)

$$\begin{aligned} \min_{\mathbf{u},\mathbf{x}} \quad & c(\mathbf{x}) = \mathbf{f}^T\mathbf{u} \\ \text{such that} \quad & \mathbf{K}(\mathbf{x})\mathbf{u} = \mathbf{f}, \\ & x_i \in \mathcal{X}, \quad \forall i \end{aligned} \tag{2.10}$$

with $\mathbf{f}$ and $\mathbf{u}$ denoting nodal displacement and nodal force vectors respectively. $c(\mathbf{x})$ is the mean compliance and $\mathbf{x}$ is the vector of design variables. The global stiffness matrix $\mathbf{K}$ can be derived by assembling element stiffness matrices in the form of $\mathbf{K}(\mathbf{x}) = \sum_{i=1}^{N} \hat{\mathbf{K}}_i(\mathbf{x})$. Here $\hat{\mathbf{K}}_i$ is the element stiffness matrix at global level. If one assigns one design variable to each element this relation can be simplified to $\mathbf{K}(\mathbf{x}) = \sum_{i=1}^{N} \hat{\mathbf{K}}_i(x_i)$.

2.3.2 Sensitivity analysis

In order to derive optimality conditions for (2.9) one can use KKT conditions in (2.6). This, however, requires the sensitivity of objective function to be calculated. The sensitivity of the mean compliance can be calculated directly (Tanskanen 2002) or by using adjoint method (Bendsøe and Sigmund 2003). Here the latter approach is used.

The mean compliance can be rewritten in the following form by adding the adjoint field $\tilde{\mathbf{u}}$ multiplied by a zero function

$$c(\mathbf{x}) = \mathbf{f}^T\mathbf{u} - \tilde{\mathbf{u}}^T(\mathbf{K}(\mathbf{x})\mathbf{u} - \mathbf{f}) \tag{2.11}$$

After differentiation one will get

$$\frac{\partial c}{\partial x_i} = (\mathbf{f}^T - \tilde{\mathbf{u}}\mathbf{K})\frac{\partial \mathbf{u}}{\partial x_i} - \tilde{\mathbf{u}}^T\frac{\partial \mathbf{K}}{\partial x_i}\mathbf{u} \tag{2.12}$$

The adjoint equation derived for the mean compliance is $\mathbf{f}^T - \tilde{\mathbf{u}}\mathbf{K} = 0$. This equation is the same as equilibrium equation and does not need to be solved separately. For this, mean compliance is known to be a self-adjoint function.

The adjoint equation can be satisfied by setting $\tilde{\mathbf{u}} = \mathbf{u}$. Hence (2.12) can be simplified to

$$\frac{\partial c}{\partial x_i} = -\mathbf{u}^T\frac{\partial \mathbf{K}}{\partial x_i}\mathbf{u} \tag{2.13}$$

If one design variable is assigned to each element this relation can be simplified to $\frac{\partial c}{\partial x_i} = -\mathbf{u}^T\frac{\partial \hat{\mathbf{K}}_i}{\partial x_i}\mathbf{u}$. Again noting that the only non-zero components of $\hat{\mathbf{K}}_i$ correspond to the i-th elements degrees of freedom, one can further simplify this equation to

$$\frac{\partial c}{\partial x_i} = -\mathbf{u}_i^T\frac{\partial \mathbf{K}_i}{\partial x_i}\mathbf{u}_i \tag{2.14}$$

where $\mathbf{K}_i$ and $\mathbf{u}_i$ are the local level stiffness matrix and displacement vector of the i-th element. This equation shows that sensitivities of the mean compliance are local i.e. the sensitivity of an element only depends on the responses of that element.

Using (2.14) and KKT conditions, the optimality conditions of (2.10) can be easily obtained. It should be noted that the KKT conditions shown in (2.6) are only valid for problems written in the form of (2.5). That is, the problem should be a minimisation problem and the inequality conditions

should be of the form $g_i(x) \leq 0$. Changing the direction of inequalities or changing the problem from minimisation to maximisation will change the sign of μ_i in (2.6) (Hassani and Hinton 1999).

The following four sections introduce the four most common topology optimisation techniques in chronological order. All these techniques solve the topology optimisation problem indirectly using optimality criteria approach.

2.4 Homogenisation method

The homogenisation method was originally presented by Bendsøe and Kikuchi (1988). It was the first practical method in the field of structural topology optimisation and set up the basis for many further studies in the field.

In this method the design domain is assumed to be made of periodic microstructures. These microstructures have some microscale voids inside them whose size and orientation can be controlled by design variables. The microstructures are selected in such a way that they can yield the two limiting cases of solid material and void. That is, by changing the design variables, it should be possible that the void area inside a microstructure become zero or cover the whole area of that microstructure. Two commonly used microstructures are microcells with rectangular holes and layered materials (Hassani and Hinton 1998b, 1999). Figure 2.7 shows these types of microstructures.

Other types of microstructures may also be used in homogenisation method (Bendsøe and Kikuchi 1988; Matsui and Terada 2004). Using microstructures results in an ISEP topology (Rozvany 2001).

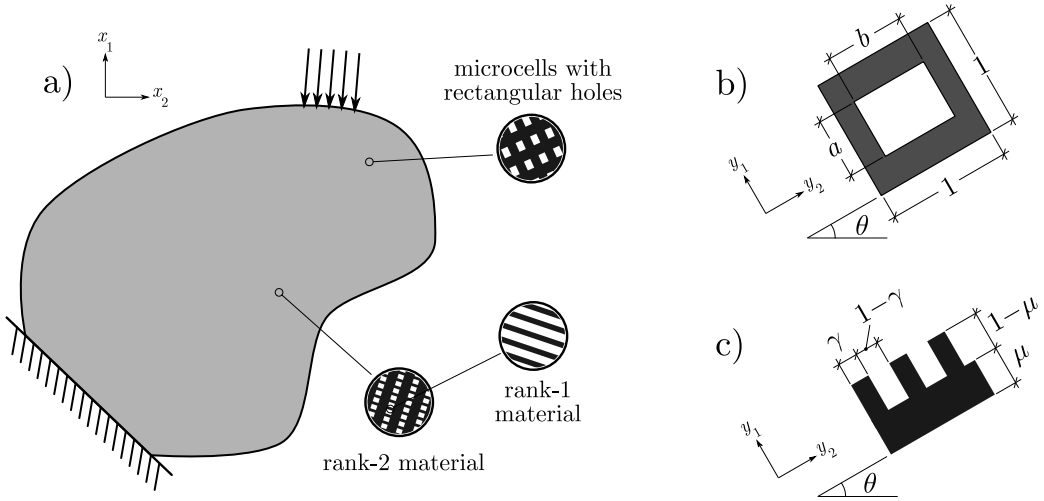

Figure 2.7 Two commonly used microcells in the homogenisation method: a) the macroscopic and microscopic scale; b) control parameters of microcells with rectangular holes; c) control parameters of second rank layered material.

2.4.1 Calculating homogenised properties of microcells

Mechanical properties of microstructures can be calculated using homogenisation theory (Hassani and Hinton 1998a). This results in a relationship between density of material in microstructures and their effective mechanical properties (Bendsøe and Kikuchi 1988). The homogenisation theory links the mechanical properties of homogenised cells in macroscopic scale to the properties of microstructures in microscopic scale. The so-called homogenisation equations should be solved for microstructures at microscopic scale. The resulted homogenised mechanical properties can then be used in macroscopic scale to analyse the homogenised structure. After homogenisation the original ISEP topology changes into an ASE topology (Rozvany 2001).

For elasticity problems the homogenisation theory results in the following equation for homogenised modulus of elasticity (Bendsøe and Kikuchi 1988;

Hassani and Hinton 1998a)

$$E^H_{ijkl}(x) = \frac{1}{|Y|}\int_Y \left(E_{ijkl} - E_{ijpq}\frac{\partial \chi^{kl}_p}{\partial y_q} \right) \mathrm{d}Y \tag{2.15}$$

where E^H_{ijkl} are the homogenised elasticity coefficients of the considered microcell. E_{ijkl} are elasticity constants of the base material, i.e. the material the microcell is made of. x and y denote the macroscopic (general) and microscopic (local) coordinates respectively. $|Y|$ is the size of the base cell and is defined as $|Y| = \int_Y 1 \, \mathrm{d}Y$. The tensor $\chi^{kl} = \chi^{kl}(y)$ should satisfy the following equation

$$\int_Y E_{ijpq}\frac{\partial \chi^{kl}_p}{\partial y_q}\frac{\partial v_i}{\partial y_j}\mathrm{d}Y = \int_Y E_{ijkl}\frac{\partial v_i}{\partial y_j}\mathrm{d}Y, \quad \forall v \in \mathcal{V}_Y \tag{2.16}$$

Here $\mathcal{V}_Y$ can be defined as the space of all Y-periodic functions over the microcell (Bendsøe and Sigmund 2003). After solving (2.16) for χ^{kl} in microscopic scale (y), one can calculate homogenised mechanical properties of the microstructure through (2.15).

The equation (2.16) for layered materials can be calculated analytically. But for microcells with rectangular holes there is no close-form solution for (2.16) and one need to apply numerical methods (such as finite element method) to calculate effective homogenised properties of these microstructures (Hassani and Hinton 1998b). Here, for sake of brevity, we only report the calculated values of homogenised properties of these microstructures in a special case. The interested reader may consult Hassani and Hinton (1998a,b), Eschenauer and Olhoff (2001), or Bendsøe and Kikuchi (1988)

for further information about homogenisation theory and the procedures to calculate these results.

The control parameters for microcells with rectangular holes and second ranked layered materials have been illustrated in Figure 2.7b and Figure 2.7c. Here, for simplicity, it is assumed that in both types of microstructures the holes are square shaped, i.e. $b = a$ and $\mu = \gamma$. It is assumed that the material in use is an isotropic material with Young's modulus of $E = 0.91$ and Poisson's ratio of $\nu = 0.3$. The elasticity matrix for plane stress hence reads $\left(\begin{smallmatrix} 1 & .3 & 0 \\ .3 & 1 & 0 \\ 0 & 0 & .35 \end{smallmatrix}\right)$. It can be readily concluded that the microstructures made of this isotropic material will response like an orthotropic material in macroscopic scale. The microcells are assumed to be square-shaped with unit length ($Y =]0,1[\times]0,1[$). The homogenised elasticity constants of microcells with square hole and of second ranked layered materials are reported in Table 2.1 and Table 2.2 for different values of a and γ respectively (Hassani and Hinton 1998b, 1999).

Table 2.1 Homogenised elasticity constants of microcells with square holes. The base material is an isotropic material with $E = 0.91$ and $\nu = 0.3$.

$a = b$	E^H_{1111}	E^H_{2222}	E^H_{1122}	E^H_{1212}	ρ
1.0	0.0000	0.0000	0.0000	0.0000	0.00
0.9	0.0925	0.0925	0.0035	0.0005	0.19
0.8	0.1886	0.1886	0.0141	0.0045	0.36
0.7	0.2891	0.2891	0.0328	0.0168	0.51
0.6	0.3955	0.3955	0.0606	0.0441	0.64
0.5	0.5101	0.5101	0.0992	0.0917	0.75
0.4	0.6348	0.6348	0.1487	0.1582	0.84
0.3	0.7644	0.7644	0.2039	0.2313	0.91
0.2	0.8833	0.8833	0.2540	0.2947	0.96
0.1	0.9689	0.9689	0.2882	0.3360	0.99
0.0	1.0000	1.0000	0.3000	0.3500	1.00

In case of layered materials the homogenised stiffness matrix will be singular. To avoid singularity one should use a soft material instead of voids. Here this soft material has been chosen a hundred times softer than the actual material by setting its Young's modulus equal to 0.0091.

Table 2.2 Homogenised elasticity constants of second ranked layered materials. The base material is an isotropic material with $E = 0.91$ and $\nu = 0.3$.

$\gamma = \mu$	E^H_{1111}	E^H_{2222}	E^H_{1122}	E^H_{1212}	ρ
0.0	0.0100	0.0100	0.0030	0.0035	0.00
0.1	0.1101	0.1013	0.0066	0.0043	0.19
0.2	0.2272	0.1932	0.0172	0.0054	0.36
0.3	0.3579	0.2865	0.0360	0.0071	0.51
0.4	0.4957	0.3820	0.0635	0.0096	0.64
0.5	0.6314	0.4803	0.0988	0.0136	0.75
0.6	0.7548	0.5817	0.1399	0.0208	0.84
0.7	0.8570	0.6862	0.1839	0.0353	0.91
0.8	0.9325	0.7930	0.2275	0.0706	0.96
0.9	0.9797	0.9013	0.2678	0.1759	0.99
1.0	1.0000	1.0000	0.3000	0.3500	1.00

In these tables the last column shows values of relative density ρ of microstructures. For microcells with rectangular holes one can write $\rho = 1 - ab$ while for layered materials this relation takes the form of $\rho = \gamma + \mu - \gamma\mu$ (Fig. 2.7). In Figure 2.8 the homogenised elasticity constants of the two considered microstructures are shown against the relative density of the cell. It can be seen that the homogenised properties of the two microstructures are close to each other except for the shear term E_{1212} where rank-2 layered materials are substantially weaker in intermediate densities.

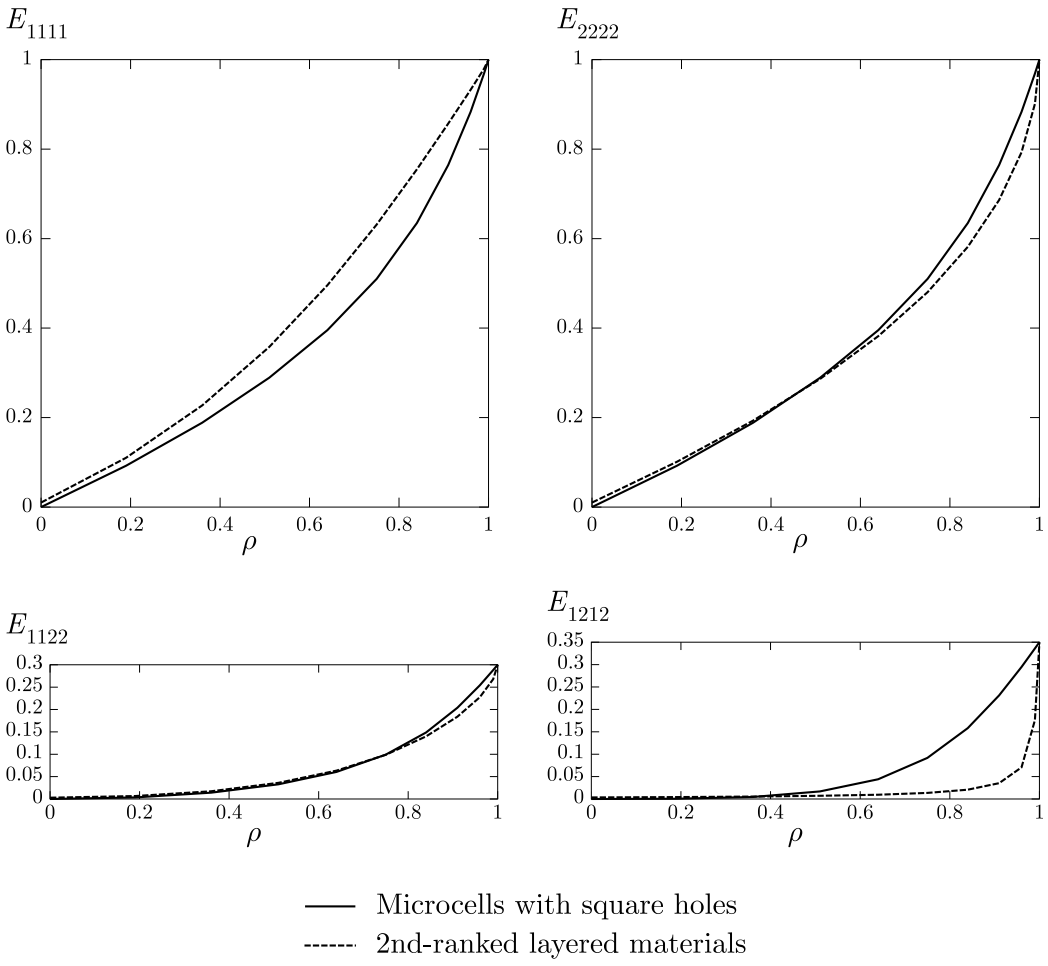

Figure 2.8 Comparing the homogenised elasticity constants of microcells with rectangular holes and rank-2 layered materials.

2.4.2 Deriving optimality criteria

The minimum compliance design problem using microcells with square holes can be expressed as

$$\begin{aligned} \min_{\mathbf{u},\mathbf{a},\boldsymbol{\theta}} \quad & c(\mathbf{a},\boldsymbol{\theta}) = \mathbf{f}^T\mathbf{u} \\ \text{such that} \quad & \mathbf{K}(\mathbf{a},\boldsymbol{\theta})\mathbf{u} = \mathbf{f}, \\ & a_i - 1 \leq 0, \quad i = 1,\ldots,N \\ & -a_i \leq 0, \quad i = 1,\ldots,N \\ & \sum_{i=1}^{N}(1-a_i^2)V_i - \bar{V} \leq 0 \end{aligned} \tag{2.17}$$

Here N is the number of elements; V_i is the volume of the i-th element; and $\bar{V}$ is the maximum allowable volume of material. For laminated materials $\mathbf{a}$ and a_i should be changed to $\boldsymbol{\gamma}$ and γ_i respectively. The Lagrangian functional associated to (2.17) takes the following form

$$\begin{aligned} \mathfrak{L} = \mathbf{f}^T\mathbf{u} + \bar{\mathbf{u}}^T(\mathbf{K}\mathbf{u} - \mathbf{f}) + \\ \sum_{i=1}^{N}\Big(\lambda_i^u(a_i - 1) + \lambda_i^l(-a_i)\Big) + \Lambda\sum_{i=1}^{N}\Big((1-a_i^2)V_i - \bar{V}\Big) \end{aligned} \tag{2.18}$$

where $\bar{\mathbf{u}}$ is the vector of Lagrange multipliers for equilibrium condition and is a kinematically admissible displacement vector. λ_i^u and λ_i^l are Lagrange multipliers for upper and lower limit conditions of design variables $\mathbf{a}$ and Λ is the Lagrange multiplier for volume constraint. Differentiating $\mathfrak{L}$ with respect to displacement $\mathbf{u}$ and setting it to zero implies $\bar{\mathbf{u}} = \mathbf{u}$. Stationarity of the

Lagrangian with respect to $\mathbf{a}$ and $\boldsymbol{\theta}$ requires that

$$\frac{\partial c}{\partial a_i} + \lambda_i^u - \lambda_i^l - 2a_i V_i \Lambda = 0, \qquad \forall i = 1, \ldots, n \tag{2.19a}$$

$$\frac{\partial c}{\partial \theta_i} = 0, \qquad \forall i = 1, \ldots, n \tag{2.19b}$$

The sensitivities of the mean compliance can be substituted in (2.19) from (2.14) i.e. $\frac{\partial c}{\partial a_i} = -\mathbf{u}_i^T \frac{\partial \mathbf{K}_i}{\partial a_i}\mathbf{u}_i$ and $\frac{\partial c}{\partial \theta_i} = -\mathbf{u}_i^T \frac{\partial \mathbf{K}_i}{\partial \theta_i}\mathbf{u}_i$. Note that the (2.17) is written in the same format as (2.5). Hence the KKT conditions (2.6) yield the following necessary conditions of optimality

$$\begin{aligned}
&\mathbf{K}\mathbf{u} - \mathbf{f} = 0, \\
&a_i - 1 \leq 0, \quad \lambda_i^u (a_i - 1) = 0, \quad \lambda_i^u \geq 0, \quad \forall i = 1, \ldots, N, \\
&-a_i \leq 0, \quad \lambda_i^l (-a_i) = 0, \quad \lambda_i^l \geq 0, \quad \forall i = 1, \ldots, N, \\
&\sum_{i=1}^{N} (1 - a_i^2) V_i - \bar{V} \leq 0, \quad \Lambda \sum_{i=1}^{N} \Big((1 - a_i^2) V_i - \bar{V} \Big) = 0, \quad \Lambda \geq 0
\end{aligned} \tag{2.20}$$

The conditions in (2.20) together with (2.19) are the necessary conditions of optimality for any solution of (2.17).

To solve the problem (2.17), using the optimality conditions (2.19) and (2.20), Bendsøe and Kikuchi (1993) proposed the following resizing scheme

$$a_i^{K+1} = \begin{cases} \min\{(1+\zeta)a_i^K, 1\} & \text{if } a_i^K (\mathfrak{B}_i^K)^\eta \leq \max\{(1-\zeta)a_i^K, 0\} \\ \max\{(1-\zeta)a_i^K, 0\} & \text{if } a_i^K (\mathfrak{B}_i^K)^\eta \geq \min\{(1+\zeta)a_i^K, 1\} \\ a_i^K (\mathfrak{B}_i^K)^\eta & \text{otherwise} \end{cases} \tag{2.21}$$

Here the superscript K denotes the value of parameters at iteration step K;

ζ is the move limit and η is a weighting factor (Bendsøe and Kikuchi 1988) with typical values of 0.2 and 0.5 respectively. $\mathfrak{B}_i$ is defined as

$$\mathfrak{B}_i = \frac{\left(\frac{\partial c}{\partial a_i}\right)}{2a_i V_i \Lambda} = \frac{-\mathbf{u}_i^T \frac{\partial \mathbf{K}_i}{\partial a_i} \mathbf{u}_i}{2a_i V_i \Lambda} \tag{2.22}$$

Using (2.19a) one can easily show that $\mathfrak{B}_i = 1 + \frac{\lambda_i^l}{2a_i V_i \Lambda} - \frac{\lambda_i^u}{2a_i V_i \Lambda}$. If $0 < a_i < 1$ it can be readily seen from (2.20) that $\lambda_i^u = \lambda_i^l = 0$ and hence $\mathfrak{B}_i = 1$. Suppose at some iteration K, in order to move towards optimum, more material should be added to the i-th element. This means that at this iteration a_i should be reduced and hence $a_i < 1$ which implies $\lambda_i^u = 0$ and consequently $\mathfrak{B}_i \geq 1$. Similarly for increasing a_i one will get $\mathfrak{B}_i \leq 1$ (Hassani and Hinton 1999). This justifies the update scheme (2.21). An improved version of this update scheme has been suggested by Hassani and Hinton (1998c).

In order to use the resizing scheme (2.21) one needs to calculate Γ. This can be achieved by solving $\Lambda \sum_{i=1}^{N} \left((1 - a_i^2) V_i - \bar{V} \right) = 0$ using, for example, bisection method in an inner loop (Hassani and Hinton 1999; Bendsøe and Sigmund 2003). The optimal orientation can be calculated by solving (2.19b) via a combined Newton-bisection method (Bendsøe and Kikuchi 1988) or by matching the orientation of microstructures to those of principal stresses (Suzuki and Kikuchi 1991). It is also possible to use other approaches to update microcells' orientation (Hassani and Hinton 1999).

A brief algorithm for the homogenisation method is shown in Figure 2.9. Once the homogenised properties of microstructures are found, one can use them to solve different topology optimisation problems.

1: Find the homogenised mechanical properties of microstructures as functions of the design variables (eqs. 2.15 and 2.16).
2: Discretise the problem's domain.
3: Select initial values of design variables within the feasible space.
4: **repeat**
5: Assign the homogenised properties of microcells to elements.
6: Perform FE analysis and calculate the objective function.
7: **repeat**
8: Update the design variables using the update scheme (eq. 2.21).
9: Update Lagrangian multiplier of volume constraint.
10: **until** volume constraint becomes active
11: **until** convergency criteria are met
12: **print** the results
13: **end**

Figure 2.9 An algorithm for the homogenisation method.

2.4.3 Numerical examples

To illustrate the application of the homogenisation method, the optimal topology of a short cantilever beam is found using this method by minimising the mean compliance. The design domain and loading conditions of the beam are illustrated in Figure 2.10. The width and length of the domain are taken as $l = 16$ and $w = 10$ respectively. The volume of using material is restricted to 40% of the design domain. Young's modulus of the material is $E = 0.91$ and its Poisson's ratio is $\nu = 0.3$. All units are consistent. The domain Ω is discretised into 32×20 square shaped finite elements.

The final topologies and the evolution histories of objective function are shown in Figure 2.11. The high-order 9-node square-shaped finite elements have been used in these examples.

The initial solutions correspond to a uniform distribution of similar mi-

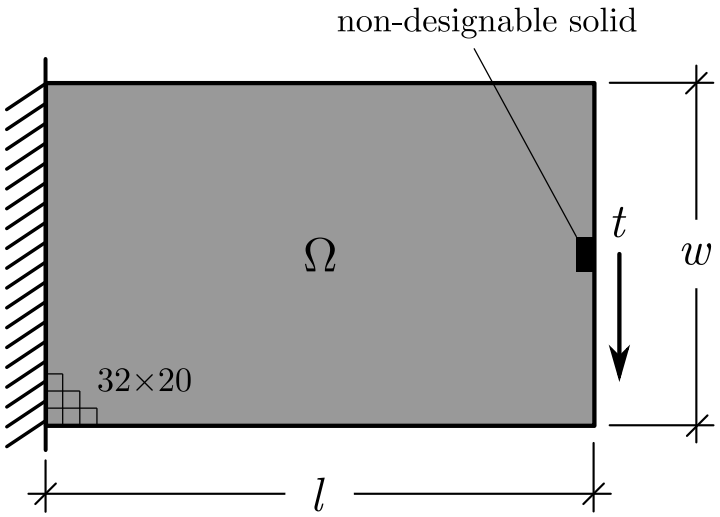

Figure 2.10 Problem definition and design domain of short cantilever beam.

crocells. It can be seen that in both cases the final topology shows a significantly smaller value of mean compliance. The initial and final values of the objective function in case of microcells with square holes are 486.8 and 69.07 respectively. For layered materials these values are 16623.3 and 87.61 respectively. The large drop at the beginning of the case of layered materials corresponds to updating microcells' orientation.

2.5 The SIMP method

Bendsøe (1989) presented a new topology optimisation method based on the homogenisation method. In this new approach Bendsøe (1989) used the relative densities directly as design variables. He called it *the direct approach*. Unlike the preceding homogenisation method, in the direct approach there is no need to calculate the homogenised properties of microstructures. In fact

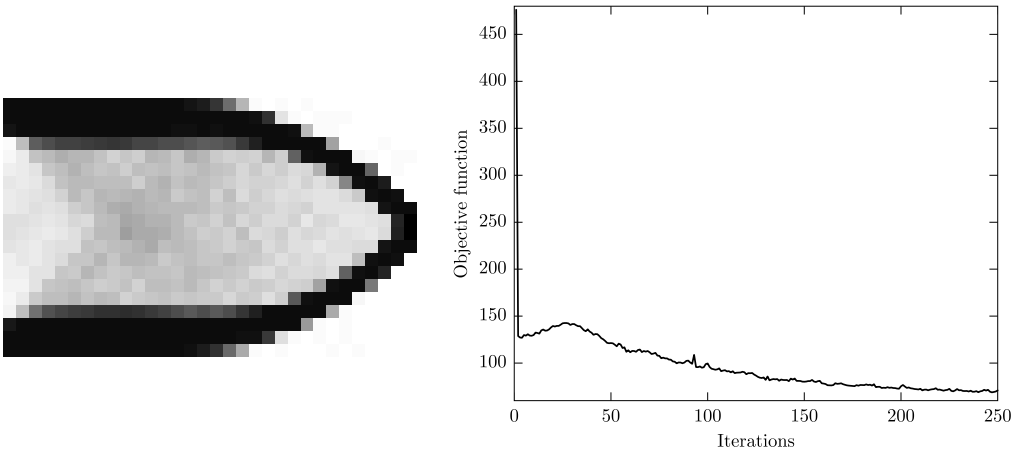

(a) microcells with square holes

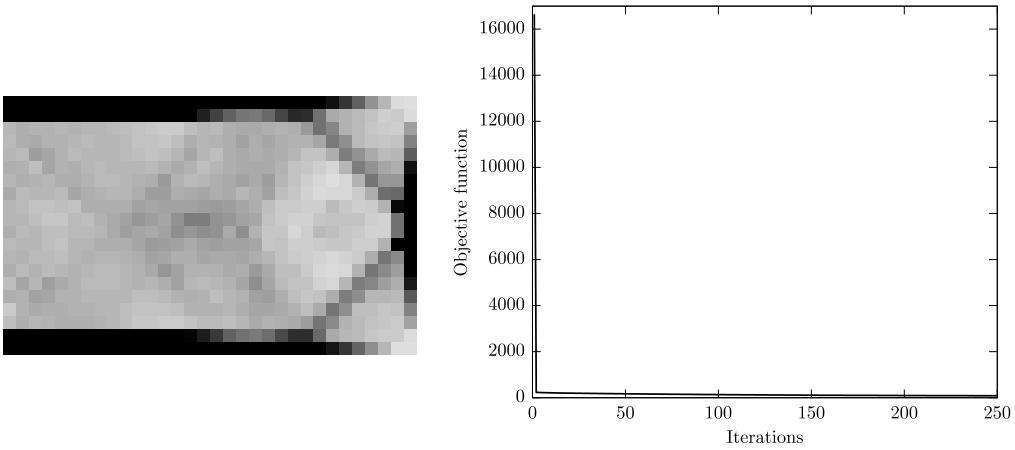

(b) layered materials

Figure 2.11 The final results obtained by the homogenisation method for SCB problem.

there is no microstructures in use. Instead it is assumed that the structure is made of an *artificial material* whose elasticity constants are changing by its density. For this reason the approach is also referred to as 'the artificial material model' by some authors (e.g. Hassani and Hinton 1998c). Later on the name *SIMP* standing for 'Solid Isotropic Microstructures with Penalisation' was selected by Rozvany et al. (1992) for this approach. The same term SIMP was also used by Bendsøe and Sigmund (1999) with 'M' standing for 'Material'.

2.5.1 Material model

The relationship between the elasticity tensor and the density of the base material is commonly referred to as material interpolation scheme (Bendsøe and Sigmund 1999). In his original paper Bendsøe (1989) used the so-called *power-law* approach as material interpolation scheme. The power-law interpolation scheme can be written as

$$E_{ijkl}(\rho) = [\rho(\xi)]^p \bar{E}_{ijkl}, \quad \xi \in \Omega \tag{2.23}$$

where E_{ijkl} is the interpolated stiffness tensor which replaces the homogenised stiffness tensor in the homogenisation method; $\bar{E}_{ijkl}$ stands for elasticity constants of the base material and $\rho(\xi)$ is the relative density function with $0 \leq \rho(\xi) \leq 1$. ξ indicates the location and Ω is the design domain. The parameter p is a penalisation factor which penalises the intermediate density values $0 < \rho < 1$ and push the topology towards a solid/empty (with $\rho = 1$

and $\rho = 0$) topology.

Using an isotropic base material, unlike homogenisation approach, this material model yields an isotropic interpolated material. The resulted topology is thus an ISE topology. However note that in (2.23) the material changes continuously from void to solid and hence the resulted topology is not a binary ISE but rather a relaxed one. Applying high penalty factors, the resulted topology will be more close to a binary ISE topology. On the other hand setting $p = 1$ in (2.23) the optimisation problem will change to a variable thickness sheet problem (Bendsøe 1989). For comparison, the resulted elasticity constants of SIMP material model with $p = 2$ and $p = 3$ are depicted in Figure 2.12 along with results of homogenised microcells with square holes. In this graph, the base material has modulus of elasticity of 0.91 and Poisson's ratio of 0.3.

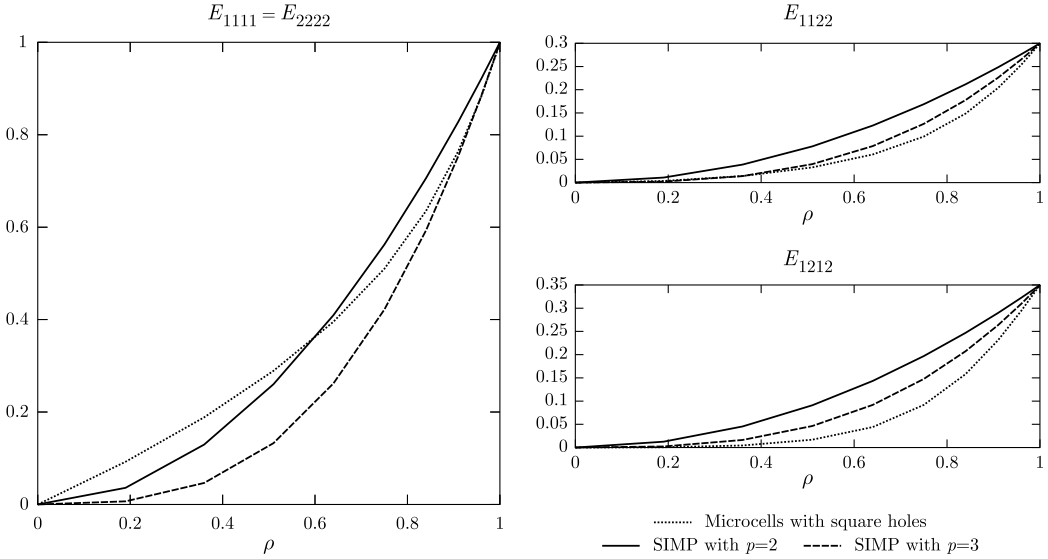

Figure 2.12 The SIMP material model with penalty values of $p = 2$ and $p = 3$ compared with microcells with square holes.

Despite simplicity and satisfactory results of the SIMP method, Bendsøe

(1989) mentioned the fictitious material properties in the SIMP material model and stated that the homogenisation method is preferred. Nevertheless the SIMP approach superseded the original homogenisation method shortly after introduction. Later Bendsøe and Sigmund (1999) proposed a physical interpretation of the so-called artificial material model. According to Bendsøe and Sigmund (1999) the power-law material model can correspond to a real physical microstructural model providing

$$p \geq \max\left\{\frac{2}{1-\nu}, \frac{4}{1+\nu}\right\}, \qquad \text{in 2D} \tag{2.24}$$

$$p \geq \max\left\{15\frac{1-\nu}{7-5\nu}, \frac{3(1-\nu)}{2(1-2\nu)}\right\}, \qquad \text{in 3D} \tag{2.25}$$

with ν denoting the Poisson's ratio of the base material.

Note that the power-law interpolation scheme will result in singular stiffness for $\rho = 0$. In order to avoid singularity, a soft material should be used instead of void. This can be achieved by increasing the lower bound of ρ from 0 to a small positive number $\underline{\rho}$. The box constraints on relative density in the SIMP method thus becomes $0 < \underline{\rho} \leq \rho \leq 1$.

2.5.2 Deriving optimality criteria

The solution procedure for the SIMP method is similar to that of the homogenisation method. Using finite element discretisation, the minimum com-

pliance design problem takes the form

$$\begin{aligned} \min_{\mathbf{u},\boldsymbol{\rho}} \quad & c(\boldsymbol{\rho}) = \mathbf{f}^T\mathbf{u} \\ \text{such that} \quad & \mathbf{K}(\boldsymbol{\rho})\mathbf{u} = \mathbf{f}, \\ & \rho_i - 1 \leq 0, \quad i = 1, \ldots, N \\ & \underline{\rho} - \rho_i \leq 0, \quad i = 1, \ldots, N \\ & \sum_{i=1}^{N}(\rho_i V_i) - \bar{V} \leq 0 \end{aligned} \tag{2.26}$$

The Lagrangian functional for the above equation can be expressed as

$$\begin{aligned} \mathfrak{L} = \mathbf{f}^T\mathbf{u} + \bar{\mathbf{u}}^T(\mathbf{K}\mathbf{u} - \mathbf{f}) + \\ \sum_{i=1}^{N}\Big(\lambda_i^u(\rho_i - 1) + \lambda_i^l(\underline{\rho} - \rho_i)\Big) + \Lambda\Big(\sum_{i=1}^{N}(\rho_i V_i) - \bar{V}\Big) \end{aligned} \tag{2.27}$$

Stationarity of $\mathfrak{L}$ with respect to ρ_i implies that

$$\frac{\partial c}{\partial \rho_i} + \lambda_i^u - \lambda_i^l + V_i\Lambda = 0, \quad \forall i = 1, \ldots, n \tag{2.28}$$

Similar to homogenisation method, if the parameter $\mathfrak{B}_i$ is defined as

$$\mathfrak{B}_i = \frac{-\left(\frac{\partial c}{\partial \rho_i}\right)}{V_i\Lambda} \tag{2.29}$$

the following update scheme for ρ can be proposed

$$\rho_i^{K+1} = \begin{cases} \max\{(1-\zeta)\rho_i^K, \underline{\rho}\} & \text{if } \rho_i^K(\mathfrak{B}_i^K)^\eta \leq \max\{(1-\zeta)\rho_i^K, \underline{\rho}\} \\ \min\{(1+\zeta)\rho_i^K, 1\} & \text{if } \rho_i^K(\mathfrak{B}_i^K)^\eta \geq \min\{(1+\zeta)\rho_i^K, 1\} \\ \rho_i^K(\mathfrak{B}_i^K)^\eta & \text{otherwise} \end{cases} \tag{2.30}$$

The partial derivatives of the mean compliance with respect to ρ in (2.29) can be easily calculated using the power-law equation (2.23) in (2.14)

$$\frac{\partial c}{\partial \rho_i} = -p\rho_i^{p-1}\mathbf{u}_i^T\mathbf{K}_i\mathbf{u}_i, \quad i = 1, \ldots, N \tag{2.31}$$

Like homogenisation method, the Lagrange multiplier of volume constraint Λ need to be calculated in an inner loop in each iteration.

The algorithm of the SIMP method has been reviewed in Figure 2.13. A 99-line code in Matlab for the SIMP method has been published by Sigmund (2001).

1: Discretise the problem's domain.
2: Select initial values of densities. A uniform distribution is a good starting point.
3: **repeat**
4: Perform FE analysis and calculate the objective function.
5: **repeat**
6: Update the design variables using the update scheme (eq. 2.30).
7: Update Lagrangian multiplier of volume constraint.
8: **until** volume constraint becomes active
9: **until** convergency criteria are met
10: **print** the results
11: **end**

Figure 2.13 An algorithm for the SIMP method.

2.5.3 Numerical example

The short cantilever beam problem depicted in Figure 2.10 is solved using the SIMP method to demonstrate the application of this method. Using (2.24), the minimum penalty factor for a two dimensional case with the Poisson's ratio of 0.3 can be calculated as $p = 3$. Here this minimum value is adopted. The lower limit of densities is chosen as $\underline{\rho} = 0.001$. The move limit and the damping factor in (2.30) are selected as $\zeta = 0.1$ and $\eta = 0.5$ respectively. The final topology and the evolution of the objective function are illustrated in Figure 2.14.

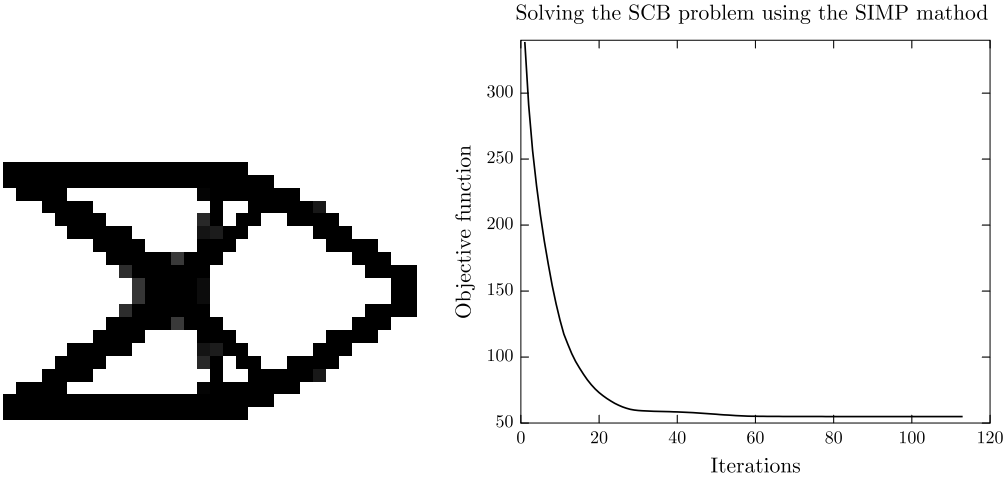

Figure 2.14 The final results obtained by the SIMP method for SCB problem. The graph on the right side shows the values of objective function in each iteration.

The initial objective function was 338.72 corresponding to the initially uniform distribution of material. This value reduces to 54.89 after optimisation. Note that because of the power-law material model, the objective function values in the SIMP method are not comparable to those obtained by the homogenisation method. The evolution of the topologies obtained by

the SIMP method for this problem is illustrated in Figure 2.15.

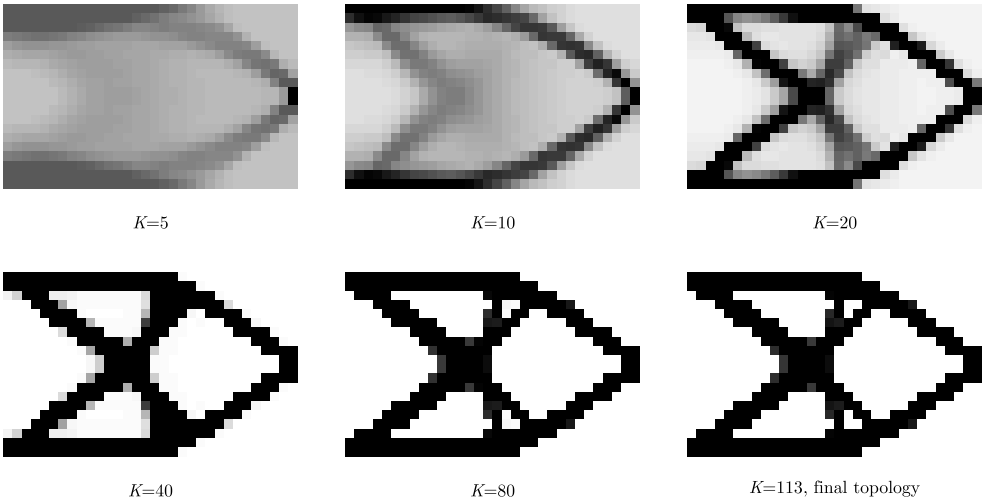

Figure 2.15 The topologies obtained by the SIMP method for the SCB problem at different iterations. The darkness of the elements in these grey-scale images corresponds to the value of their relative densities.

2.6 Evolutionary structural optimisation

Although choosing a large penalty in the SIMP method will result in a near-binary ISE topology, there will be still some elements with intermediate densities ($0 < \rho_i < 1$) in the final topology even for large penalty values. Moreover choosing large penalties causes convergency problems in the SIMP method. Hence to achieve a binary ISE topology one usually needs to perform some post-processing on the final topology obtained by the SIMP method.

Proposed by Xie and Steven (1993), the Evolutionary Structural Optimisation method, short-formed to *ESO*, was another topology optimisation technique which could provide binary ISE topologies. The ESO method is

based on the simple idea that by progressively removing inefficient parts, the structure will evolve towards an optimum. The removal of elements is controlled by a *rejection criterion*. This rejection criterion typically compares a scalar functional of the mechanical responses of the elements with a threshold value. The elements with values less than the threshold will then be removed. The ESO procedure totally removes the inefficient elements. This behaviour is sometimes referred to as *hard killing* as opposed to *soft killing* where a very soft material will be assigned to the inefficient elements. The ESO method is hence known as a hard kill method.

2.6.1 Stress-based ESO

In the original version of the ESO method (Xie and Steven 1993) the rejection criterion was based on the von Mises stress. The threshold value was defined as a ratio of the maximum von Mises stress in the structure in each iteration. This ratio, referred to as *rejection ratio* RR initially takes a small value like 1% (Xie and Steven 1993). After few iterations, because elements with low stress levels are being removed, all elements in the structure will have stress levels higher than the threshold level. This stage is referred to as *steady state*. After reaching a steady state the rejection ratio RR is increased by a predefined step size called *evolution rate* ER. Then the procedure continues with the new rejection ratio to reach a new steady state and henceforth until reaching a desired optimum level. The solution procedure can be seen as an intuitively based optimality criteria which defines the optimality based on the fully stressed design idea. The algorithm of this stress-based ESO

procedure is shown in Figure 2.16.

1: Discretise the problem's domain.
2: Initialise ER and RR and set the final value for RR (RR_{max}).
3: **repeat**
4: Perform FE analysis and calculate the von Mises stresses in all elements.
5: **if** $\sigma_i^{vm} \leq RR \cdot \sigma_{max}^{vm}$ **then**
6: Remove the element i.
7: **end if**
8: **if** no element is removed (steady state) **then**
9: $RR \leftarrow RR + ER$.
10: **end if**
11: **until** $RR \geq RR_{max}$ (or another termination criteria)
12: **print** the results
13: **end**

Figure 2.16 Algorithm for topology optimisation using a stress-based ESO method. σ_i^{vm} and σ_{max}^{vm} are the von Mises stress level in element i and the maximum von Mises stress of the structure respectively.

Since its original appearance, the ESO method has been improved mainly by its original developers and their colleagues and few other researchers (e.g Hinton and Sienz 1995; Kim et al. 2003). The application of the ESO method to other types of problems has been investigated by Xie and Steven (1997).

2.6.2 Compliance-based ESO

Chu et al. (1996) modified the ESO method to minimise the compliance (maximise the stiffness) of structures. To evaluate the efficiency of the elements in compliance-based ESO, Chu et al. (1996) used a *sensitivity number*. This number is an approximation of the change in the compliance due to removing an element. Here we report the procedure used by Chu et al. (1996)

to find the sensitivity numbers corresponding to minimum compliance design. Suppose that the i-th element is removing from a structure consisting N elements. The stiffness matrix $\mathbf{K}$ will then change to $\overset{-i}{\mathbf{K}}$. The change in the stiffness matrix can be expressed as $\Delta\mathbf{K} = \overset{-i}{\mathbf{K}} - \mathbf{K} = -\hat{\mathbf{K}}_i$ where $\hat{\mathbf{K}}_i$ is the stiffness matrix of the i-th element in global level. Note that the force vector $\mathbf{f}$ will not change by removing the elements. The change in compliance can thus be expressed as $\Delta c = \mathbf{f}^T \Delta\mathbf{u}$ which is defined as the sensitivity number for the i-th element, α_i. Ignoring higher order terms, the change in displacement vector takes the form $\Delta\mathbf{u} = -\mathbf{K}^{-1}\Delta\mathbf{K}\mathbf{u}$. Using this expression the sensitivity number for the i-th element can be defined as (Chu et al. 1996)

$$\alpha_i = \mathbf{u}_i^T \mathbf{K}_i \mathbf{u}_i \tag{2.32}$$

where $\mathbf{u}_i$ and $\mathbf{K}_i$ are the local level displacement vector and stiffness matrix of the i-th element. Using this definition, the solid elements with the lowest sensitivity numbers are the least efficient ones and consequently need to be removed.

The stress-based algorithm presented in Figure 2.16 can also be used in minimum compliance design. The only necessary modifications is changing σ_i^{vm} and σ_{max}^{vm} to α_i and α_{max} respectively. As pointed out by Li et al. (1999b) there are considerable similarities between the results obtained by stress-based ESO and compliance-based ESO.

The ESO method originally was not proposed on a mathematical basis. However Tanskanen (2002) discusses the equivalence of the compliance-based ESO method and "the sequential linear programming (SLP)-based approx-

imate optimisation method followed by the Simplex algorithm" with the compliance-volume product as the objective function provided that all elements are of same size.

In the ESO method the values of the mean compliance are not comparable in different iterations as the volume in each iteration is different. However the *performance index* defined by Yang et al. (2003) can be used as an indicator of optimality. The performance index is defined as $PI = c \times V/\bar{V}$ with $\bar{V}$ denoting the target volume. This definition is in line with Tanskanen (2002) who discussed that the actual objective function of the ESO method is the product of mean compliance and volume.

2.6.3 Numerical results

To demonstrate the application of the ESO technique the short cantilever beam problem (Fig. 2.10) has been solved using the compliance-based ESO method. Instead of 9-node quadrilateral elements, 8-node elements have been used in this example. In order to produce comparable results with other methods, the termination criteria in the algorithm has been changed to a condition on the materials volume. Here the main loop of the algorithm is repeated until at least 60% of the designable domain is removed. The final result will thus have at most 40% of its design domain volume occupied by material. The evolutionary ratio and the initial rejection ratio have been taken as $ER = 0.2\%$ and $RR = 0.2\%$ respectively. The resulted topology is illustrated in Figure 2.17. Unlike the results of the SIMP and homogenisation method there is no grey elements in the ESO results.

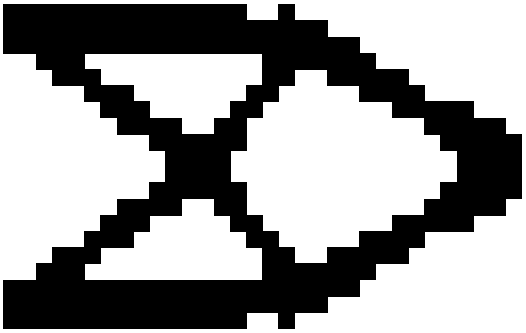

Figure 2.17 The final topology obtained by the ESO method for the SCB problem.

In the final result the volume fraction is 39.69% and the compliance is 56.82. Note that the final value of the objective function obtained here is not directly comparable with the SIMP results due to the penalty power in the SIMP material model. Figure 2.18 shows the topologies at some steady states as well as the final topology.

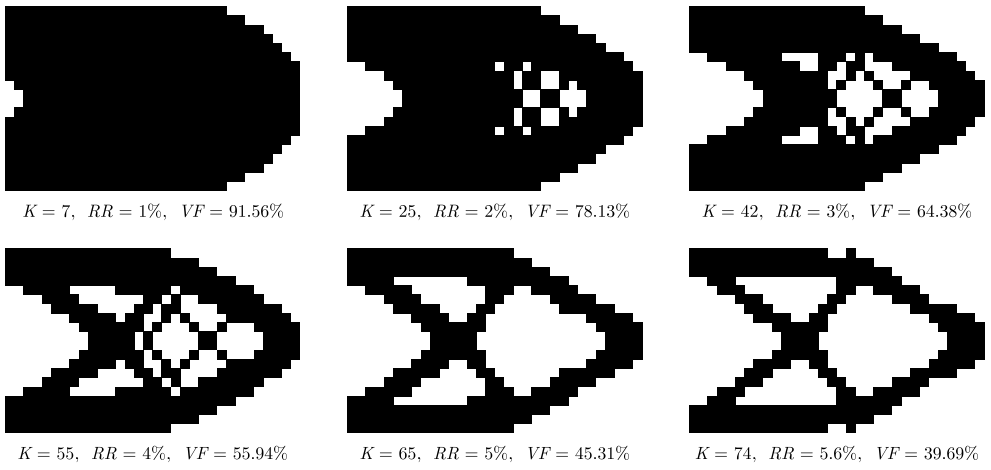

Figure 2.18 The topologies obtained by the ESO method for the SCB problem at steady states. K is the iteration number, RR is the rejection ratio, and VF is the volume fraction.

2.7 Bidirectional evolutionary structural optimisation

The ESO method only removes inefficient parts of the structure. Once an element is removed it can not be reintroduced. This can lead to non-optimal solutions, unless very small evolutionary ratio is used. On the other hand, using small evolutionary ratios will prolong the optimisation procedure. Furthermore in the ESO method one should always start the optimisation procedure from the largest possible designable area fully filled by material. These shortcomings were solved in late 90s when an improved version of the ESO algorithm was introduced by Querin (1997), Querin et al. (1998) and Yang et al. (1999). The improved ESO algorithm was able to add materials to the efficient areas as well as removing inefficient parts. The new approach was hence named as "Bidirectional Evolutionary Structural Optimisation", or simply *BESO*.

Although the idea of the BESO method is a natural extension of the ESO's, the two procedures are different from each other. One of the main differences lies in using the concept of *ground structure* in the BESO method. The ground structure covers the whole designable domain. It contains the solid elements as well as void elements which potentially can be switched to solid elements. In the ESO method one does not need to keep any record of removed elements because there is no hope in recalling them. In BESO, on the other hand, when an element needs to be removed, the procedure turns it off in the ground structure but its geometrical information is not removed.

The ground structure keeps all the information of the void elements as well as solid ones. And when the BESO procedure urges to add an element, the element can be easily added by turning it on in the ground structure. One can assign values of 1 and 0 to elements' design variables to turn them on and off respectively. Using this notation, the minimum compliance design problem will take the following form

$$\begin{aligned} \min_{\mathbf{u},\mathbf{x}} \quad & c(\mathbf{x}) = \mathbf{f}^T\mathbf{u} \\ \text{such that} \quad & \mathbf{K}(\mathbf{x})\mathbf{u} = \mathbf{f}, \\ & x_i \in \{0,1\}, \quad i = 1,\dots,N, \\ & \sum_{i=1}^{N} x_i V_i \leq \bar{V} \end{aligned} \tag{2.33}$$

where V_i is the volume of the i-th element; N is the number of elements, and $\bar{V}$ is the upper limit of materials' volume. Note that (2.33) is exactly similar to (2.10) with $\mathcal{X} = \left\{ x_i \in \{0,1\} | \sum_{i=1}^{N} x_i V_i \leq \bar{V} \right\}$.

2.7.1 Sensitivity number of void elements

In the BESO method, referring to the idea behind the method, the material should be added to the neighbourhood of the most efficient elements. In this method, the elements with the higher sensitivity numbers are nominated to be added. However, because the void elements are not included in finite element analysis, their sensitivity numbers are equal to zero. Hence to add the void elements in the neighbourhood of efficient areas, the sensitivity number of these void elements should be changed to higher values. This can

be done in several ways.

In the BESO algorithm used by Querin (1997), all void elements which has a common node with the most efficient elements gain that element's sensitivity number and subsequently are added to the mesh. Another algorithm has been used by Yang et al. (1999) and Li et al. (1999a) where the nodal displacement of void elements are calculated by extrapolating the nodal displacements of their neighbouring solid elements. The sensitivity number of the void elements can then be calculated using these extrapolated nodal displacements. Other researchers like Huang et al. (2006) directly extrapolated sensitivity numbers.

More recently Huang and Xie (2007) have used a linear filter to extrapolate the sensitivity number of voids. In this approach the filtered sensitivity number of an element i is calculated through

$$\hat{\alpha}_i = \frac{\sum_{j=1}^{N} w_{ij}\alpha_j}{\sum_{j=1}^{N} w_{ij}} \tag{2.34}$$

in which w_{ij} is a linear wighting factor defined as

$$w_{ij} = \max\{0, r_f - r_{ij}\} \tag{2.35}$$

Here r_f is the filtering radius and r_{ij} is the distance between the centroids of elements i and j. Using this filtering scheme, the filtered sensitivity number of every element is affected by sensitivity numbers of all of its neighbouring elements within the radius of r_f. The filtering approach is also useful in overcoming numerical instabilities. This is the subject of section 2.8.

2.7.2 Adding and removing elements

The efficiency of the elements in the BESO method can be measured in the same way as in the ESO method. However adding and removing material needs a different procedure. In the original BESO Querin (1997) and Querin et al. (1998, 2000) used a control parameter name Inclusion Ratio (IR) which controls the amount of adding material. Material is added to the neighbourhood of the elements satisfying the inclusion inequality, $\alpha_i \geq IR \cdot \alpha_{max}$. The steady state is reached when no more elements are nominated for adding or removal. Upon reaching a steady state the inclusion ratio is decreased and the rejection ratio is increased allowing the procedure to continue further. In this algorithm the rejection and inclusion are treated separately and the volume fraction can not be controlled easily.

A new BESO algorithm has been proposed by Huang et al. (2006) and Huang and Xie (2007) in which the volume fraction can be controlled explicitly. In this new algorithm, in each iteration, first the target volume of the next iteration is calculated using a parameter called Evolutionary Volume Ratio (EVR)

$$V^{K+1} = V^K(1 + \text{sign}(\bar{V} - V^K)EVR) \tag{2.36}$$

where $\bar{V}$ is the desired volume of material; V^K is the volume at iteration K

and sign(t) is defined as

$$\text{sign}(t) = \begin{cases} +1 & \text{if} \quad t > 0 \\ 0 & \text{if} \quad t = 0 \\ -1 & \text{if} \quad t < 0 \end{cases} \tag{2.37}$$

After that, the number of adding and removing elements will be calculated through the following steps.

1: Sort the sensitivity numbers in a ascending order ($\alpha_1 \leq \alpha_2 \leq \ldots \leq \alpha_N$)

2: Assign α_{th} equal to the sensitivity number of the element which corresponds to the target volume V^{K+1}, for example if V^{K+1} corresponds to volume of 237 elements, set $\alpha_{th} = \alpha_{237}$. Set $\alpha_{th}^{add} = \alpha_{th}^{del} = \alpha_{th}$.

3: Set V^{add} equal to the volume of void elements with sensitivity numbers greater than α_{th}. Calculate the Admission Ratio $AR = \frac{V^{add}}{V}$ where V is the total volume of solid and void elements.

4: Compare AR with the maximum allowable admission ratio AR_{max} which is a predefined parameter. If $AR \leq AR_{max}$ skip to step 7 otherwise proceed to step 5.

5: Sort the sensitivity numbers of void elements in descending order. Set $V^{add} = AR_{max} \times V$. Among the void elements, set α_{th}^{add} equal to the sensitivity number of the element which corresponds to the volume V^{add}. For example if V^{add} corresponds to volume of 14 elements, set α_{th}^{add} equal to the sensitivity of the 14th void element.

6: Set the volume of removing elements V^{del} equal to $V^{add} + V^{K+1} - V^{K}$.

Among the solid elements, set α_{th}^{del} equal to the sensitivity number of the element which corresponds to the volume V^{del}.

7: Remove the solid elements satisfying $\alpha_i \leq \alpha_{th}^{del}$ and add the void elements satisfying $\alpha_i \geq \alpha_{th}^{add}$.

Figure 2.19 illustrates these steps through a simple example. This procedure needs two tuning parameters, namely EVR and AR_{max}. The first one controls the change in volume in each iteration and the second one controls the maximum amount of adding materials.

step 1

i	α	x	
1	0.05	1	
2	0.12	0	
3	0.15	1	
4	0.27	1	
5	0.33	1	
6	0.33	1	
7	0.35	1	$\leftarrow \alpha_{th}$
8	0.40	0	
9	0.42	1	
10	0.57	0	
11	0.82	0	
12	0.87	1	

steps 2, 3

$V^{add} = 3$

$AR = 3/12$

steps 4, 5

$AR > AR_{max}$

$V^{add} \leftarrow V.AR_{max}$

$V^{add} \leftarrow 2$

void elements

i	α	x	
11	0.82	0	
10	0.57	0	$\leftarrow \alpha_{th}^{add}$
8	0.40	0	
2	0.12	0	

step 6

$V^{del} \leftarrow 8+2-7 = 3$

solid elements

i	α	x	
1	0.05	1	
3	0.15	1	
4	0.27	1	$\leftarrow \alpha_{th}^{del}$
5	0.33	1	
6	0.33	1	
7	0.35	1	
9	0.42	1	
12	0.87	1	

step 7

i	α	x
1	0.05	0
2	0.12	0
3	0.15	0
4	0.27	0
5	0.33	1
6	0.33	1
7	0.35	1
8	0.40	0
9	0.42	1
10	0.57	1
11	0.82	1
12	0.87	1

Figure 2.19 A simple example illustrating the procedure of adding and removing elements in the new BESO algorithm (Huang and Xie 2007). Here V^K and V^{K+1} are equal to the volume of 8 elements and 7 elements respectively. The maximum admission ratio is $AR_{max} = 2/12$. V is equal to the volume of 12 elements.

After discussing different aspects of the BESO method, we can now briefly summarise the BESO algorithm. A brief algorithm is shown in Figure 2.20. This algorithm can be used to solve any optimisation problem provided that suitable sensitivity numbers are used.

1: Discretise the problem's domain.
2: Initialise EVR and AR_{max} and set the upper limit of material's volume $\bar{V}$.
3: **repeat**
4: Perform FE analysis and calculate the sensitivity numbers (α_i) for all elements. At this stage the sensitivity of voids is zero.
5: Calculate the filtered sensitivity numbers (eq. 2.34).
6: Add and remove elements based on the abovementioned algorithm.
7: **until** Convergency criteria
8: **print** the results
9: **end**

Figure 2.20 Algorithm for topology optimisation using the BESO method.

2.7.3 Numerical examples

The application of the BESO method is demonstrated by solving the short cantilever beam problem (Fig. 2.10). Like the example solved by the ESO method, 8-node quadrilateral elements have been used for discretising the domain. As in the BESO method it is not necessary to start from the full design, here we have used an initial guess design with volume fraction of 80%. The maximum allowable material's volume is set equal to 40% of the volume of the design domain. The evolutionary volume ratio and the maximum admission ratio are taken as $EVR = 0.5\%$ and $AR_{max} = 0.5\%$ respectively. The filtering radius r_f in (2.34) is chosen as twice of the size of the elements. The initial and the resulted topologies are illustrated in Figure 2.21.

The mean compliance of the final result is 57.89 which is achieved after 104 iterations. The evolution of the topologies through the BESO method is shown in Figure 2.22.

Figure 2.21 The initial guess design and the final topology obtained by the BESO method for the SCB problem.

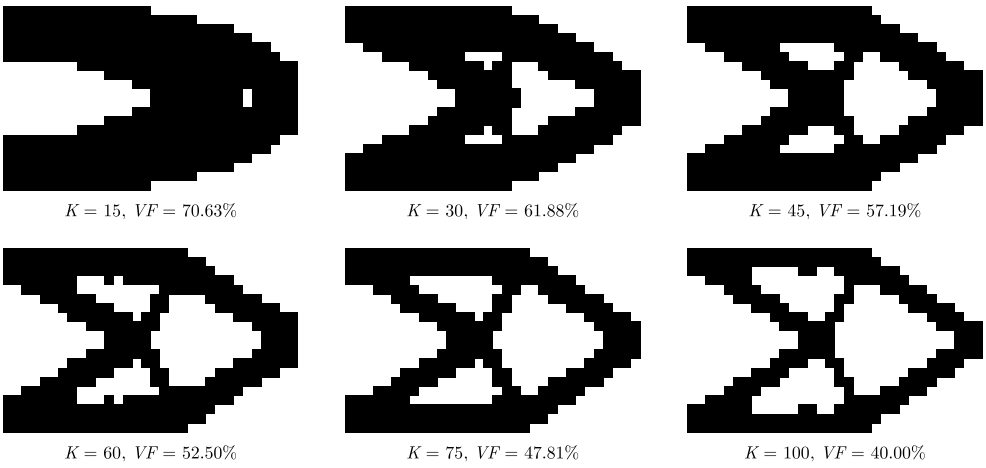

Figure 2.22 The topologies obtained by the BESO method for the SCB problem at different iterations. K is the iteration number and VF is the volume fraction.

2.8 Dealing with numerical instabilities

Numerical instabilities are not uncommon in topology optimisation techniques. These instabilities can affect the optimality of the results and the applicability of the optimisation methods. Sigmund and Petersson (1998) reviewed the possible approaches to treat the three common numerical instabilities in topology optimisation. These three instabilities are known as *checkerboards*, *mesh dependency*, and *local minima*. In what follows we will introduce these numerical instabilities and then briefly discuss the known approaches to overcome them.

2.8.1 Checkerboards

Checkerboard instability refers to the formation of checkerboard-like patterns made of alternating solid and void (or hard and soft) elements. This problem was investigated by Díaz and Sigmund (1995) and Jog and Haber (1996). They demonstrated that the reason for checkerboard formation is that these patterns gain artificially high stiffness due to numerical problems in the mixed formulation of the finite element discretisation. An example of checkerboard patterns is given in Figure 2.23. This topology is obtained by the SIMP method solving exactly the same problem already solved in section 2.5.3. All the parameters have been selected similar to the original problem, but instead of high order 9-node elements, here, 4-node elements have been used.

The homogenisation, the SIMP, the ESO, and the original BESO methods are all prone to the checkerboard instability. This is due to the mixed finite

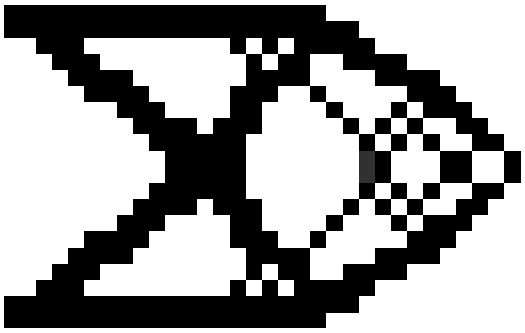

Figure 2.23 The checkerboard instability in a result obtained by the SIMP method for the SCB problem. Instead of 9-node elements, 4-node elements have been used here.

element formulation which is used in all of these methods. However, there are several ways to prevent formation of checkerboard patterns. Here some of the well-known techniques will be introduced.

Using stable elements

Jog and Haber (1996) proposed a patch test to identify unstable elements which can cause the checkerboards formation in topology designs. Also Díaz and Sigmund (1995) presented some guidelines for choosing stable elements. It has been shown in both papers that higher order finite elements can prevent checkerboard formation. In the examples already presented in this chapter, 9-node and 8-node high-order finite elements have been used and no checkerboard pattern has been found in the final topologies. However in the SIMP method this approach does not guarantee a checkerboard-free result if one applies big penalty values (Díaz and Sigmund 1995). Also this approach might not work with the ESO and the BESO methods. Furthermore, using higher order finite elements demands substantially higher computational

effort compared to 4-node elements.

Special types of non-conforming finite elements may also help preventing checkerboard formation. Jang et al. (2003) reported checkerboard-free results using non-conforming 4-node finite elements with their nodes located in the middle of the edges rather than corners.

filtering techniques

The use of filtering techniques to overcome checkerboard formation has been first studied by Sigmund (1994). Although no rigorous proof was ever proposed for this approach, it can successfully prevent checkerboard formation with low computational effort. The filtering scheme is similar to filtering techniques used in image processing. This technique was originally used in the SIMP method. However Li et al. (2001) successfully applied a similar technique to the ESO method. The linear filter used in the BESO algorithm (2.34) is also capable of preventing checkerboard formation. As mentioned before, in the BESO method, the filtering scheme plays an additional role of assigning sensitivity numbers to voids as well.

The short cantilever beam problem is solved here using the SIMP method with 4-node finite elements but sensitivities are filtered using a radius of twice of the size of the elements. In the SIMP method the filtered sensitivities are calculated using the following formula

$$\widehat{\frac{\partial c}{\partial \rho_i}} = \frac{\sum_{j=1}^{N} \rho_j \frac{\partial c}{\partial \rho_j} w_{ij}}{\rho_i \sum_{j=1}^{N} w_{ij}} \tag{2.38}$$

where w_{ij} are weight factors defined in (2.35). The final topology is shown

in Figure 2.24. Note the blurred boundaries in this figure. This is due to the applied filtering scheme which assures a smooth transition from solids to voids exists.

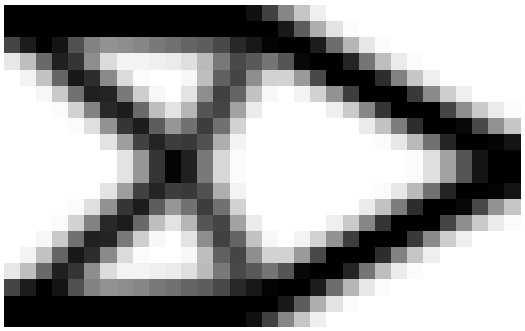

Figure 2.24 Preventing formation of checkerboard patterns using filtering techniques. The filtering radius is twice of the elements' size.

An approach similar to filtering was proposed by Ghabraie (2005) to overcome checkerboards instability in the SIMP method. In this approach the sensitivities at nodes are calculated by averaging the sensitivities of the elements connected to them. Then the sensitivities of the elements are re-calculated by averaging the resulted nodal sensitivities.

Perimeter control

Another way to control checkerboards is to impose a constraint on the perimeter. Between two topologies with the same amount of material the one with less holes has a shorter perimeter. By setting an upper limit on the perimeter, one can thus control the complexity of the resulted topologies and prevent checkerboards. This approach was first used by Haber et al. (1996). Perimeter control was also applied in the BESO method by Yang et al. (2003).

Other techniques

Apart from the abovementioned techniques, several other approaches have been proposed that can deal with the checkerboards problem. Guest et al. (2004), Rahmatalla and Swan (2004), and Matsui and Terada (2004) used nodal sensitivities instead of elemental ones and reported checkerboard-free topologies using the SIMP and the homogenisation methods. Another approach was proposed by Poulsen (2002) in which an additional constraint is added to prevent one-node connected hinges. A simple method was proposed by Kim et al. (2000) which can control the number of holes in the final topology produced by the ESO method and also can solve the checkerboards problem. Using fixed-grid finite element in the ESO method has been investigated by same researchers (Kim et al. 2003) and it was shown that this approach is capable of preventing checkerboard patterns. To overcome the checkerboards problem in the homogenisation method Fujii and Kikuchi (2000) introduced a gravity control function to be added to the objective function. This function is similar to the perimeter control function, however it penalises the intermediate densities as well. It was shown through examples that this approach can solve the mesh dependency and local minima problems as well.

It should be noted here that most of the techniques which are used to deal with the mesh dependency problem can also overcome the checkerboards instability (Sigmund and Petersson 1998).

2.8.2 Mesh dependency

Mesh dependency is the problem of obtaining different topologies for different mesh sizes. This problem is due to nonexistence or sometime non-uniqueness of solutions for the optimisation problem. One approach to overcome this instability is to restrict the feasible space to ensure existence of solutions (Sigmund and Petersson 1998). It is proved by Ambrosio and Buttazzo (1993) that in topology optimisation problems, restricting the perimeter can guarantee the problem to have a solution. The aforementioned perimeter control techniques are thus capable of resolving the mesh dependency problem. Another kind of restriction is through gradient constraints. Petersson and Sigmund (1998) used local bounds on the density slopes and proved the existence of solutions. Via some examples, they also demonstrated the capability of their approach in dealing with other numerical instabilities. A global gradient constraint was proposed by Bendsøe and Sigmund (2003) together with proof of existence of solutions. A different kind of restriction was used by Bourdin (2001). In this paper the densities in the SIMP method are replaced by filtered values which are regulated using a convolution operator. Proof of existence of solutions was given in the paper and it was shown by numerical examples that the approach can deal with mesh dependency and checkerboard anomalies.

Apart from restriction approaches, there are other types of techniques capable of overcoming mesh dependency. Notably the aforementioned sensitivity filter is useful in preventing mesh dependent solutions. In this approach, to obtain mesh independent results one should use absolute filtering radius

values, i.e. the filtering radius should not depend on the elements size.

2.8.3 Local minima

The topology optimisation problems generally are not convex and have several local minima. The gradient based optimisation techniques (like all the four methods presented in this chapter) can therefore be easily trapped in these local minima and miss the global optimum. This generally means that one may get different solutions by applying different parameters or by starting from different initial designs. A common approach to prevent such behaviour is using the so-called continuation technique (Sigmund and Petersson 1998). In this approach an artificial convex version of the problem is modified gradually in some steps to the actual non-convex problem. The problem is solved in each step using the normal topology optimisation technique. Based on experience this approach is more likely to capture the global optimum.

Different types of continuation has been suggested by different researchers. Haber et al. (1996), for example, started from low penalties and increased the penalty gradually to the desired value. Sigmund (1997), on the other hand, used sensitivity filter with a very big radius at the beginning gradually decreasing it. Nevertheless the main problem with the continuation method is the considerable time and effort it needs.

2.9 Choosing an appropriate method

In this chapter we introduced four methods for topology optimisation, namely the homogenisation, the SIMP, the ESO, and the BESO methods. In the previous section we also briefly reviewed some of the approaches to overcome numerical anomalies in these methods. Each of these methods have their own benefits and disadvantages and it is not generally possible to state which method is the best. For a specific problem, one technique might be more appropriate than the other, while the latter might suite another problem better than the former. One should know about the capabilities, advantages, limitations, and shortcomings of these methods and also should have a fair understanding of the optimisation problem in concern, to be able to select a proper method. In many cases it might be even necessary to amend a classic topology optimisation method to fulfil the requirements of a special design problem. Here the characteristics of the introduced methods are discussed briefly and we shortlist these methods based on their properties and our requirements. Then, after explaining the methods and mechanisms of underground excavation design in the next chapter, we will come back to this point to enhance the selected methods to match the special requirements in excavation design.

Starting from the homogenisation method §2.4, the underlying microstructures make the method suitable for designing composite structures. One can define and use different microcells for different types of problems. The method gives real solutions for perforated plates and other problems of this kind. It is made on a sound mathematical basis. However the final results are

complicated and not easily manufacturable. To obtain a simple ISE topology the method is certainly not as good as the other methods. Furthermore the number of design variables needed for a discretised problem are twice or even trice compared to the other methods. Implementation of the homogenisation method is also considerably harder. It is also very difficult to link the homogenisation algorithm with an external finite element solver.

The SIMP method §2.5 is easier to code and implement compared to the homogenisation method. It can work with isotropic materials and the results are close to ISE topologies. In terms of computational time and effort, the method is economical. It is applicable to several types of problems. It can be linked to external finite element packages. The method can easily be protected against numerical instabilities by simple techniques like filtering sensitivities. However the main disadvantage of the SIMP method is the existence of elements with intermediate densities, or grey areas, in final topologies. These areas may not have physical meaning. It is possible to assign a composite design to represent these grey areas, however in this case the manufacturability of the topology decreases. Furthermore employing filtering techniques to overcome mesh dependency and checkerboards results in blurred images with lots of grey elements. On the other hand, using high penalty powers to reduce the grey areas causes convergency problems. One might use a post-processor to sharpen the obtained images, but this approach can change the shape and even the topology qualitatively.

The ESO method §2.6 does not have this blurred images problem and always results in clear pure ISE topologies. The implementation is very simple and it can be linked to external finite element packages almost effortlessly.

It can also solve shape optimisation problems. One of the main advantages of this method is its ability to adopt intuitively derived as well as rigorously derived optimality criteria. This can be very helpful in cases were one cannot establish the sensitivity analysis. The main disadvantage of the method, on the other hand, is that it moves towards the optimum from one direction only. This makes the changes unrecoverable in solution procedure. However this can be even beneficial in certain problems where the nature of the problems enforces a one directional evolution. Another drawback of the ESO method is its vulnerability to small changes in tuning parameters (RR and ER). A small change in these parameters can change the final topology considerably. Finally because of hard killing nature of the ESO procedure, in some cases it might remove all the links between a part and the rest of the structure causing an unstable solution.

The BESO method §2.7 is capable of recovering removed elements. Like the ESO method, the final results are pure ISE topologies. Again like ESO, this method can also use either intuitively or mathematically derived optimality criteria. The method is more robust than ESO and is not very vulnerable to changes in its algorithmic parameters. It can be applied (and has been applied) to a range of physical problems. It is easy to implement and it can be easily linked to an external finite element engine for analysis. It is generally faster than the ESO method. The optimisation problem which is being solved by the BESO method can be well established and mathematically stated. It can be easily formulated to solve shape optimisation problems. Moreover, the inbuilt filtering technique can protect the method against numerical anomalies. However like the ESO method, this method

can also lead to unstable solutions, although this can be prevented by special considerations in the algorithm or by weakening the inefficient elements instead of totally removing them (soft killing approach).

For problems in underground excavation design, the abilities of the homogenisation method in dealing with microcells may not be very useful. Furthermore making use of the capabilities of commercial powerful finite element packages is a highly beneficial point which this method can not enjoy. On the other hand, the ease of linking with these finite element packages is an important advantage. In this regard, the ESO method and the BESO method are more advantageous than the SIMP method and the homogenisation method. Also noting the importance of shape optimisation for optimising the shape of the underground openings, the ESO and the BESO methods are more beneficial for our case than the SIMP method. The clear topology obtained by the ESO and the BESO methods is another advantage for these methods comparing to the SIMP method. Between the ESO and the BESO methods, the latter is more robust and converges faster. This makes the BESO method the most proper choice for the types of problems to be considered in this thesis. However for some non-linear problems which are history dependent, ESO's one directional optimisation approach matches the nature of the problem. Hence for these types of problems (which are to be dealt with in Chapter 7) the ESO method is the most suitable optimisation method.

The next chapter gives a brief review of modelling geomechanical materials and designing issues in underground excavations. After that, became more acquainted with the subject, in Chapter 4 we will tailor the BESO method in accordance to the recognised demands and enhance its capabili-

ties to deal with underground excavation problems.

CHAPTER 3

Designing underground excavations

Unfortunately, soils are made by nature and not by man, and the products of nature are always complex.

Terzaghi 1936

3.1 Differences between structural and excavation design

In excavation design, unlike structural engineering, the goal is to achieve particular objectives by perturbing a pre-existing natural system whose behaviour is not known *a priori*. The main differences between structural and underground excavation designs can be summarised into the following items:

- ▷ properties of the ground material need to be estimated and their behaviour is more complex
- ▷ in-situ stresses need to be estimated
- ▷ the loading sequence is different.

In this chapter different ways to estimate mechanical properties of geomaterials and in-situ stresses are briefly discussed. In the last section an introduction to the application of topology optimisation techniques in underground excavation is presented with a brief review of the previously published papers in this context.

3.2 Mechanical properties of soil

The material properties of geomechanical materials can be estimated directly or indirectly. In the direct approach the material properties are determined through laboratory and in situ tests. In the indirect approach the material properties are estimated using empirical or theoretical correlations, combining the properties of discontinuities and intact material through analytical or numerical methods, and back-analysis (Zhang 2005).

Soil is generally a cohesive frictional granular medium. In excavation design, because the size of the opening is much larger than the size of soil particles, the soil mass can be assumed as a continuum. For simplification, the stress-strain relationship is idealised. Common idealisations are elastic-perfectly plastic, elastic-strain hardening plastic, and elastic-strain softening plastic models.

The elastic-perfectly plastic model consists of three basic elements (Yu 2006):

1. The elastic stress-strain relation

2. The *yield criterion*, which distinguishes the elastic and plastic regions

3. The *plastic flow rule*, which defines the plastic relation between stress and strain

The elasticity parameters of soil can be determined via laboratory or in-situ tests. Assuming the material is isotropic, the elastic behaviour of the soil can be completely described if the values of the Young's modulus (E) and Poisson's ratio (ν) are determined. Alternatively one can find the value of the shear modulus (G) instead of the Poisson's ratio. The shear modulus is related to the Young's modulus and the Poisson's ratio through the following expression

$$G = \frac{E}{2(1+\nu)} \tag{3.1}$$

The value of the shear modulus does not depend on the drainage conditions of the soil (Craig 2004).

The Young's modulus can be estimated using the results of the triaxial test. It is also possible to determine the Young's modulus through in-situ tests. This can be achieved by, for example, applying load increments to a test plate. The shear modulus can be determined by using pressuremeter on site (Craig 2004).

Several yielding criteria have been proposed for soils among which the Mohr-Coulomb criterion is the oldest and the most widely used. This criterion was proposed by Coulomb (1773). It considers both friction and cohesion effects. According to the Mohr-Coulomb criterion the yielding starts when the shear stress reaches the following value

$$|\tau| = c + \sigma_n \tan\phi \tag{3.2}$$

where c is the cohesion and ϕ is the internal angle of friction. In terms of principal stresses $\sigma_1 \geq \sigma_2 \geq \sigma_3$, the Mohr-Coulomb yield function takes the form

$$f = (\sigma_1 - \sigma_3) - (\sigma_1 + \sigma_3)\sin\phi - 2c\cos\phi = 0 \tag{3.3}$$

The Mohr-Coulomb yield criterion is illustrated in Figure 3.1.

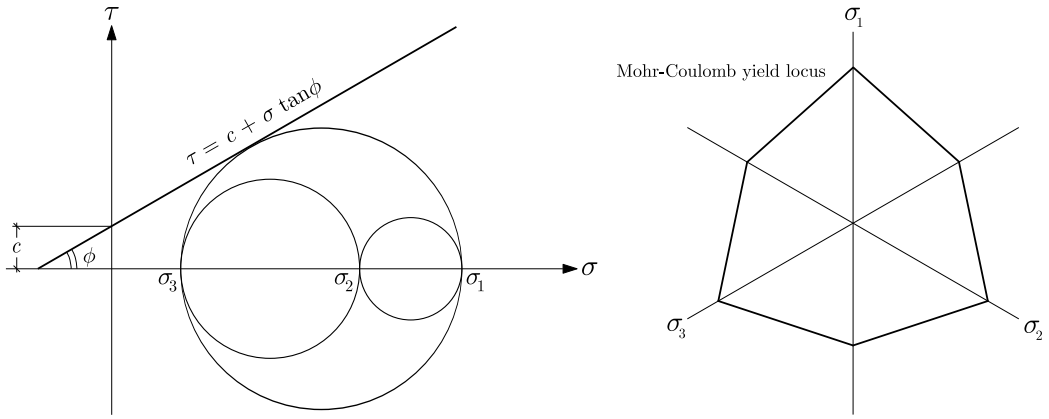

(a) (b)

Figure 3.1 Mohr-Coulomb yield surface. a) on $\tau - \sigma$ plane; b) on deviatoric plane ($\pi-$plane).

The cohesion and the friction angle of soils can be determined through the triaxial or direct shear tests.

The plastic flow rule is commonly assumed to be in the following form (Yu 2006; Kempfert and Gebreselassie 2006)

$$\mathrm{d}\epsilon_{ij}^{p} = \mathrm{d}\lambda \frac{\partial g}{\partial \sigma_{ij}} \tag{3.4}$$

where ϵ_{ij}^{p} represents the plastic strain; $\mathrm{d}\lambda$ is a positive scalar, and $g(\sigma_{ij}) = 0$ is known as *plastic potential function*. In the case of associative flow rule, the plastic potential function is the same as the yield function ($g = f$). Otherwise

the flow rule is non-associative.

It is usually assumed that the plastic potential function for the Mohr-Coulomb model has the same form as the yield function, but the friction angle is replaced by the smaller dilation angle ψ (Yu 2006). This implies a non-associated flow rule. The relationship between the angles of friction and dilation is referred to as stress-dilatancy equation. One of the most successful stress-dilatancy models is the following proposed equation

$$\psi = 1.25(\phi - \phi_{cs}) \tag{3.5}$$

in which ϕ_{cs} is the friction angle at the critical state (Yu 2006).

3.3 Material properties of rock

Naturally rocks contain discontinuities which affect their mechanical behaviour. Unlike soils, and most other engineering materials, because of these discontinuities, rocks do not generally satisfy the continuum assumption. A clear distinction should be made between rock material and the generally discontinuous structure of rock in nature. The rock material between two discontinuities is usually referred to as *intact rock*. On the other hand the in situ medium involving intact rock blocks separated by discontinuity sets is known as *rock mass*.

For different structures, the size of representative rock mass domain which is affected by the structure might be different. The simulation of the behaviour of a rock mass depends on the size of the structure in concern, or

the problem's domain. The influence of the domain size is illustrated in Figure 3.2. When the representative size is adequately smaller than the discontinuity spacing, the properties of intact rock can be used to model the rock mass behaviour. In this case the rock medium can be assumed as a continuum, usually with isotropic behaviour. For problem domains containing few discontinuities, the continuum assumption is not valid. In such cases, the behaviour of the rock mass is highly influenced by its discontinuities and is not isotropic. When the size of the problem domain is much larger than the blocks of rocks, the rock mass can be seen as heavily jointed. In this case, like soil, an equivalent continuum can be used to model the rock mass (Brady and Brown 2006).

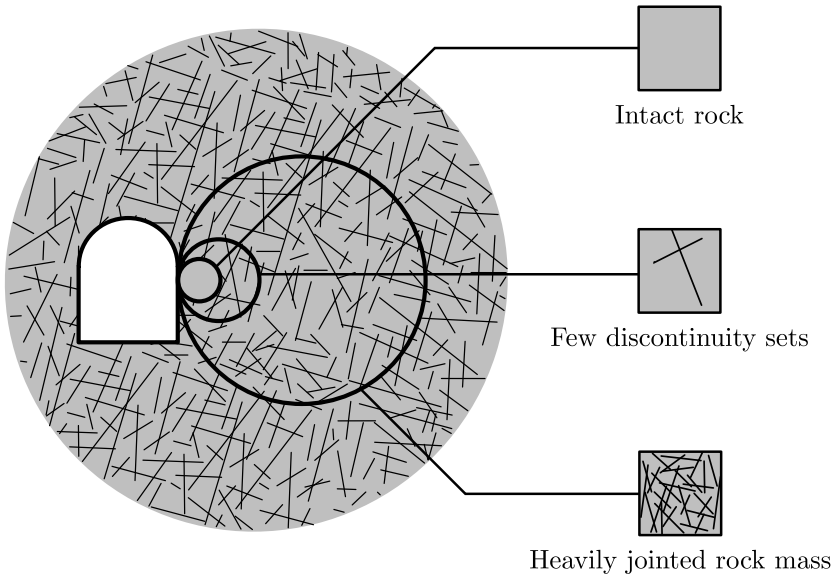

Figure 3.2 The influence of scale on rock mass behaviour.

The rock material (intact rock) in most cases shows a brittle behaviour where strength reduces significantly upon reaching a specific stress level (Hoek et al. 1997). One of the popular failure criteria for intact rock has

been suggested by Hoek and Brown (1980). This criterion is empirical and can be expressed in the following form

$$\sigma_1' = \sigma_3' + \sigma_c \left(m_i \frac{\sigma_3'}{\sigma_c} + 1 \right)^{\frac{1}{2}} \tag{3.6}$$

where σ_1' and σ_3' are the major and minor effective stresses at failure respectively; σ_c is the uniaxial compressive strength of the intact rock, and m_i is a material constant which only depends on the rock type.

The uniaxial (or unconfined) compressive strength σ_c and the material constant m_i can be determined by laboratory tests. The most reliable values for these parameters can be derived from the triaxial test results on rock core samples (Hoek et al. 1997). The values of unconfined compressive strength of rocks may vary from 1MPa for weak rocks like claystone to more than 300MPa for Quartzite or some igneous rocks like granite and syenite (Zhang 2005). The material constant m_i is a dimensionless parameter which depends on mineralogy, composition and grain size of the rock material (Hoek et al. 1992). The typical values for this parameter varies between 4 for claystone to 33 in case of granite (Hoek and Brown 1980; Hoek et al. 1997).

3.3.1 Discontinuities in rocks

The main difference between rock masses and other engineering materials is the existence of discontinuities in them. The word *discontinuity* is a general term referring to any kind of separation in rock mass which effectively has no tensile strength. This compromises faults, bedding planes, joints, ...

The shear strength of discontinuities is assumed to obey the Mohr-Coulomb criterion (3.2). However in discontinuities the parameter c does not have the same physical meaning (cohesion) as it has in soils (Hoek et al. 1997). Conservatively c can be eliminated in this case (Hudson and Harrison 1997). The Mohr-Coulomb criterion can thus be simplified as $|\tau| = \sigma_n \tan\phi$. The tensile strength of discontinuities is zero by definition and the compressive strength is equal to that of intact rock.

The geometrical and mechanical properties of discontinuities are mostly the main factors that govern the mechanical properties of rock masses. However obtaining a clear picture of discontinuities within a rock mass in most cases is not possible. The designers often should rely on the information obtained from borehole cores. One of the most important aspects of discontinuity occurrence is the ratio of intact rock pieces in core samples. The *Rock Quality Designation* (RQD) is a quantitative measurement of this ratio developed by Deere et al. (1967). RQD is defined as the ratio of intact rock pieces longer than 100mm in the total length of core expressed in percentage.

3.3.2 Rock mass classification

Mechanical properties of rock masses depend on both rock material (intact rock) and discontinuity sets. Rock mass classification schemes can provide an initial quantitative estimation of overall rock mass properties. The use of rock mass classification schemes can be considerably beneficial in the early design stages of projects when detailed information on rock mass is barely available. These schemes, however, should not be used as a replacement of

more sophisticated design procedures.

The *Rock Mass Rating* (RMR) and the *Rock Tunnelling Quality Index* (Q) are two well-known rock mass classification schemes for tunnels. The RMR classification is introduced by Bieniawski (1976) under the name of 'Geomechanics Classification System'. Since then this system was refined several times by Bieniawski (1989). The RMR system uses the following six parameters:

1. Uniaxial compressive strength of the rock material (σ_c).
2. Rock quality designation (RQD).
3. Spacing of discontinuities.
4. Condition of discontinuities (roughness, separation, etc.).
5. Ground water condition.
6. Orientation of discontinuities.

The rating values corresponding to the these items are derived from the tables provided by Bieniawski (1989) and added together. These tables can also be found in Hoek et al. (1997, p. 35). The final value of RMR is in the range of 0 to 100. Higher values imply better rock quality.

The Tunnelling Quality Index (Q) was proposed by Barton et al. (1974) for estimating rock mass properties and tunnel support requirements. It is defined as

$$Q = \frac{RQD}{J_n} \times \frac{J_r}{J_a} \times \frac{J_w}{SRF} \tag{3.7}$$

where RQD is the rock quality designation; J_n is the joint set number; J_r is the joint roughness number; J_a is the joint alteration number; J_w is the joint water reduction factor, and SRF is the stress reduction factor. All these factors can be extracted from the tables provided by Barton et al. (1974). These tables can also be found in Hoek et al. (1997, p. 41). The value of Q can change from 0.001 to 1,000 on a logarithmic scale.

3.3.3 Strength of rock mass

For rock masses with few dominant discontinuities, the strength of discontinuities should be explicitly considered in terms of a shear strength criterion. In this case failure of the intact rock blocks can be estimated by using Hoek-Brown criterion for intact rock (3.6), while the shear strength of discontinuities can be determined by using Mohr-Coulomb criterion.

For heavily jointed rock masses, on the other hand, the strength of discontinuities can be implicitly combined with the strength of intact rock to provide a single failure criterion for the rock mass. In this case the overall behaviour of the rock mass can be assumed isotropic. Such criterion can also be used to model the behaviour of a weak rock mass with a single dominant shear zone or fault. In these rock masses the behaviour of the weak rock mass can be predicted by the rock mass failure criterion and the strength of the dominant discontinuity should be explicitly modelled using a shear strength criterion (Hoek et al. 1992).

Among different empirical failure criteria presented for jointed rock masses, the Hoek-Brown criterion will be introduced here. This criterion was origi-

nally proposed by Hoek and Brown (1980). A modified version of this criterion was later presented by Hoek et al. (1992). In the most general form, the Hoek-Brown failure criterion can be expressed in the following form (Hoek et al. 1997)

$$\sigma_1' = \sigma_3' + \sigma_c \left(m_b \frac{\sigma_3'}{\sigma_c} + s \right)^a \tag{3.8}$$

This form incorporates both the original and the modified versions of the criterion. Here m_b is the material constant for the rock mass, and s and a are constants which depend on the characteristics of the rock mass. σ_1' and σ_3' are the major and minor effective stresses at failure respectively and σ_c is the uniaxial compressive strength of the intact rock.

The original Hoek-Brown criterion can be achieved by substituting $a = 0.5$ in (3.8). This criterion works well with most rocks with good quality when the rock mass strength is controlled by tightly interlocking angular rock pieces (Hoek et al. 1997).

The modified criterion is more suitable for poor quality rock masses where the tight interlocking has been disturbed. Such rock masses have no tensile strength or 'cohesion'. The modified criterion can be obtained by setting $s = 0$ in (3.8) and thus reads

$$\sigma_1' = \sigma_3' + \sigma_c \left(m_b \frac{\sigma_3'}{\sigma_c} \right)^a \tag{3.9}$$

To estimate the values of the parameters m_b, s, and a in (3.8), Hoek et al. (1997) proposed some formulae which relate these parameters to the rock mass classification indexes of RMR and Q through a new index called

Geological Strength Index (GSI). The value of m_b can be estimated from

$$\frac{m_b}{m_i} = \exp\left(\frac{GSI - 100}{28}\right) \tag{3.10}$$

For s and a the following relations have been proposed

$$s = \begin{cases} \exp\left(\frac{GSI-100}{9}\right) & \text{for } GSI > 25 \\ 0 & \text{for } GSI < 25 \end{cases} \tag{3.11}$$

$$a = \begin{cases} 0.5 & \text{for } GSI > 25 \\ 0.65 - \frac{GSI}{200} & \text{for } GSI < 25 \end{cases} \tag{3.12}$$

Values of $GSI > 25$ indicate rock masses of good to reasonable quality (when original criterion should be used) and the values of $GSI < 25$ are related to rock masses of poor quality (when modified criterion should be used).

The GSI value can be related to the RMR and Q indexes. Hoek et al. (1997) proposed the following relationship to estimate the GSI value from the latest version of RMR (the 1989 RMR classification)

$$GSI = RMR - 5, \quad \text{for } RMR > 23 \tag{3.13}$$

For $RMR < 23$ this classification cannot be used to estimate GSI value. For such cases the modified Q index should be used in the following formula

$$GSI = 9 \ln Q' + 44 \tag{3.14}$$

where Q' is the modified quality index which is calculated as

$$Q' = \frac{RQD}{J_n} \times \frac{J_r}{J_a} \tag{3.15}$$

For extremely poor rock masses GSI takes the value of about 10 and for intact rock the value of GSI reaches 100 (Hoek et al. 1997).

3.4 In-situ and induced stresses

3.4.1 In-situ stresses

In underground excavations, the stresses involved in the analysis are not applied but rather induced by disrupting the in-situ stresses. These in-situ stresses are tolerated by rocks or soils prior to excavating. Measuring or estimating the pre-existing in-situ stresses is thus a necessary step in any underground excavation design. The in-situ stresses in ground materials are mainly caused by the weight of overlying strata and the locked-in tectonic stresses (Hoek et al. 1997).

The in-situ stresses might be directly measured via several measurement methods description of which is beyond the scope of this text. It is also possible to estimate the in-situ stresses through empirical correlations, stress measurements in the past, and analytical models. The vertical stress, σ_v, can be usually safely estimated as the weight of overlying strata (Terzaghi et al. 1996; Hoek and Brown 1980)

$$\sigma_v = \gamma z \tag{3.16}$$

where γ is the unit weight of the overlying material and z is the depth below surface. The ratio of averaged horizontal stress to vertical stress is usually denoted by k such that

$$\sigma_h = k\sigma_v = k\gamma z \tag{3.17}$$

In soil mechanics the ratio of the in-situ vertical to horizontal stress is usually referred to as 'coefficient of earth pressure at rest' (Jáky 1944; Terzaghi et al. 1996; Craig 2004; Mitchell and Soga 2005) and is denoted by k_0. A couple of relations have been proposed by various authors to estimate the value of k_0 in soils which all depend on the friction angle and possibly the *overconsolidation ratio* (OCR). A commonly used relationship for normally consolidated soils is the simplified version of the formula proposed by Jáky (1944),

$$k_0 = 1 - \sin\phi' \tag{3.18}$$

in which ϕ' is the effective friction angle of the soil. The typical range of 18° to 43° for ϕ' in (3.18) results in k_0 values ranging from 0.31 to 0.67 (Terzaghi et al. 1996). For overconsolidated soils, Mayne and Kulhawy (1982) proposed the following relationship.

$$k_0 = (1 - \sin\phi')(\mathrm{OCR})^{\sin\phi'} \tag{3.19}$$

For rocks the typical value of γ is 2700kg/m^3 (Hoek and Brown 1980). For the value of k and the horizontal stress σ_h several correlations have been suggested by different authors (Zhang 2005). Considering the worldwide in-situ

rock stress data, Hoek and Brown (1980) provided the following bounding limits for k

$$\frac{100}{z} + 0.3 < k < \frac{1500}{z} + 0.5 \tag{3.20}$$

It can be seen that unlike soils, in rocks the ratio of averaged horizontal to vertical stress (k) depends on depth (z) rather than material properties.

3.4.2 Induced stresses

Excavating underground openings disturbs the in-situ stresses in the vicinity of the opening. The stress release caused by excavation will cause the stresses to redistribute around the opening. Determining these induced stresses is thus an unavoidable step if one wants to model the responses of the ground in which an opening is excavated. This can be done by using simplified analytical models or numerical modelling.

For openings of simple shapes, e.g. circle, a closed form solution might be available in the literature assuming elastic or elasto-plastic ground response. A handful of such analytical solutions can be found in Yu (2000).

In general cases, the induced stresses can be calculated using numerical methods. Some of the most widely used numerical methods in excavation designs are *Finite Difference Methods* (FDM), *Finite Element Method* (FEM), *Boundary Element Method* (BEM), *Discrete Element Method* (DEM), and *Discrete Fracture Network* (DFN) (Jing and Hudson 2002; Jing 2003). These methods can be divided into two groups (Jing and Hudson 2002; Jing 2003): continuum methods including FDM, FEM and BEM, and discontinuum meth-

ods including DEM and DFN. The first group of methods is more suitable for analysing rock masses with no discontinuities or with many discontinuities. These methods are also suitable for rock masses containing few discontinuities, providing the behaviour of these discontinuities are explicitly simulated. The second group are more appropriate for moderately jointed rock masses.

Because all the previously discussed topology optimisation techniques are based on finite element method, in this thesis only the finite element method has been used for numerical analysis.

3.5 Support and reinforcement design

In regard to mechanical stability, excavating an opening will cause two major effects on the rock mass environment. Firstly the stress release caused by excavation will allow the surrounding rock to displace and squeeze the opening. Secondly the stress tensor on the boundary of the opening would have no shear stress and two of the normal (principal) stresses would lie on the boundary surface with the other one (normal to the boundary surface) dissipating (Hudson and Harrison 1997).

Influenced by the first effect, the rock mass might deform as a whole or some rock blocks might move towards the opening separately. If the displacement exceeds certain limits failure can happen either partially or globally. The second effect involves a significant disruption of the in-situ stresses. This may increase the magnitude of the deviatoric stresses leading the rock or soil mass to fail.

In order to maintain the stability of the excavation and prevent such failures, in most cases, it is necessary to improve the integrity and stiffness of the rock or soil mass by means of additional reinforcement or support. In rock mechanics there is a distinction between the two terms *reinforcement* and *support* (Brady and Brown 2006; Hudson and Harrison 1997). The term 'reinforcement' is used when one improves the overall rock mass behaviour from within the rock mass so that the rock supports itself. Techniques such as cable bolts, rock bolts, and ground anchors come under this category. On the other hand, the term 'support' refers to use of structural elements such as timber or steel liners which are installed inside the excavation to support the rock mass externally.

This thesis is not going to deal with different types and available techniques for stabilisation of excavations. Instead the mechanical effects of reinforcement or support on the rock mass are concerned in the numerical models. To understand these effects and to model them correctly, it is essential to know how the support and reinforcement systems interact with the ground.

3.5.1 Ground and support interaction

As excavation proceeds, the tunnel face advances into the rock mass. This can happen, for example, by cycles of drilling and blasting. This advancement changes the stress distribution in the surrounding rock mass. If one monitors the stress and displacement of a fixed point in rock mass ahead of the tunnel face, these values will change dramatically as the tunnel face approaches this point. Consider the case depicted in Figure 3.3 where the displacements of

the point P is being monitored. The graph in this figure shows the normalised values of inward radial displacement of P against its distance from the tunnel face.

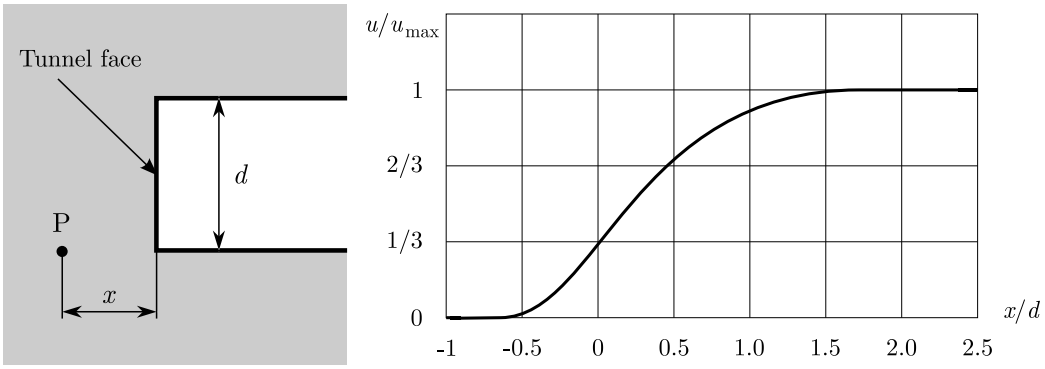

Figure 3.3 The change in displacement of a floor point as the tunnel advances.

The radial displacement of P starts when the tunnel face reaches the distance of around one half of the tunnel diameter. At tunnel face, the displacement reaches about one third of its final value. Finally when the tunnel face passes the point, in a distance about one and a half tunnel diameter, the inward displacement of the point reaches its final value (Brady and Brown 2006; Hoek et al. 1997).

In order to illustrate the disruption caused by excavation, a simple case of a circular tunnel with the initial radius of r_0 is considered here. The stress field is assumed to be hydrostatic with the value of p_0 and the tunnel is assumed to be long and straight enough to validate the plane strain assumption. The rock mass behaviour is idealised as elastic-perfectly plastic and the yielding is assumed to be governed by Mohr-Coulomb criterion.

An internal pressure p_i acts inside the tunnel. Initially this pressure is equal to the in-situ stress, i.e. $p_i = p_0$. As the excavation proceeds, the

internal pressure decreases. The rock mass surrounding the tunnel starts to yield as the internal pressure becomes less than a critical value. This critical pressure can be calculated as (Hoek et al. 1997)

$$p_{cr} = \frac{2p_0 - \sigma_{cm}}{1+k} \tag{3.21}$$

where σ_{cm} and k are two parameters depending on friction angle and cohesion defined as

$$\sigma_{cm} = \frac{2c\cos\phi}{1-\sin\phi} \tag{3.22}$$

and

$$k = \frac{1+\sin\phi}{1-\sin\phi} \tag{3.23}$$

For values of $p_i > p_{cr}$ the rock mass behaviour is elastic. In this range the inward radial displacement can be expressed as

$$u_e = \frac{r_0(1+\nu)}{E}(p_0 - p_i) \tag{3.24}$$

with ν and E denoting the Poisson's ratio and Young's modulus of the rock mass. For $p_i \leq p_{cr}$ the rock mass will undergo a plastic deformation. The radius of the plastic zone takes the following form (Hoek et al. 1997)

$$r_p = r_0 \left(\frac{2\left(p_0(k-1) + \sigma_{cm}\right)}{(1+k)\left((k-1)p_i + \sigma_{cm}\right)} \right)^{\frac{1}{k-1}} \tag{3.25}$$

Using this, the total radial displacement can be calculated as

$$u = \frac{r_0(1+\nu)}{E} \left(2(1-\nu)(p_0 - p_{cr}) \left(\frac{r_p}{r_0}\right)^2 - (1-2\nu)(p_0 - p_i) \right) \tag{3.26}$$

Figure 3.4 shows the variation of inward radial displacement against the internal pressure p_i using (3.24) and (3.26).

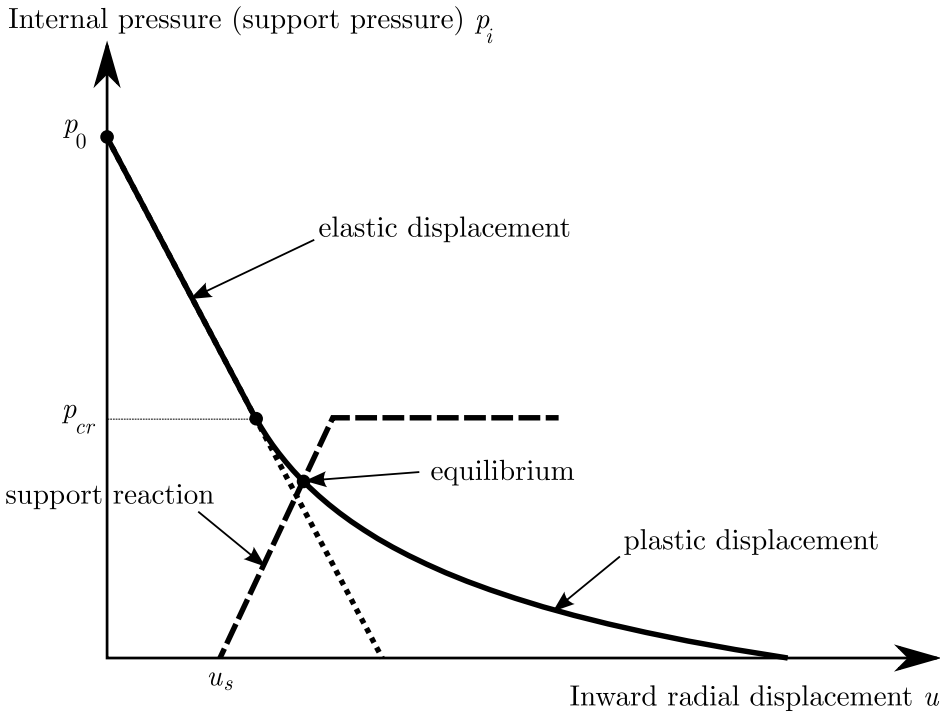

Figure 3.4 Ground response curve and support interaction.

As depicted in Figure 3.4 the displacements are elastic for $p_i > p_{cr}$ and as the internal pressure decreases further the rock yields and plastic displacement occurs.

Now suppose that some support system is installed as the tunnel face advances. As illustrated in Figure 3.3, displacement at the tunnel face itself would be approximately one third of the final displacement. That means before installing any support system some deformation has already occurred. Assume that the displacement at the time of support installation is u_s. After adding the support system, as the displacement increases the support stress becomes greater. The reaction of the support stress acts as an internal pres-

sure and is added to p_i. In Figure 3.4 the reaction of the support system is depicted using dashed line. As the radial displacement increases further, the internal pressure decreases while the support pressure increases. Once the ground response curve meets the support reaction curve equilibrium is achieved (Fig. 3.4). If the support system yields before reaching equilibrium or if the support is installed too late, the support will be ineffective.

3.5.2 Modelling rock support and rock reinforcement

According to definition, supports act externally. The effect of supports can thus be modelled by adding an external pressure acting outward on the supported parts of the opening boundary. The magnitude of this pressure is equal to the pressure tolerated by the support system in opposite direction.

Rock reinforcement on the other hand, act internally and their modelling is more complicated. In terms of the effect on the host rock, generally two types of reinforcement systems can be recognised. The first group applies a confining pressure to the reinforced parts of the rock mass. Ungrouted anchored bolts come in this category. The second group reinforces the rock mass by adding elements which are generally stronger and stiffer than the host rock and particularly can withstand tensile stresses. Grouted rock bolts and dowels are examples of this type of reinforcement.

To simulate the effect of reinforcement one approach is to model the reinforcing elements explicitly. Such models can provide a high level of accuracy but at the same time might take considerable effort and time to be analysed. Another simpler approach is to include reinforcement effect by con-

sidering a stiffer and stronger material for reinforced areas of the rock mass. Properties of this 'reinforced material' can be calculated through homogenisation method (Bernaud et al. 1995, 2009). This is specially useful in case of fully grouted rock bolts. Using this approach the reinforcement optimisation problem reduces to finding the optimal distribution of the reinforced material. Such problems can be easily solved by topology optimisation techniques. Throughout this thesis a simplified homogenised reinforced material is used to simulate the effect of reinforcement.

3.6 Optimising underground excavations

Finding the best shape of the opening and the best arrangement and topology of the rock reinforcement are two vital and challenging steps in excavation design. Both of these optimisation problems can be addressed by topology optimisation techniques presented in Chapter 2. This might however involve significant complexities due to complex behaviour of ground materials and the differences in the loading sequence between structural and excavation problems.

In this section a review of the published works on using topology and shape optimisation techniques in underground excavations is presented. The pre-excavation stress fields have been modelled by applying remote distributed forces on a large finite element mesh. The finite element mesh should be large enough to eliminate the boundary effects. A linear elastic material model have been used for rock and soil in all of these papers and the ground media

has been assumed as an isotropic continuum.

3.6.1 Shape optimisation of the openings

Ren et al. (2005) employed the ESO method to optimise the shape of underground openings assuming linear elastic behaviour for ground material. They used the mean principal compressive stress defined as

$$\bar{\sigma} = \frac{\sigma_1 + \sigma_2 + \sigma_3}{3} \tag{3.27}$$

as the efficiency measurement in the ESO procedure. The effect of the weight of ground material was assumed to be negligible in this paper. The results were verified with theoretical solutions in simple cases where a single opening is under biaxial principal stresses. In this case the optimum shape is known to be an ellipse with axial lengths matching the in-situ stress ratio (Ren et al. 2005). The optimum shape of a tunnel intersection was also presented in this paper. This optimal tunnel intersection shape is reintroduced in Figure 3.5.

A more detailed review of the procedure used in this paper will be presented in Chapter 7.

3.6.2 Reinforcement optimisation around tunnels

Topology optimisation of the reinforcement around underground openings was first studied by Yin et al. (2000). The objective function used in this

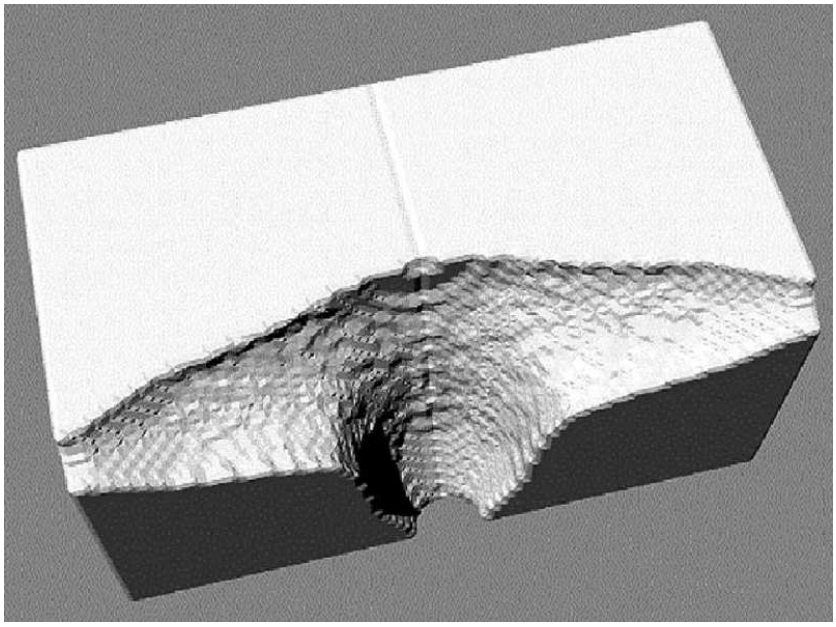

Figure 3.5 The optimum shape for two intersecting tunnels obtained by Ren et al. (2005).

paper is the external work along the tunnel wall defined as

$$W(\mathbf{u}) = \int_{\Gamma} \mathbf{t} \cdot \mathbf{u} \mathrm{d}\Gamma \tag{3.28}$$

where $\mathbf{u}$ is the displacement vector; Γ is the tunnel's boundary, and $\mathbf{t}$ is the negating surface traction on tunnel's boundary prior to excavation. In this paper the tunnels were assumed to be deep enough so that the difference of the gravity force is negligible. By assuming linear elasticity, the superposition principle can be applied. The loading of the tunnel is thus equivalent to the superposition of two other load cases: the initial in-situ stresses and the negating surface traction $\mathbf{t}$. Figure 3.6 illustrates this idea.

In their approach Yin et al. (2000) used the homogenisation method to minimise W. They considered a square base cell of unit length made of

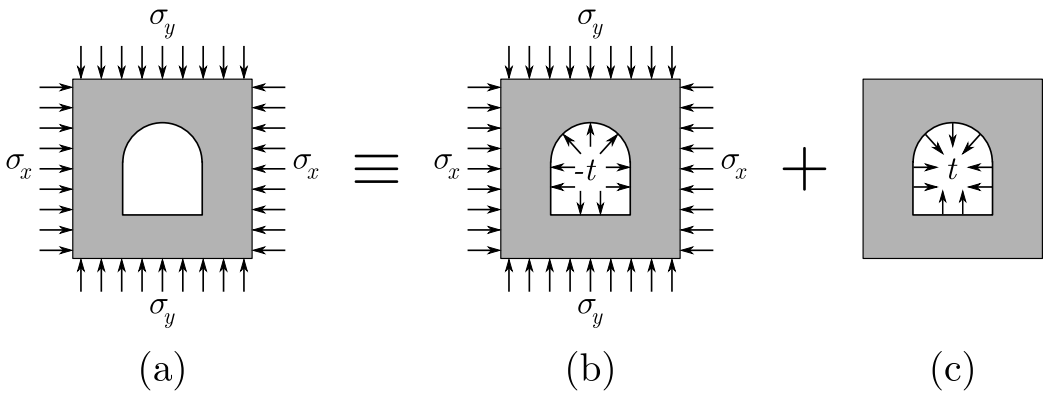

Figure 3.6 Using superposition principle to analyse a deep tunnel: a) A tunnel under remote stresses; b) the pre-excavation stress state; c) the negating surface traction.

reinforced material consisting a smaller square of size $\mu < 1$ in its centre made of original rock. The reinforcement material was assumed to be linear elastic with a Young's modulus five times that of rock mass.

Yin and Yang (2000a) solved the reinforcement optimisation problem for tunnels in layered rock structures. This structure may consist of layers of hard and soft rocks with different Young's moduli. Reinforcement optimisation of tunnels in four different structures were studied by Yin and Yang (2000a), namely, isotropic soft, hard/soft, soft/hard, and hard/soft/hard rock structures.

Yin and Yang (2000a) employed the SIMP method to minimise displacement based objective functions. These objective functions correspond to the sum of the relative displacements around the opening boundary. In their paper, linear elastic behaviour is assumed for both original and reinforced rock. The following power-law interpolation scheme is used for stiffness tensor

$$E_{ijkl}(\rho) = \rho^p E^{(r)}_{ijkl} + (1 - \rho^p) E^{(o)}_{ijkl} \tag{3.29}$$

where ρ is the relative density; p is the penalty factor, and $E^(r)_{ijkl}$ and $E^(o)_{ijkl}$ are stiffness tensors of reinforced rock and original rock respectively.

In their paper, Yin and Yang (2000a) have solved two examples in the four rock structures considered with deep tunnel assumption (neglecting the weight of rocks). In another example, however, they included the gravity force for a tunnel in isotropic media.

The same approach was applied by Yin and Yang (2000b) to find the optimum reinforcement topology minimising the floor and side wall heaves of a tunnel in homogeneous rock. In this paper the weight of rock material was neglected and the tunnel was considered under stress biaxiality.

The reinforcement optimisation of underground tunnels was also studied by Liu et al. (2008). Different displacement based objective functions were considered in this paper. To solve the optimisation problem, Liu et al. (2008) used the BESO method within a fixed grid finite element framework. The fixed-grid finite element prevents the formation of checkerboard patterns and smoothens the final topologies. The following interpolation scheme is used in this paper

$$E_{ijkl}(\eta) = \eta E^{(r)}_{ijkl} + (1-\eta)E^{(o)}_{ijkl} \tag{3.30}$$

where η is the design variable field changing between 0 and 1. The two material phases differ in their Young's moduli. The sensitivity numbers for the BESO method can be calculated by using (3.30) in the results of sensitivity analysis of the objective functions. More information on this issue can be found in Chapter 4 where the application of the BESO method in solving bi- or multi-material problems is discussed.

CHAPTER 4

Tailoring topology optimisation algorithm for underground excavation problems

4.1 Introduction

As mentioned in the previous chapter, in excavation design, the shape of the opening and the topology of the rock reinforcement can be optimised by state-of-the-art topology optimisation techniques.

In reinforcement optimisation the material is changing between normal rock and reinforced rock. The material interpolation scheme is thus different from solid-void design and the choice of material interpolation scheme is more critical (Bendsøe and Sigmund 2003). Unlike material-void design, in bi-material (or multi-material) problems, the ratio of the Young's moduli of the two material phases is a finite number. This might lead to convergency difficulties specially when the elasticity properties of the two materials are very close to each other.

For optimising the shape of the opening, it is necessary to find the boundary of the opening. The material elements on this boundary may change

to voids and the voids on the inner side of this boundary may change to material elements. As discussed before, the SIMP and the homogenisation methods are not very suitable for shape optimisation, because the material-void boundary is not well definable in these methods. In applying ESO or BESO methods a normal material-void interpolation scheme would be sufficient provided that the switches between material and void elements are limited to the elements at the boundary of the opening. This restriction generally assures that the topology of the opening will not change.

In this chapter a reformulation of the BESO technique is presented. To derive the sensitivity numbers, a general approach is presented which is based on sensitivity analysis. The characteristics of the proposed BESO technique is then tuned and improved to match these special requirements and considerations.

4.2 Deriving sensitivity numbers

In the BESO method, the sensitivity number of the i-th element, α_i is an indicator of the change in the objective function due to switching the material in that element. We thus try to evaluate the change in objective function due to a change in an element.

Suppose that the objective function f is a function of design variables, $f = f(\mathbf{x})$ which is to be minimised. By changing the value of the design variable of the i-th element from 1 to 0, the vector of design variables will change from $\mathbf{x}$ to $\overset{-i}{\mathbf{x}}$. Using Taylor series of f in the neighbourhood of $\overset{-i}{\mathbf{x}}$ one

can write

$$f(\mathbf{x}) = f(\overset{-i}{\mathbf{x}}) + \frac{\partial f}{\partial x_i}(x_i - \overset{-i}{x}_i) + \frac{\partial^2 f}{\partial x_i^2}(x_i - \overset{-i}{x}_i)^2 + \cdots \tag{4.1}$$

Substituting $x_i = 1$ and $\overset{-i}{x}_i = 0$ in this equation, one can get the following first-order approximation for the change in f due to weakening (or removing) the i-th element

$$\underset{-i}{\Delta} f = f(\overset{-i}{\mathbf{x}}) - f(\mathbf{x}) = -\frac{\partial f}{\partial x_i} \tag{4.2}$$

The parameter $\underset{-i}{\Delta} f$ represents the effect of the imposed change on the objective function and thus can be used to define the sensitivity number of the i-th element.

By increasing the value of the design variable in the i-th element from 0 to 1, the vector of design variables will change from $\mathbf{x}$ to $\overset{+i}{\mathbf{x}}$. Again using Taylor series and substituting $x_i = 0$ and $\overset{+i}{x}_i = 1$ the following first-order approximation for the change in f due to strengthening (or adding) the i-th element can be achieved.

$$\underset{+i}{\Delta} f = f(\overset{+i}{\mathbf{x}}) - f(\mathbf{x}) = \frac{\partial f}{\partial x_i} \tag{4.3}$$

The two equations (4.2) and (4.3) can be summarised into the following relation

$$\underset{i}{\Delta} f = \begin{cases} \frac{\partial f}{\partial x_i} & \text{if } x_i = 0 \\ -\frac{\partial f}{\partial x_i} & \text{if } x_i = 1 \end{cases} \tag{4.4}$$

Using (4.4) if one strengthens the i-th element ($x_i = 0$) and weakens the j-th element ($x_j = 1$), the change in the objective function can be approximated

to $\Delta f = \frac{\partial f}{\partial x_i} - \frac{\partial f}{\partial x_j}$. In a minimisation problem the lowest value of Δf is desirable. One can thus conclude that the weak elements with the lowest value of $\frac{\partial f}{\partial x_i}$ are more desirable to be strengthened. While in case of elements with the strong material, the most desirable to be weaken is the one with the greatest value of $\frac{\partial f}{\partial x_j}$.

Based on this discussion the following definition for sensitivity numbers can be proposed

$$\alpha_i = -\frac{\partial f}{\partial x_i}, \quad i = 1, 2, \ldots, n \tag{4.5}$$

Using this definition and noting the above discussion, the weak elements with the highest sensitivity number are more desirable to be strengthened (are the most *efficient* elements). And the strong elements with the lowest sensitivity number are more desirable to be weaken (are the least *efficient* elements). This definition is consistent with the original definition of sensitivity numbers and efficiency of elements in the BESO method.

For the compliance minimisation problem one can substitute $\frac{\partial c}{\partial x_i}$ from (2.14) in (4.5) to get the following expression

$$\alpha_i = \mathbf{u}_i^T \frac{\partial \mathbf{K}_i}{\partial x_i} \mathbf{u}_i, \quad i = 1, 2, \ldots, n \tag{4.6}$$

To calculate the sensitivities one needs to know the value of the parameter $\frac{\partial \mathbf{K}_i}{\partial x_i}$. This value depends on the material interpolation scheme in use.

4.3 Linear material interpolation

The simplest material interpolation between two materials is a linear interpolation formulated below

$$E_{ijkl}(x) = E^{(1)}_{ijkl} + x(\xi)(E^{(2)}_{ijkl} - E^{(1)}_{ijkl}), \quad \xi \in \Omega \tag{4.7}$$

where E_{ijkl} is the interpolated stiffness tensor; $E^{(m)}_{ijkl}$ stands for elasticity tensor of the m-th material and $x(\xi)$ is the design variable field with $0 \leq x(\xi) \leq 1$. ξ indicates the coordinates and Ω is the design domain.

The elasticity tensor E_{ijkl} for isotropic materials is a function of two material constants, namely Young's modulus E and Poisson's ratio ν. If one assumes that the Poisson's ratio is same for the two material phases, the equation (4.7) can be expressed in terms of Young's modulus only. Supposing a similar finite element discretisation for displacement and design variable fields, (4.7) can be simplified to

$$E_i(x_i) = E^{(1)} + x_i(E^{(2)} - E^{(1)}), \quad i = 1, 2, \ldots, n \tag{4.8}$$

where E_i is the Young's modulus of the i-th element, and $E^{(1)}$ and $E^{(2)}$ are the moduli of elasticity of the two materials. x_i represents the design variable of the i-th element, and n is the number of finite elements. Here it is assumed that $E^{(1)} < E^{(2)}$ which means the first material is weaker than the second. Note that by setting $E^{(2)} = \bar{E}$ and $E^{(1)} = 0$, a material-void interpolation can be derived from (4.8).

Using the linear elasticity assumption, the element level stiffness matrix

$\mathbf{K}_i$ can be expressed as

$$\mathbf{K}_i(x_i) = \frac{E_i(x_i)}{\bar{E}}\bar{\mathbf{K}}_i \tag{4.9}$$

where $\bar{E}$ is the modulus of elasticity of the base material and $\bar{\mathbf{K}}_i$ is the stiffness matrix of the i-th element when it is made of the base material. For two-material problems the base material can be chosen as either of the two materials. Differentiating with respect to x_i, one will get

$$\frac{\partial \mathbf{K}_i}{\partial x_i} = \frac{\partial E_i}{\partial x_i}\frac{\bar{\mathbf{K}}_i}{\bar{E}} = \frac{\partial E_i}{\partial x_i}\frac{\mathbf{K}_i}{E_i} \tag{4.10}$$

which can be simplified further by substituting $\frac{\partial E_i}{\partial x_i}$ from (4.8) to give

$$\frac{\partial \mathbf{K}_i}{\partial x_i} = (E^{(2)} - E^{(1)})\frac{\mathbf{K}_i}{E_i} \tag{4.11}$$

Now substituting $\frac{\partial \mathbf{K}_i}{\partial x_i}$ from (4.11) into (4.6), one can calculate the following sensitivity numbers for the compliance minimisation problem.

$$\alpha_i = \begin{cases} \frac{E^{(2)}-E^{(1)}}{E^{(1)}}\mathbf{u}_i^T\mathbf{K}_i\mathbf{u}_i & \text{for the weak material } (x_i = 0) \\ \frac{E^{(2)}-E^{(1)}}{E^{(2)}}\mathbf{u}_i^T\mathbf{K}_i\mathbf{u}_i & \text{for the strong material } (x_i = 1) \end{cases} \tag{4.12}$$

The linear interpolation scheme with the above sensitivity numbers may not result in recognisable topologies in two-material problems when a filtering technique is implemented. The reason lies on the coefficients $\frac{E^{(2)}-E^{(1)}}{E^{(1)}}$ and $\frac{E^{(2)}-E^{(1)}}{E^{(2)}}$ which increase the sensitivity number of the weak elements and decrease the sensitivity number of strong elements. The BESO routine sorts the elements based on their sensitivity numbers and then switches the elements

based on their ranking. Hence, what is important in BESO is the ranking of sensitivity numbers, not their numerical value. When no filtering is employed the neighbouring elements will not affect each other and thus the algorithm works fine. However, when the filter is turned on the sensitivity numbers of neighbouring elements affect each other and combine together. In this case, the two coefficients $\frac{E^{(2)}-E^{(1)}}{E^{(1)}} > \frac{E^{(2)}-E^{(1)}}{E^{(2)}}$ give more weight to the weak elements. This scatters the materials and ultimately results in non-recognisable topologies. This problem is illustrated in the numerical examples solved at the end of this chapter (see Figure 4.4a and Figure 4.5a).

The linear material interpolation is thus only suitable when no filtering is employed and the sensitivity numbers of the two materials does not influence each other. However, one can use non-linear interpolation schemes or adjust the weight factors to overcome this shortcoming. The following sections propose such interpolation schemes.

4.4 Power-law interpolation

The common material interpolation scheme used in the SIMP method is the power-law interpolation (2.23). A similar interpolation scheme can be used in the BESO method (Huang and Xie 2009).

$$E_i(x_i) = x_i^p \bar{E}, \quad i = 1, 2, \ldots, n \tag{4.13}$$

where $\bar{E}$ is the Young's modulus of the base material and $p \geq 1$ is a penalty factor.

Similarly for two-material problems, assuming a similar Poisson's ratio for the two materials, the following interpolation scheme can be defined

$$E_i(x_i) = E^{(1)} + x_i^p(E^{(2)} - E^{(1)}), \quad i = 1, 2, \ldots, n \tag{4.14}$$

The material-void interpolation scheme (4.13) can be derived from (4.14) by setting $E^{(2)} = \bar{E}$ and $E^{(1)} = 0$. Setting $p = 1$ results in a linear interpolation.

Now by calculating $\frac{\partial E_i}{\partial x_i}$ from (4.14) and substituting into (4.10) one can write

$$\frac{\partial \mathbf{K}_i}{\partial x_i} = p x_i^{(p-1)}(E^{(2)} - E^{(1)})\frac{\mathbf{K}_i}{E_i} \tag{4.15}$$

Using this equation in (4.6), the following sensitivity numbers can be defined

$$\alpha_i = \begin{cases} p x_i^{p-1} \frac{E^{(2)} - E^{(1)}}{E^{(1)}} \mathbf{u}_i^T \mathbf{K}_i \mathbf{u}_i & \text{if } x_i = 0 \\ p x_i^{p-1} \frac{E^{(2)} - E^{(1)}}{E^{(2)}} \mathbf{u}_i^T \mathbf{K}_i \mathbf{u}_i & \text{if } x_i = 1 \end{cases} \tag{4.16}$$

Assuming $p > 1$ the above equation can be simplified to

$$\alpha_i = \begin{cases} 0 & \text{if } x_i = 0 \\ p \frac{E^{(2)} - E^{(1)}}{E^{(2)}} \mathbf{u}_i^T \mathbf{K}_i \mathbf{u}_i & \text{if } x_i = 1 \end{cases} \tag{4.17}$$

This equation suggests that the objective function dose not change by strengthening an element. In order to overcome this, one can use a small positive value $x_{min} > 0$ instead of 0 for the weak material. In this case the above

equation can be rewritten as

$$\alpha_i = \begin{cases} p\frac{x_{min}^{p-1}(E^{(2)}-E^{(1)})}{E^{(1)}+x_{min}^{p}(E^{(2)}-E^{(1)})}\mathbf{u}_i^T\mathbf{K}_i\mathbf{u}_i & \text{for the weak material } (x_i = x_{min}) \\ p\frac{E^{(2)}-E^{(1)}}{E^{(2)}}\mathbf{u}_i^T\mathbf{K}_i\mathbf{u}_i & \text{for the strong material } (x_i = 1) \end{cases} \tag{4.18}$$

As the actual value of the sensitivity numbers are not important in BESO, for further simplification, the above definition can be divided by p.

4.5 An alternative interpolation scheme

When one uses power-law interpolation, it is necessary to introduce an extra parameter, x_{min}, in order to evaluate the change in objective function due to strengthening an element. This requirement is resulted from the fact that the slope of the power-law interpolation (4.14) vanishes at $x_i = 0$. On the other hand, the slope of the interpolation curve at the other end ($x_i = 1$) is always a positive value. This gives different weights to the sensitivity numbers of the weak and the strong materials.

The alternative material interpolation scheme proposed by Stolpe and Svanberg (2001) overrides these shortcomings. This material interpolation can be expressed in the following form

$$E_i(x_i) = E^{(1)} + \frac{x_i}{1+q(1-x_i)}(E^{(2)} - E^{(1)}), \quad i = 1, 2, \ldots, n \tag{4.19}$$

where q plays the same role as p in (4.14). Using $q = 0$ will result in a linear interpolation (without penalty) while any positive value for q penalises the

intermediate design variables.

Differentiating (4.19) with respect to design variables, one would get

$$\frac{\partial E_i}{\partial x_i} = \frac{(E^{(2)} - E^{(1)})(1+q)}{[1+q(1-x_i)]^2} \tag{4.20}$$

which can then be substituted in (4.10) to give

$$\frac{\partial \mathbf{K}_i}{\partial x_i} = \frac{(1+q)}{[1+q(1-x_i)]^2} \frac{(E^{(2)} - E^{(1)})}{E_i} \mathbf{K}_i \tag{4.21}$$

Using (4.21) in (4.6), the sensitivity number for the i-th element can be defined as

$$\alpha_i = \begin{cases} \frac{1}{1+q} \frac{(E^{(2)}-E^{(1)})}{E^{(1)}} \mathbf{u}_i^T \mathbf{K}_i \mathbf{u}_i & \text{for the weak material } (x_i = 0) \\ (1+q) \frac{(E^{(2)}-E^{(1)})}{E^{(2)}} \mathbf{u}_i^T \mathbf{K}_i \mathbf{u}_i & \text{for the strong material } (x_i = 1) \end{cases} \tag{4.22}$$

4.6 Modified linear interpolation

In §4.3 it was mentioned that the sensitivity numbers resulted form linear interpolation are not suitable for two-material problems. This is due to the two weight factors $\frac{(E^{(2)}-E^{(1)})}{E^{(1)}} > \frac{(E^{(2)}-E^{(1)})}{E^{(2)}}$ which result in higher sensitivity numbers for weak elements. Moreover, for voids where $E^{(1)} \to 0$, one would get $\frac{(E^{(2)}-E^{(1)})}{E^{(1)}} \to \infty$ which can cause numerical problems.

In order to overcome these issues, we redefine the sensitivity numbers in

(4.12) as

$$\alpha_i = \begin{cases} E^{(1)}(E^{(2)} - E^{(1)})\mathbf{u}_i^T \mathbf{K}_i \mathbf{u}_i & \text{for weak material } (x_i = 0) \\ E^{(2)}(E^{(2)} - E^{(1)})\mathbf{u}_i^T \mathbf{K}_i \mathbf{u}_i & \text{for strong material } (x_i = 1) \end{cases} \tag{4.23}$$

In this definition, for the case of solid-void design, setting $E^{(1)} \to 0$ will result in $\alpha_i \to 0$ when $x_i = 0$. Note that no extra parameter need to be defined in (4.23).

As in the BESO method the ranking of the sensitivity numbers is what is important, the sensitivity numbers defined in (4.23) are equivalent to (4.22) with q satisfying the following equation

$$q = \frac{E^{(2)}}{E^{(1)}} - 1 \tag{4.24}$$

The results are also equivalent to the definition provided in (4.18) if p and x_{min} satisfy the following equation

$$x_{min}^{1-p} = \left(\frac{E^{(2)}}{E^{(1)}}\right)^2 + x_{min}\left(1 - \frac{E^{(2)}}{E^{(1)}}\right) \tag{4.25}$$

For example, assuming $\frac{E^{(2)}}{E^{(1)}} = 5$ and $x_{min} = 0.001$, one would get $q = 4$ and $p = 1.466$ from (4.24) and (4.25) respectively.

The sensitivity numbers formulated in (4.18), (4.22), and (4.23) were all calculated for compliance minimisation. If one chooses another objective function, similar procedures may be followed to define corresponding sensitivity numbers.

4.7 Filtering sensitivity numbers

In case of solid-void designs, the mechanical responses of voids cannot be evaluated from finite element analysis and the sensitivity number of voids should be extrapolated from surrounding elements. Filtering sensitivity numbers is one common approach for such extrapolations. In two-material problems there is no need for extrapolating sensitivity numbers. However, even in this case, filtering the sensitivity numbers is beneficial.

Filtering technique is capable of overcoming numerical anomalies such as checkerboards and mesh dependency. More details on this issue have been provided in §2.8. Moreover, filtering smoothens the resulted topologies. This generally reduces the complexities in the final design and increases its applicability.

The filtering scheme used in this text is a linear filter which has been previously introduced in §2.7.1. This filtering scheme has been formulated in equation (2.34) which is repeated here

$$\hat{\alpha}_i = \frac{\sum_{j=1}^{N} w_{ij}\alpha_j}{\sum_{j=1}^{N} w_{ij}} \qquad [2.34]$$

in which $w_{ij} = \max\{0, r_f - r_{ij}\}$ is a linear wight factor. r_f is the filtering radius and r_{ij} is the distance between the centroids of the elements i and j.

After calculating the filtered sensitivity numbers from (2.34), these values should be used instead of the original sensitivity numbers for the rest of calculations in each iteration.

4.8 Switching elements

An overview of a recently proposed element switching procedure in BESO was presented in §2.7.2. One of the capabilities of the BESO algorithm is that it can start from design points with higher or lower volumes than the specified volume constraints. Although starting from a full initial design usually leads to better results, the optimisation procedure is hard to follow when the volume is changing. In this case the value of the objective function in two steps with two different volumes are not comparable to each other. Different performance indices were used by some researchers to make this sort of comparisons possible (Yang et al. 2003; Querin 1997). However, using these performance indices, one can not easily express what optimisation problem is being solved. In order to reduce the complexity of the algorithm and for verification purposes, in this thesis we always start the BESO algorithm from a feasible design point and keep the volume fractions constant. In this manner the value of the objective function at any iteration is always comparable to the other iterations and the problem which is being solved can be expressed mathematically. It is trivial that one can use any proper element switching procedure in the BESO method without this restriction we imposed here.

In order to keep the volume constant, in each iteration, the number of elements being switched from 0 to 1 should be the same as the number of elements being switched from 1 to 0. In other words, if one determines the i-th element to be weakened (be switched from 1 to 0), another element, say j, should be strengthened (be switched from 0 to 1). The change in the

objective function, f, could be thus estimated as

$$\Delta f = \underset{-i}{\Delta} f + \underset{+j}{\Delta} f \tag{4.26}$$

In a minimisation problem one would try to make Δf negative with the largest possible absolute vale, whilst in a maximisation problem a large positive value for Δf is desirable.

For the compliance minimisation problem, considering the sensitivity numbers defined in (4.18), (4.22), or (4.23), by switching a weak and a strong element, the change in the objective function can be estimated as

$$\Delta c = \alpha_S - \alpha_W \tag{4.27}$$

where α_S and α_W are the sensitivity numbers of the strong and the weak elements respectively. The maximum drop in the objective function can thus be achieved by switching the weak elements with the greatest sensitivity numbers and the strong elements with the lowest sensitivity numbers. Based on this idea, the switching algorithm first sorts all the sensitivity numbers. Then the weak element with the highest sensitivity number and the strong element with the lowest sensitivity number are selected. If the sensitivity number of the selected weak element is higher than that of the strong element, the material of these two elements are exchanged. This switching procedure continues with the remaining elements until the lowest sensitivity number among strong elements become greater than the highest sensitivity number among weak elements. In this case $\alpha_S > \alpha_W$ and any exchange in the

elements' material will cause a positive Δc which is not desirable.

To prevent sudden alterations of the design, the maximum number of exchanges in the elements is limited to a predefined value. This value is referred to as *move limit* and indicated by m hereafter. The above mentioned switching procedure is not repeated more than m times inside each iteration. Selecting a large move limit will let the algorithm to update many elements in one step which generally reduces the accuracy of targeting the optimum but increases the speed. On the other hand, using a small move limit the solution procedure takes longer time, but with a higher chance of finding an optimum path. Selecting small move limits can be helpful in verification stages.

When in an iteration no more changes take place or when the same series of changes are repeated in two following iterations, the result is assumed to be converged. In the latter case, the design with the lowest objective function among the last two is reported as the optimum result. To prevent infinite loops the maximum number of iterations should also be limited.

4.9 Shape optimisation using BESO

In the BESO and ESO methods, the design variables have discrete values. The boundaries between different material phases are thus easily recognisable and definable in these methods. This property is very helpful when one wants to use these methods for shape optimisation. In shape optimisation only the shape of the boundaries between material phases should change and the

topology of the design should remain constant. This requirement is essential in shape optimisation of the opening.

In order to maintain the topology of the opening, the boundary between materials and voids should first be recognised by the shape optimisation algorithm. This boundary is defined as the set of all nodes which belong to at least two elements, one of which solid and the other one void. In mathematical notation this can be expressed as

$$\mathcal{B}_h = \{j \,|\exists e_m \in \mathcal{M} \wedge e_v \in \mathcal{V} : j \in e_m \cap e_v\} \tag{4.28}$$

where $\mathcal{B}_h$ denotes the boundary of the opening, and $\mathcal{M}$ and $\mathcal{V}$ are the set of solid elements and void elements respectively. After finding $\mathcal{B}_h$, the *active set*, $\mathcal{A}$, is defined as the set of all elements containing at least two boundary nodes

$$\mathcal{A} = \{e \,|\exists i, j \in \mathcal{B}_h : i \neq j \wedge i, j \in e\} \tag{4.29}$$

An example of boundary and active set definition is illustrated in Figure 4.1.

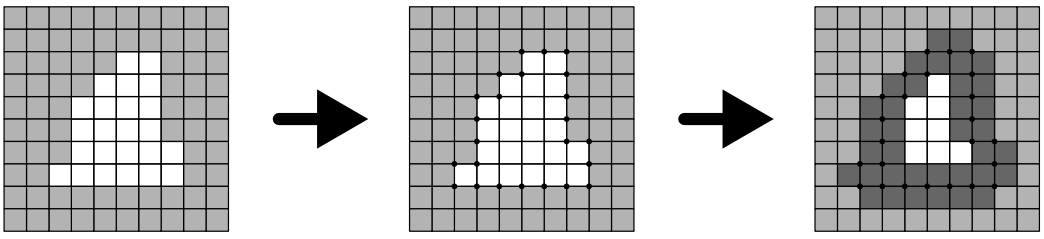

Figure 4.1 Finding boundary nodes and active set for shape optimisation.

The elements in the active set are the only elements allowed to be changed. This approach limits the changes to the boundary of the opening. Note that

this limitation cannot always assure a constant topology. An illustrative example is provided in Figure 4.2. However this case can only happen if the boundary forms a concave shape. Specially using the previously discussed filtering scheme smoothens the boundaries and prevents concave opening shapes. Note that the move limit should be adjusted for shape optimisation because the number of designable elements in this case is much smaller than general topology optimisation problems.

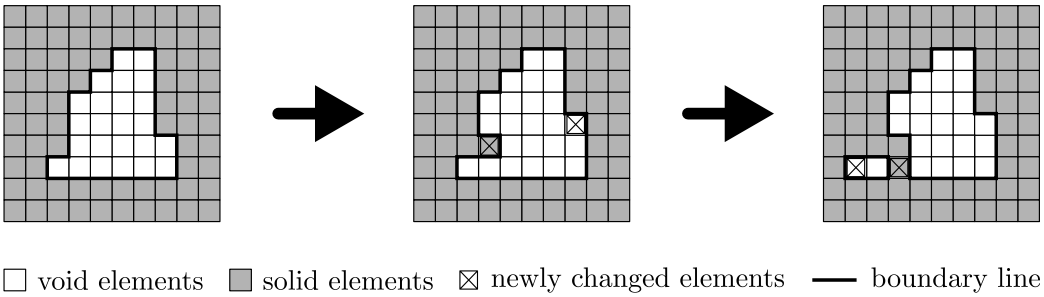

Figure 4.2 Possible alteration of topology in case of concave shapes.

4.10 Mathematical background of the proposed BESO algorithm

The compliance minimisation problem solving by the proposed BESO method can be formulated as

$$\mathbb{P}_d : \min \left\{ c(\mathbf{u}, \mathbf{x}) \middle| \mathbf{Ku} = \mathbf{f}, E_i = E_i(x_i), x_i \in \{0, 1\}, \sum_{i=1}^{n} x_i V_i = \bar{V} \right\} \quad (4.30)$$

where V_i is the volume of the i-th element and $\bar{V}$ is the desired volume of the stronger material (or solids); $E_i(x_i)$ indicates the material interpola-

tion scheme; $\mathbb{P}_d$ is a constrained discrete optimisation problem. The unconstrained continuous (relaxed) version of $\mathbb{P}_d$ takes the following form

$$\mathbb{P}_c : \min \{c(\mathbf{u}, \mathbf{x}) \,|\mathbf{K}\mathbf{u} = \mathbf{f}, E_i = E_i(x_i), x_i \in [0, 1]\} \tag{4.31}$$

Note that the continuous problem $\mathbb{P}_c$ does not have any constraint on volume and thus its solution is the whole design domain filled with the stronger material.

Using this notation the BESO algorithm can be seen as a two-phase procedure. Firstly it updates the design based on $\mathbb{P}_c$. Then the solution is modified to match the requirements defined in $\mathbb{P}_d$.

The first phase involves finding a *descent vector* for $\mathbb{P}_c$. The proposed BESO algorithm uses the *steepest descent method* to find a descent vector. The steepest descent vector for a general objective function f is defined as $\mathbf{d} = -\nabla f$ where the gradient is calculated with respect to design variables. This calculation is based on a linear approximation and provides a linear convergence (Herskovits 1995). Following the discussion in §4.2 and noting (4.5), one can clearly observe that the steepest descent vector is equivalent to sensitivity numbers. Denoting the steepest descent vector by $\mathbf{d}$ one can write

$$d_i = -\frac{\partial c}{\partial x_i} = \mathbf{u}_i^T \frac{\partial \mathbf{K}_i}{\partial x_i} \mathbf{u}_i, \quad i = 1, 2, \ldots, n \tag{4.32}$$

As seen in previous sections, the value of $\frac{\partial \mathbf{K}_i}{\partial x_i}$ and thus $\mathbf{d}$ depend on the material interpolation scheme in use. It can be seen from this equation and (4.6) that $d_i = \alpha_i$.

The second phase involves modifying the descent vector to satisfy the

constraints in $\mathbb{P}_d$. The modified vector is denoted by $\hat{\mathbf{d}}$ and referred to as *move vector* hereafter. Using the move vector, the new set of design variables are calculated through the following update scheme

$$\mathbf{x}^{K+1} = \mathbf{x}^K + \hat{\mathbf{d}}^K \tag{4.33}$$

in which the superscripts K denotes the K-th iteration. Noting the condition $x_i \in \{0, 1\}$ one can deduce that the only possible values for $\hat{d}_i$ are -1, 0, and 1 corresponding to respectively weakening (removing), not changing, and strengthening (adding) the i-th material. The algorithm for deriving the move vector has been discussed in §4.8. If for example the move limit is selected as $m = 1$ then the relationship between $\hat{\mathbf{d}}$ and $\mathbf{d}$ can be expressed mathematically as

$$\hat{d}_i = \text{sign}\left[(1 - x_i)d_i - \max\{(1 - x_i)d_i\}\right] + \text{sign}\left[x_i d_i - \min\{x_i d_i\}\right], \quad i = 1, 2, \ldots, n \tag{4.34}$$

where sign(t) is defined in (2.37).

For a higher order approximation and convergence, instead of the steepest descent method, one can use Newton's algorithm with the following equation for $\mathbf{d}$

$$\nabla^2 f \; \mathbf{d} = -\nabla f \tag{4.35}$$

This algorithm provides at least a quadratic convergence for an unconstrained problem (Herskovits 1995). However solving (4.35) is complex and time consuming as it involves calculating $\nabla^2 f$ and solving an n-order system of

equations where n is the number of design variables.

4.11 Illustrative examples

In this section, we solve the short cantilever beam (SCB) problem with two materials to illustrate the different aspects of the proposed algorithm in this chapter. The design domain, loading conditions, supports and the initial distribution of materials are depicted in Figure 4.3. The ratio of the elasticity moduli of the two materials is assumed as $\frac{E^{(2)}}{E^{(1)}} = 5$. In all of the following examples the volume of the stronger material is taken as 960 elements or 40% of the whole domain. The remaining parts of the design domain should be filled by the weaker material.

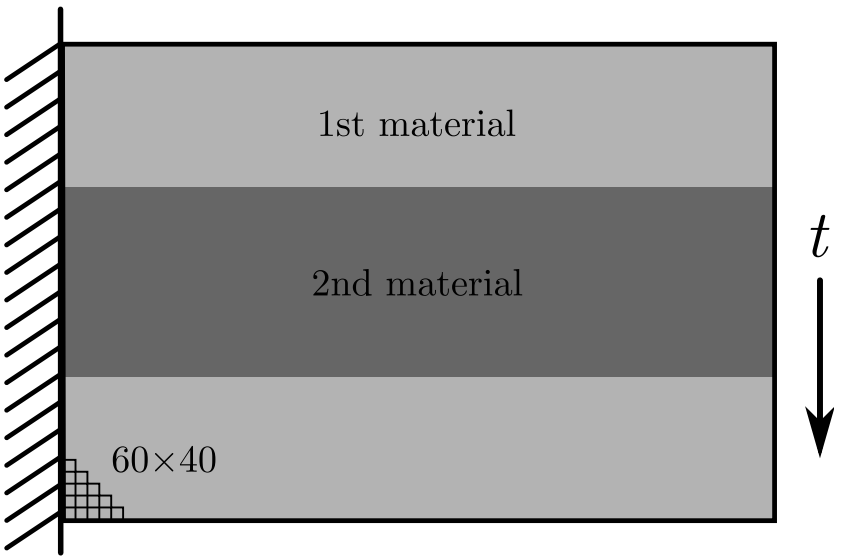

Figure 4.3 Initial distribution for two materials in a short cantilever beam.

The proposed BESO algorithm has been coded using FORTRAN language and linked with the well-known ABAQUS finite element package. The

algorithm uses ABAQUS as an external finite element solver. In each iteration the optimisation algorithm makes an input file and loads it to ABAQUS engine. Upon completion of the finite element analysis the mechanical responses are read from result files that ABAQUS provides.

All the three material interpolation schemes have been included in the optimisation code. The user should provide the optimisation program with an initial ABAQUS input file which models the initial guess design. The optimisation parameters including filtering radius r_f, and move limit m should also be provided. The user can then select any of the three material interpolation schemes proposed. For the case of power-law method, the penalty factor p and the small positive value x_{min} resembling weak material should be provided. Likewise for the alternative interpolation scheme in (4.19), the value of the parameter q is needed by the program.

4.11.1 Comparing material interpolation schemes

Different material interpolation schemes proposed in §4.4, §4.5, and §4.6 are used to solve the SCB problem. For the power-law interpolation, the value of x_{min} is taken as 0.001. The move limit and the filtering radius are chosen as $m = 20$ and $r_f = 2h$ respectively with h denoting the size of the elements.

The results obtained by the power-law interpolation with different values of p are shown in Figure 4.4. It can be seen in Figure 4.4a that using $p = 1$ (linear interpolation) will not result in a recognisable topology. Also the solutions related to $p = 1.1$ and $p = 1.2$ which are illustrated in Figure 4.4b and Figure 4.4c suggest that these values of p are not big enough. The value

of $p = 1.466$ is equivalent to the modified linear interpolation for $\frac{E^{(2)}}{E^{(1)}} = 5$ and it can be seen in Figure 4.4d that the obtained topology is well recognisable. The topology shown in Figure 4.4e corresponds to $p = 3.0$. Although in this case the topology is recognisable, the final value of the objective function is 217.9 which is 1.98% higher than 213.7 resulted from $p = 1.466$.

Apart from the differences, all examples show a smooth evolution of the objective function. The objective function reduces steeply at the beginning and monotonically converges at the end.

The next example involves implementing the alternative interpolation scheme. The results obtained with different values of q are illustrated in Figure 4.5. Like previous example, the move limit and the filtering radius are chosen as $m = 20$ and $r_f = 2h$ respectively. Using the linear interpolation ($q = 0$) will scatter the materials resulting in a non-recognisable topology. Note that Figure 4.5a is slightly different from Figure 4.4a. The reason is the non-zero value of x_{min} in the power-law interpolation. Using $q = 4$ is equivalent to using the modified linear interpolation. One can verify that Figure 4.5d is exactly similar to Figure 4.4d.

The result obtained by the modified linear interpolation is illustrated in Figure 4.6. Again the values of $m = 20$ and $r_f = 2h$ are adopted for the move limit and the filtering radius respectively. It can be seen that this result is exactly similar to the cases of $p = 1.466$ (Fig. 4.4d) and $q = 4.0$ (Fig. 4.5d).

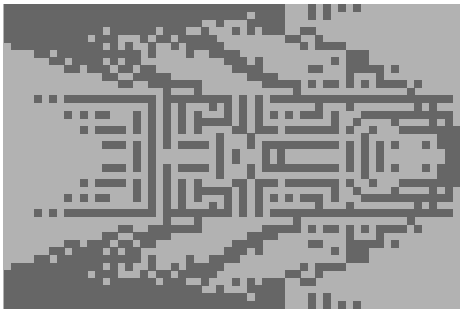

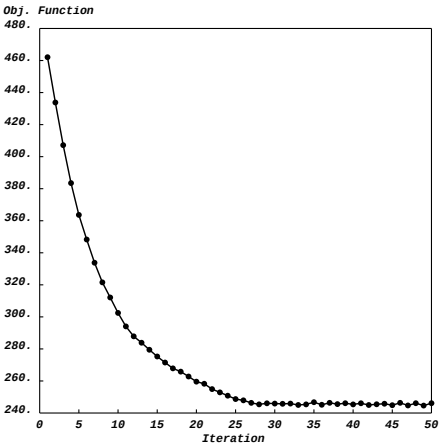

(a) $p = 1.0$

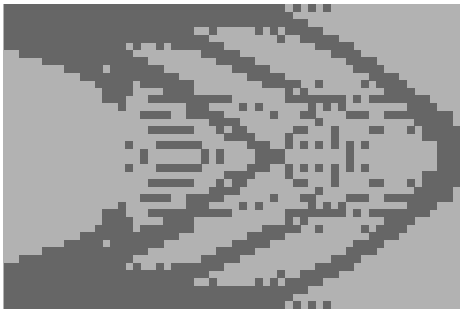

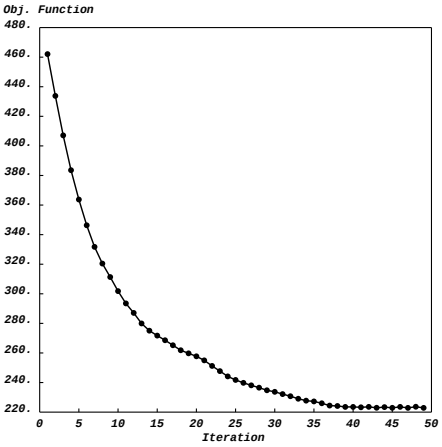

(b) $p = 1.1$

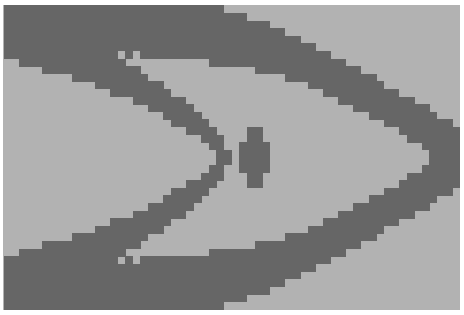

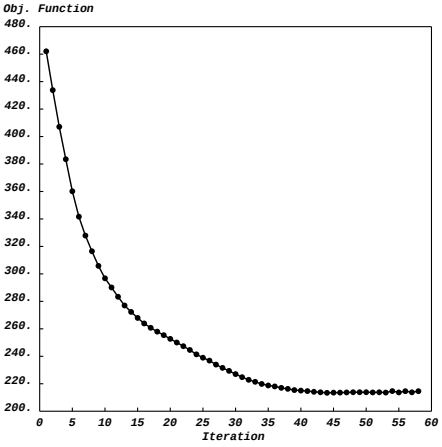

(c) $p = 1.2$

Figure 4.4 The SCB results with power-law interpolation.

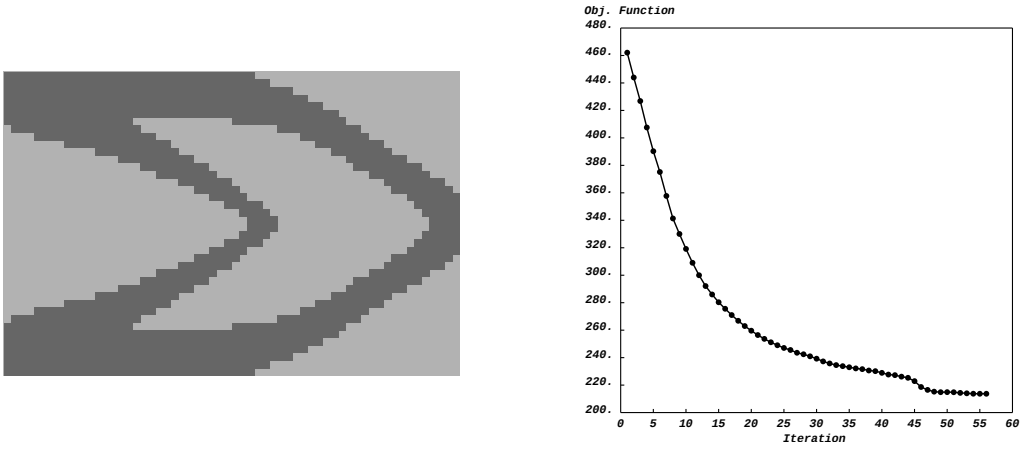

(d) $p = 1.466$

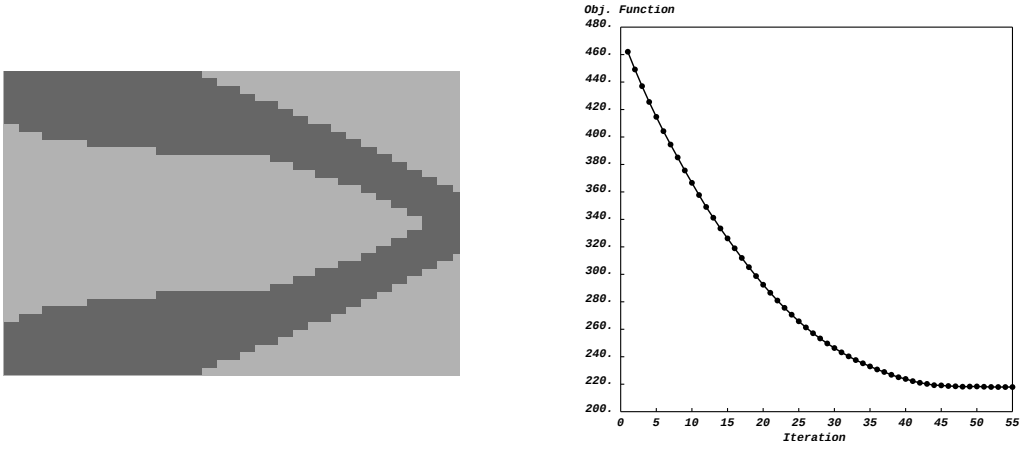

(e) $p = 3.0$

Figure 4.4 The SCB results with power-law interpolation (continued).

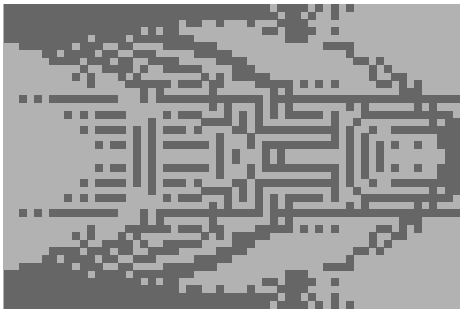

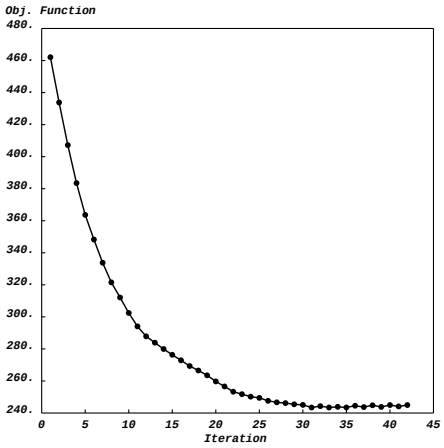

(a) $q = 0.0$

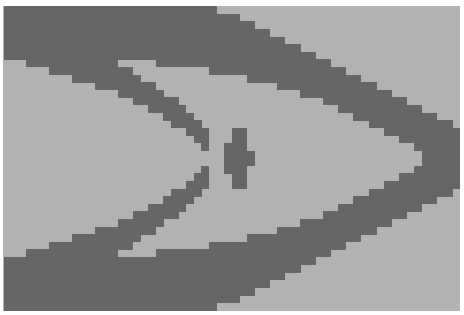

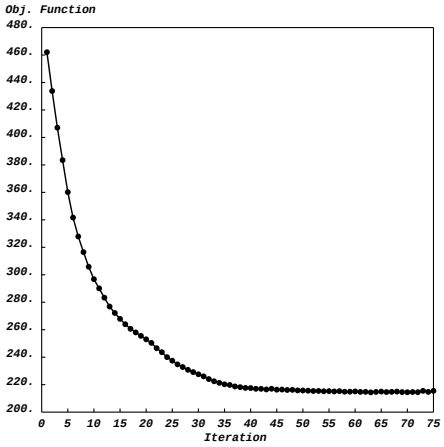

(b) $q = 1.0$

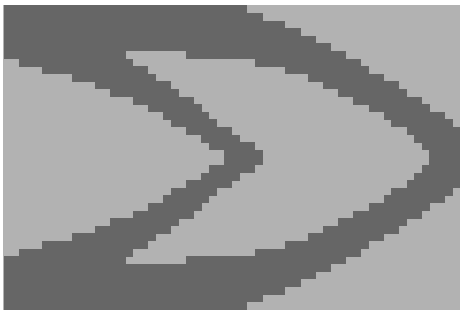

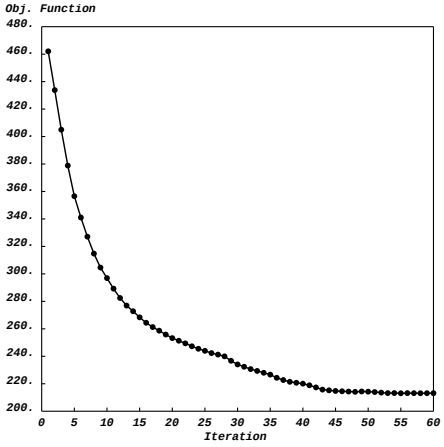

(c) $q = 2.0$

Figure 4.5 The SCB results with alternative interpolation.

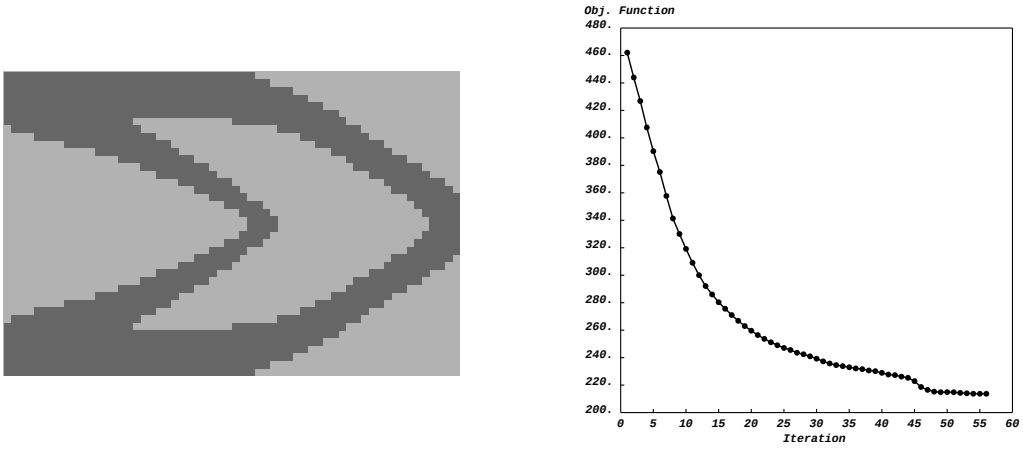

(d) $q = 4.0$

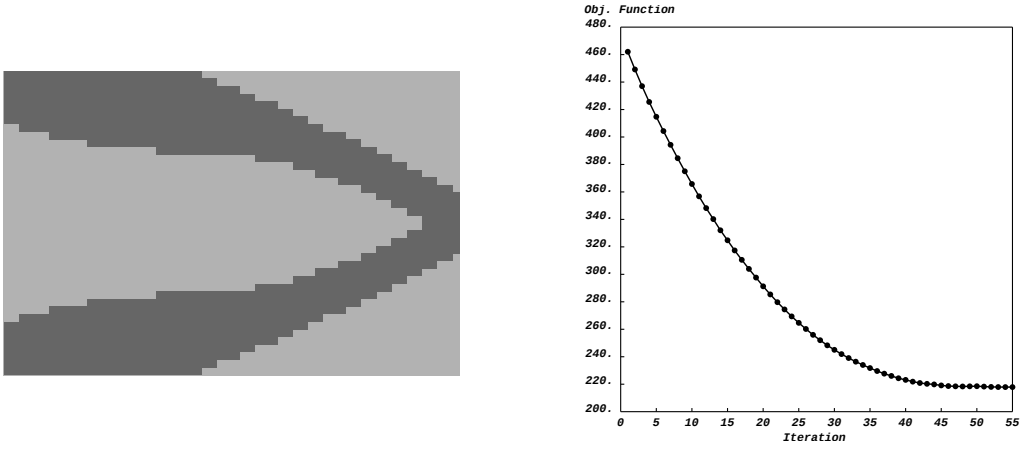

(e) $q = 8.0$

Figure 4.5 The SCB results with alternative interpolation (continued).

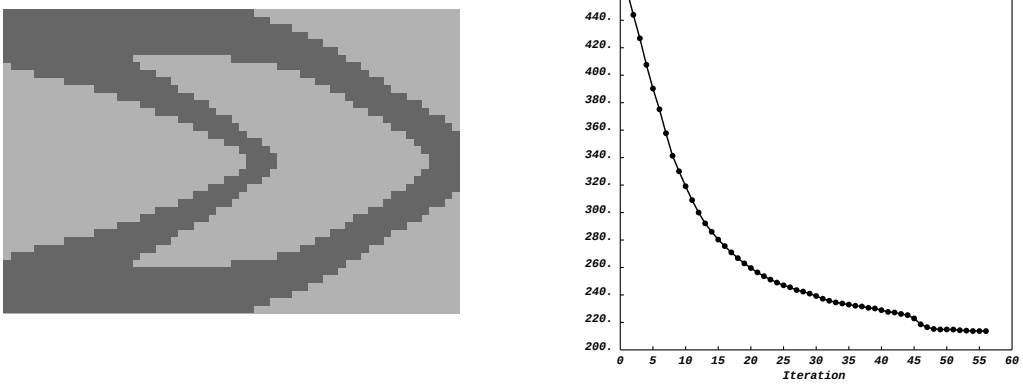

Figure 4.6 The SCB results with modified linear interpolation.

4.11.2 Effect of filtering radius

Using the modified linear material interpolation scheme, the SCB problem is solved using using different filtering radii of $r_f = 0$, $r_f = 2h$, $r_f = 4h$, and $r_f = 6h$. The move limit is $m = 20$. The results are shown in Figure 4.7.

Note the formation of checkerboard patterns when no filtering is in use (Fig. 4.7a). Using bigger filtering radii results in thicker members. It also reduces the complexity of the final topology. The filtering scheme enforces an additional restriction which prevents formation of members thinner than r_f. Hence one can conclude that implementing bigger filtering radii would restrict the feasible space leading to higher values of objective function. This can be confirmed by the obtained results where the final value of the objective function is steadily increasing when the filtering radius is changing from $r_f = 2h$ to $r_f = 6h$ (Table 4.1).

The first case where no filtering was employed resulted in an unexpectedly larger objective function. This is due to using the modified linear material in-

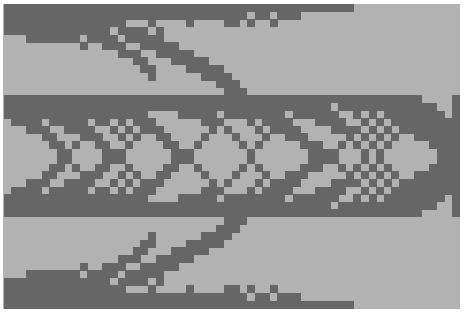

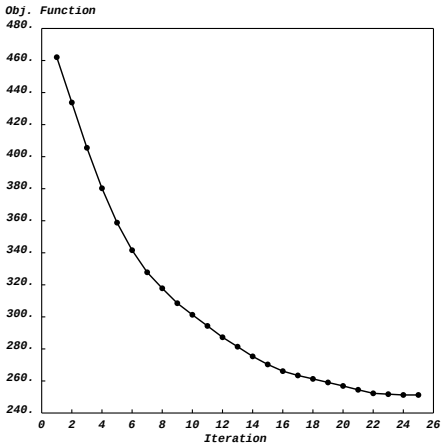

(a) $r_f = 0$ (no filtering)

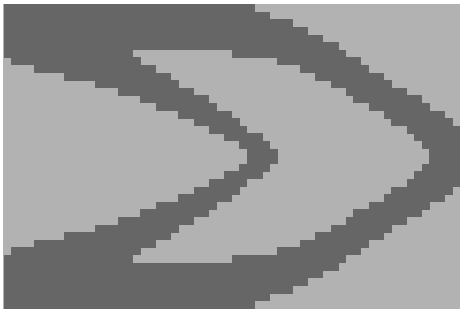

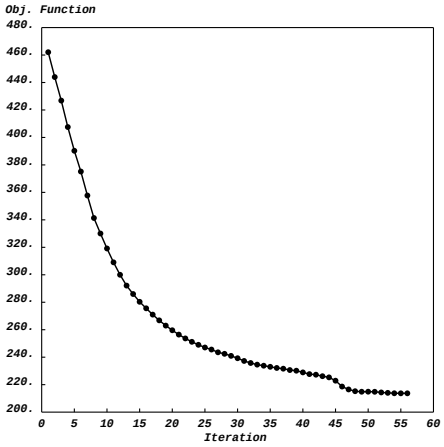

(b) $r_f = 2h$

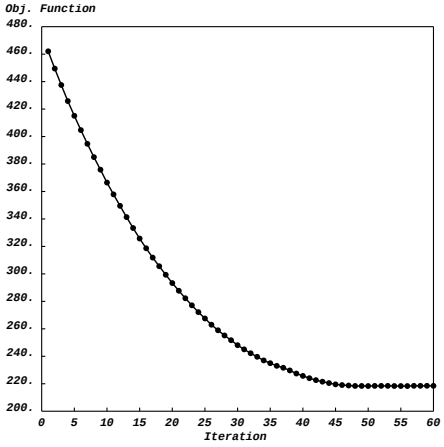

(c) $r_f = 4h$

Figure 4.7 The SCB results for different filtering radii.

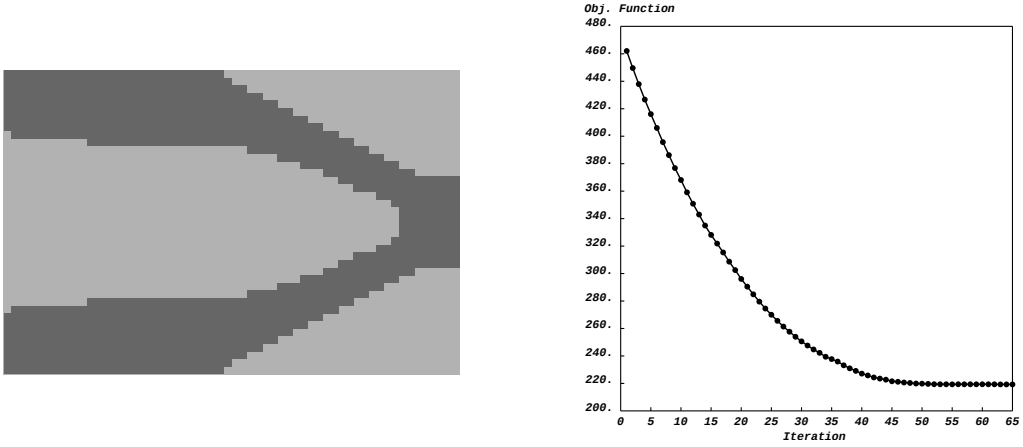

(d) $r_f = 6h$

Figure 4.7 The SCB results for different filtering radii (continued).

Table 4.1 Final values of objective function for different filtering radii.

r_f	0	$2h$	$4h$	$6h$
c	251.272	213.699	218.489	219.279

terpolation which is made to be used with filtering. This interpolation scheme forces the algorithm to terminate faster because of the weighted sensitivity numbers. Using the simple linear interpolation scheme without filtering produces the result shown in Figure 4.8.

The final value of $c = 214.299$ for this case is now comparable to the filtered results reported in Table 4.1. However, as expected, the checkerboard patterns are observable in the final topology.

4.11.3 Effect of move limit

To illustrate the effect of the move limit, different move limits of $m = 10$, $m = 20$, and $m = 40$ are used to solve the SCB problem. The filtering radius

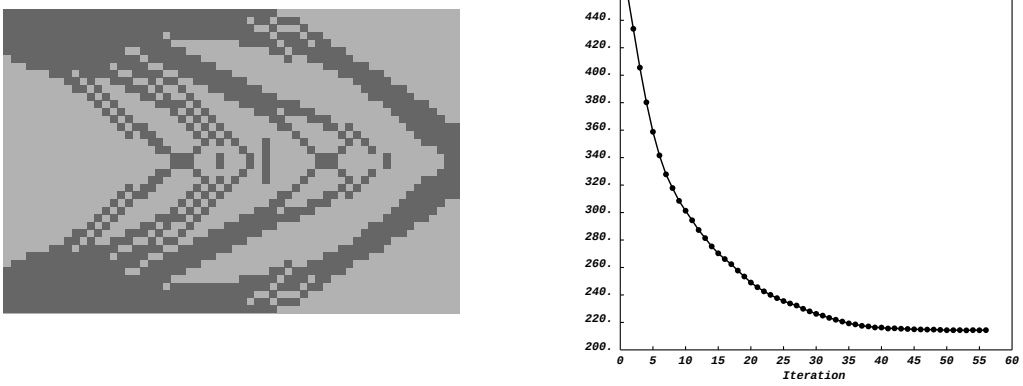

Figure 4.8 The SCB result with linear interpolation and no filtering ($q = 0, r_f = 0$).

is chosen as $r_f = 2h$. The results are illustrated in Figure 4.9.

It can be seen that lower move limits tend to converge slower but to better topologies. The final values of the objective function are reported in Table 4.2.

Table 4.2 Final values of objective function for different move limits.

m	10	20	40	60
c	213.608	213.699	213.491	224.716
Iterations	93	56	59	45

Despite the case of $m = 40$, the final value of the objective function increases with higher move limits. Also, except for the case of $m = 40$, the number of iterations required to solve the problem decreases with higher move limits.

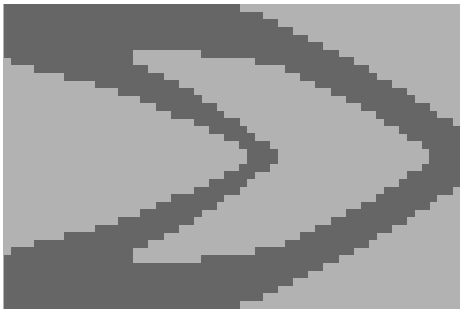

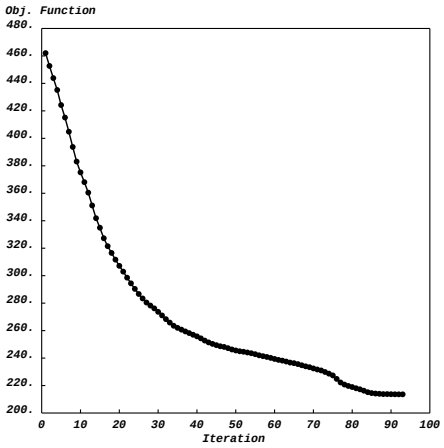

(a) $m = 10$

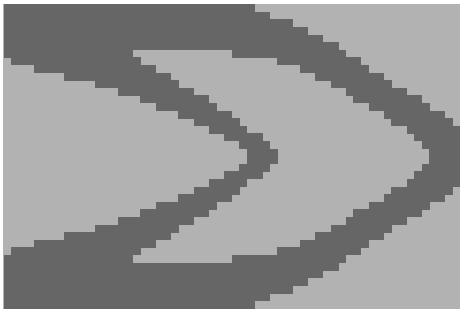

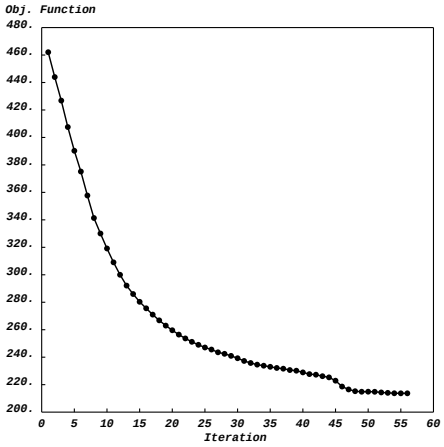

(b) $m = 20$

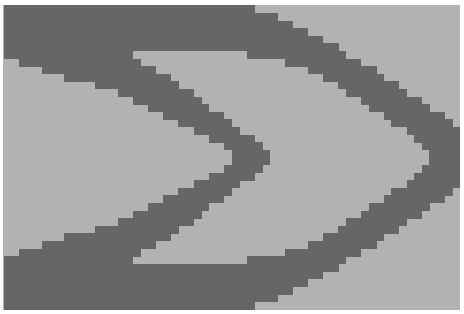

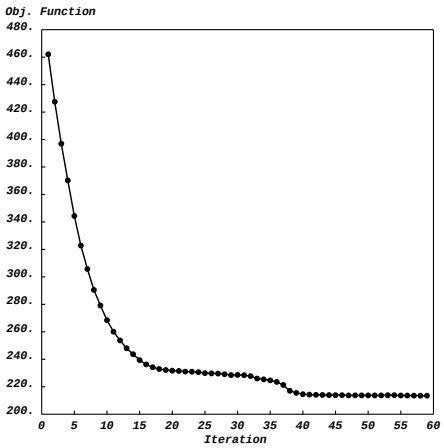

(c) $m = 40$

Figure 4.9 The SCB results for different move limits.

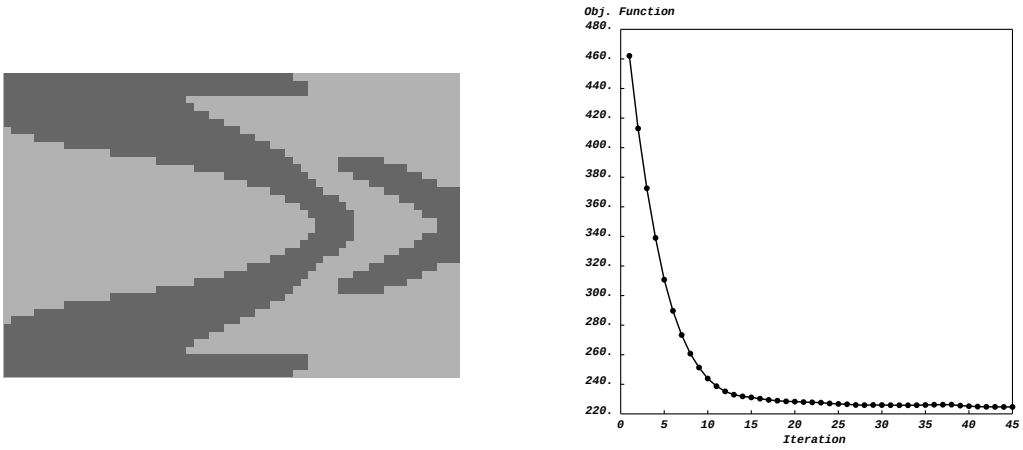

(d) $m = 60$

Figure 4.9 The SCB results for different move limits (continued).

4.12 Concluding remarks

In excavation design finding the shape of the opening and the distribution of the rock reinforcement are two important steps. Both of these problems can be viewed as material distribution problems. The state-of-the-art topology optimisation techniques are known to be capable of handling these sort of problems. However prior to using these optimisation techniques to excavation problems one should tailor them accordingly to match the requirements of these physical problems. This chapter has been devoted to this aim. As the SIMP and the homogenisation methods are not suitable for shape optimisation this chapter has focused on the BESO method.

In reinforcement optimisation one deals with a bi- or multi-material distribution problem. In this case the choice of material interpolation scheme is critically important. Three different material interpolation schemes have been studied in this chapter. The procedure of deriving sensitivity numbers has been discussed and the sensitivity numbers for compliance minimisation

have been formulated. Then the procedure to switch the elements in the proposed BESO has been described.

To optimise the shape of the opening, one needs to find the boundary of the opening and limit the changes to the boundary line. In this chapter, this issue has been covered and the necessary modifications have been discussed.

The mathematical background of the proposed BESO method has been described. It has been demonstrated that the sensitivity numbers in the proposed BESO algorithm are equivalent to the steepest descent vector.

Finally the effect of different material interpolation schemes and different controlling parameters have been studied through some numerical examples. The numerical results show the capability of the proposed method in dealing with two-material problems. Based on the obtained results, the proper material interpolation scheme and the appropriate controlling parameters for a particular problem can be selected. In the next chapter the proposed BESO algorithm will be used to solve both shape and reinforcement optimisation of underground openings.

CHAPTER 5

Optimising tunnels in linear elastic media

5.1 Introduction

Design of support system and selecting an optimum shape for the opening are two important steps in designing excavations in rock masses. Currently selecting the shape and support design are mainly based on designers' judgement and experience. Both of these problems can be viewed as material distribution problems where one needs to find the optimum distribution of a material in a domain. In the previous chapter a new BESO algorithm has been proposed that can be used to solve these kinds of problems.

As discussed in Chapter 3, the linear elastic material models often cannot adequately predict the behaviour of usually non-homogeneous, anisotropic geomaterials. However as a first step, implementing such material model can be instructive. Further, noting that the linear elastic responses are the first order approximation of more general non-linear behaviour, the linear results are useful in verifying empirical designs. This framework can also be useful in designing against time-dependent creep in rock mass where a

quasi-elastic load is imposed on reinforcement (Yin et al. 2000). In this chapter the linear elastic material model is used to model the rock masses for shape optimisation of the opening and topology optimisation of the rock reinforcement in excavation design.

As already mentioned in §3.6, the reinforcement optimisation for tunnels in linear elastic media has been studied by Yin et al. (2000), Yin and Yang (2000a,b), and Liu et al. (2008). Also the shape optimisation of underground excavations has been investigated by Ren et al. (2005) using linear elastic material model. Both of these problems are tackled here using the algorithm proposed in Chapter 4. The obtained results can be verified with these previous studies. To take one further step, both the problems of shape and reinforcement optimisations are solved simultaneously at the end of this chapter.

5.2 Modelling tunnels in linear elastic media

Consider a homogeneous and isotropic rock mass. The homogeneity assumption is valid in case of intact rock and highly weathered rocks. The rock mass behaviour is modelled using a linear elastic material with Young's modulus of E^O and Poisson's ratio of ν^O. It is assumed that the reinforced parts of the rock mass are also homogeneous and isotropic. The homogenised mechanical properties of reinforced rocks are then used for modelling. The reinforced rock is also modelled as a linear elastic material with the elasticity constants of E^R and ν^R. Reinforcing the rock increases its stiffness and thus $E^R > E^O$.

The ratio of $\frac{E^R}{E^O} > 1$ shows the local effectiveness of the reinforcement.

The reinforcement optimisation problem can be viewed as finding the best distribution of the two materials defined by $\{E^O, \nu^O\}$ and $\{E^R, \nu^R\}$. The shape optimisation of the opening, on the other hand, deals with finding the best shape of the boundary between these materials and voids. When the voids are modelled as real voids ($E^V = 0$), their mechanical responses and thus their sensitivities cannot be calculated. In this case, a filtering scheme can be used to extrapolate the sensitivity number of voids. Alternatively one can use a very weak material ($0 < \frac{E^V}{E^O} \ll 1$) to model the void elements. To be consistent with reinforcement optimisation, here the voids in shape optimisation are modelled as a very soft material with elasticity constants of E^V and ν^V.

Now consider a simple design case depicted in Figure 5.1. In this figure, Γ represents the boundary of the opening. The minimum dimensions, shown in the figure, can be due to some design restrictions. In this figure the reinforcement is through rock bolting. The placement, orientation and the length of rock bolts are depicted by solid line segments. The dark shaded area Ω with the outer boundary of $\partial\Omega$ and inner boundary of Γ is the reinforced area of the design. Having found this reinforced area, one can choose the proper location and length of the reinforcing bars and vice versa.

In shape optimisation of the opening one deals with finding Γ, while in reinforcement optimisation, the shape and topology of $\partial\Omega$ and Ω are of interest. The simultaneous shape and reinforcement optimisation can be viewed as finding the optimal Ω when both its inner and outer boundaries, Γ and $\partial\Omega$, being modified. Generally, the economical considerations can dictate

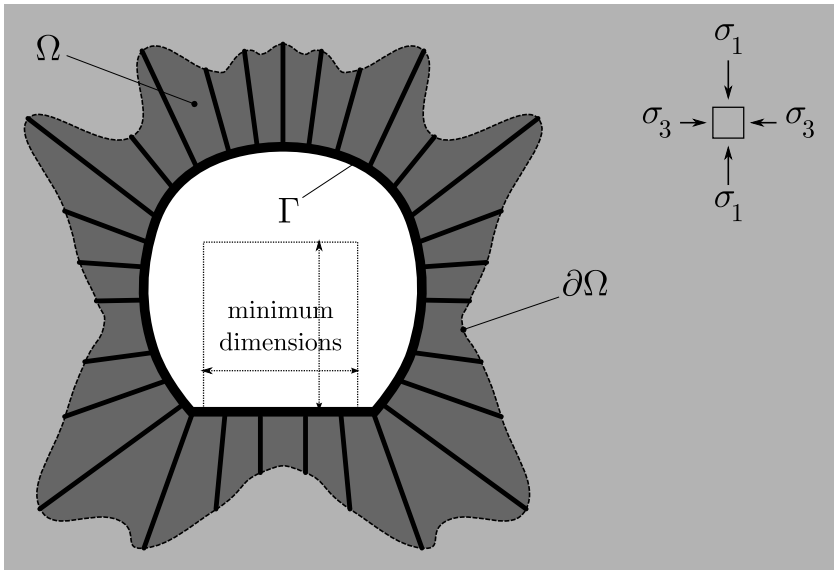

Figure 5.1 A simple design case of an underground tunnel with reinforcement.

an upper bound on the available reinforcement material. This limitation is translated into a constraint on the volume of the reinforced area, Ω.

In what follows, the voids are modelled as a weak material with $\frac{E^V}{E^O} = 0.001$. For simplicity it is assumed that $\nu^O = \nu^R = \nu^V = \nu = 0.3$.

5.3 Shape optimisation of the opening

For the shape optimisation of the tunnel, the mean compliance c is considered as the objective function. The tunnel is assumed with no reinforcement or support. The shape optimisation problem can thus be stated as finding the optimum boundary between the two materials $\{E^O, \nu\}$ and $\{E^V, \nu\}$ to minimise c such that the volume occupied by each material is constant. This

can be expressed as

$$\begin{aligned} &\min_{\mathbf{x}} c(\mathbf{x},\mathbf{u}) = \mathbf{f}^T\mathbf{u} \\ &\text{such that} \mathbf{K}\mathbf{u} = \mathbf{f}, \\ &\qquad x_i \in \{0,1\}, \\ &\qquad V_V = \sum_{i=1}^{n}(1-x_i)V_i = \bar{V}_V \end{aligned} \tag{5.1}$$

where $\bar{V}_V$ is the predefined volume of the opening. The material interpolation scheme formulated in (4.23) is used with $E^{(2)} = E^O$ and $E^{(1)} = E^V$. Consequently the sensitivity numbers are calculated from (4.23).

Shape optimisation of three different tunnel designs are considered here. The first problem involves a tunnel under biaxial in-situ stresses. In the second example the tunnel is restricted to have a flat floor with traffic load applied on it. The third example involves the shape optimisation of two identical parallel tunnels. In these problems the infinite rock domain is replaced by a large finite domain of 100×100 equal square shaped 4-node elements.

5.3.1 Tunnel under biaxial stresses

The initial guess design is depicted in Figure 5.2. The size of the opening is 1.98% of the domain size. Because of symmetry only half of the domain is used for analysis which is discretised into 50×100 elements.

Because in shape optimisation only boundary elements are allowed to change, the move limit is restricted to $m = 1$. The filtering radius is assumed to be equal to 2.5 times the elements' size. The vertical stress σ_1 is assumed

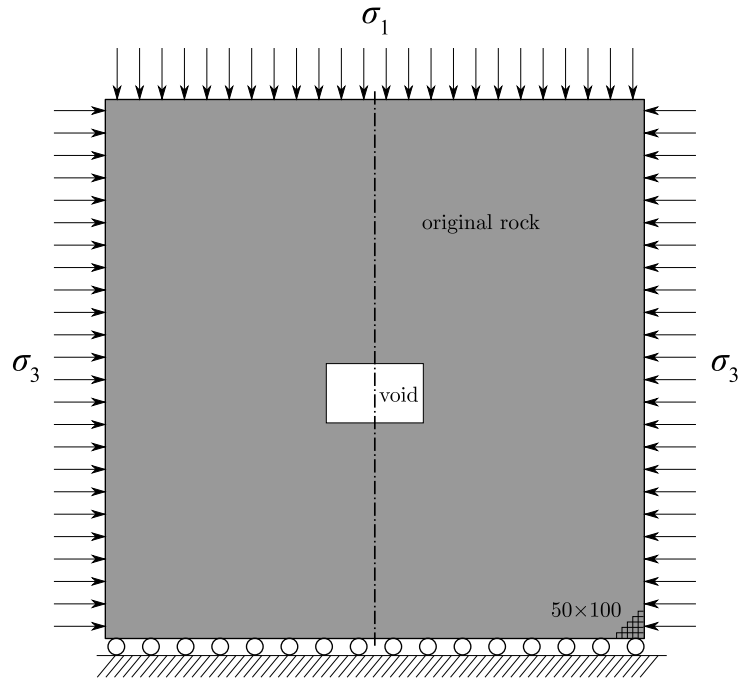

Figure 5.2 Initial guess design for tunnel under biaxial stresses.

to be equal to $0.1E^O$.

The optimal shapes are obtained for three different ratios of horizontal to vertical stresses: $\sigma_3 = 0.4\sigma_1$, $\sigma_3 = 0.7\sigma_1$, and $\sigma_3 = \sigma_1$. The results are depicted in Figure 5.3.

The resulted shapes are nearly elliptical with aspect ratios similar to the ratio of the in-situ stresses. This conclusion is similar to the results obtained by Ren et al. (2005). The slight differences from perfect ellipses in cases of $\frac{\sigma_3}{\sigma_1} = 0.7$ (Fig. 5.3b) and $\frac{\sigma_3}{\sigma_1} = 1.0$ (Fig. 5.3c) are due to the volume constraint.

It can be seen that the evolution of the objective function is not very smooth. This is due to the restrictions applied for shape optimisation. However the steady drops in the objective function values and the final shapes verify this approach.

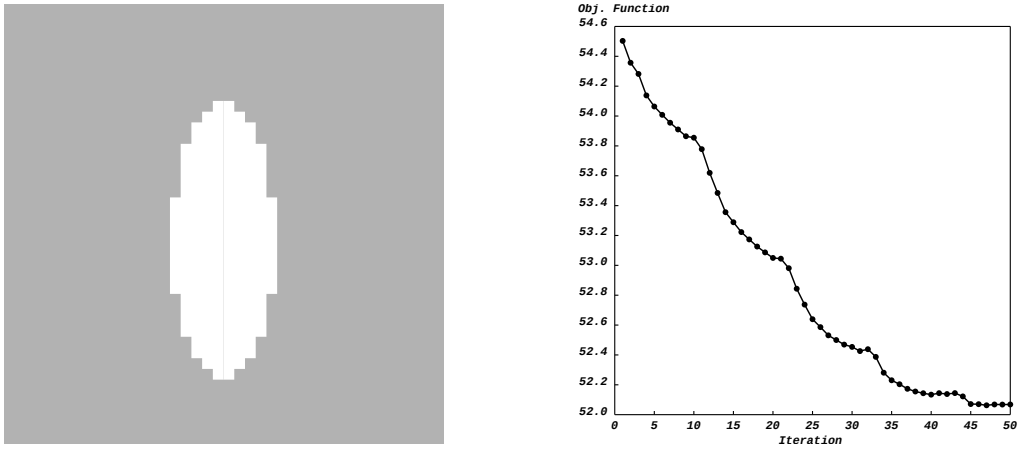

(a) $\sigma_3 = 0.4\sigma_1$

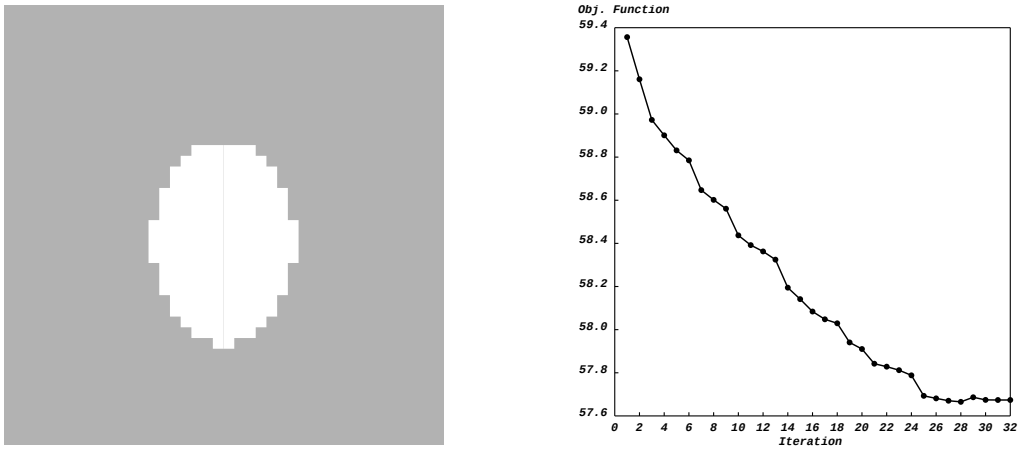

(b) $\sigma_3 = 0.7\sigma_1$

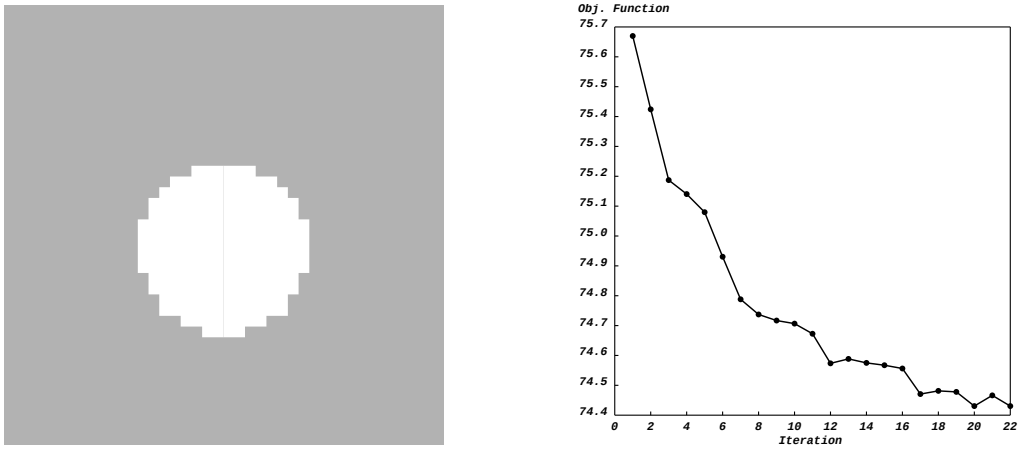

(c) $\sigma_3 = \sigma_1$

Figure 5.3 Optimum shapes for tunnels under biaxial stress.

5.3.2 Smoothing the shapes

To obtain smoother shapes one can use a finer mesh. However finite element analysis of finer mesh will take longer time. Particularly, in the optimisation process, several finite element analyses are required to solve a single problem which can effectively prolongs the solution procedure.

Alternatively one can use the same coarse mesh and smoothen the final results through a smoothing post-processor. A smoothing procedure based on Bézier curves is applied in this thesis.

After obtaining the final shapes, the boundary of the opening is extracted. This boundary is defined in (4.28) as $\mathcal{B}_h$. The boundary is then smoothed using Bézier curves. The Bézier curve for a set of control nodes always pass the first and the last node and lies in the convex hull of the control nodes. Some examples of Bézier curves are depicted in Figure 5.4.

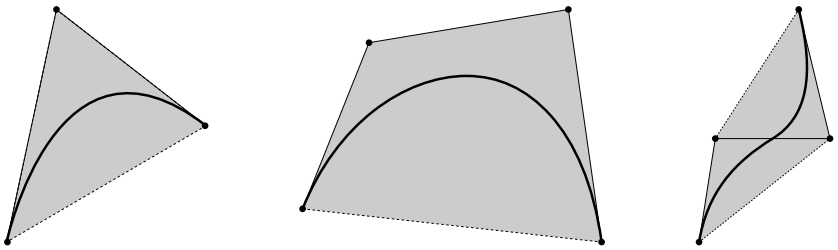

Figure 5.4 Some examples of Bézier curves. The shaded areas represent the convex hull formed by control points

The properties of Bézier curves make them suitable for smoothing jagged boundary lines. However for many control points with varying coordinates, the Bézier curve might be too distanced from the original boundary line. In this case the area of the smoothed tunnel may become far smaller than the predefined value. To prevent this, before smoothing, the boundary line

$\mathcal{B}_h$ is divided into some segments, such that in each segment, the vertical coordinates of the points change monotonically. Then the Bézier curve for each segment is derived. The complete smoothed shape is achieved by joining all the smoothed segments.

Suppose a boundary segment consists of n nodes $\mathrm{P}_1, \mathrm{P}_2, \ldots, \mathrm{P}_n$ where $\mathrm{P} = (P_x, P_y, (P_z))$. For this boundary segment, the Bézier curve of degree n should be used which takes the following form

$$\mathrm{B}(t) = \sum_{i=0}^{n} \binom{n}{i} (1-t)^{n-i} t^i \mathrm{P}_i, \quad t \in [0,1], \quad \{\mathrm{P}_1, \mathrm{P}_2, \ldots, \mathrm{P}_n\} \subset \mathcal{B}_h \tag{5.2}$$

The coordinates of n smoothed nodes can be calculated by setting the parameter t equal to n values equally dividing the $[0,1]$ interval. Hence the smoothed boundary segment can be expressed as

$$\mathcal{B}_s = \left\{ \mathrm{B}(t) \,\middle|\, t = \tfrac{i-1}{n-1}, i = 1, \ldots, n \right\} \tag{5.3}$$

Finally the location of smoothed nodes are used to produce a new mesh. This procedure is depicted in Figure 5.5.

Using this smoothing post-processor the optimum shapes reported in Figure 5.3 are smoothed. The results are illustrated in Figure 5.6.

The optimum shape of a hole under biaxial stress is known to be an ellipse with an aspect ratio (the ratio of major and minor axes) matching the stress ratio (Cherepanov 1974; Pedersen 2000; Hoek and Brown 1980). Fixing the area of the hole to A, the semimajor and semiminor axes (a and

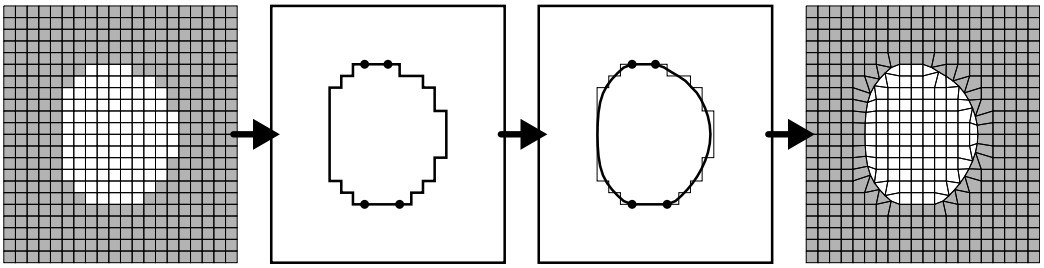

Figure 5.5 Smoothing boundary lines with Bézier curves: a) The final optimum shape is loaded into the post-processor, b) The boundary line is extracted and divided into segments, c) The Bézier curves for these segments is calculated, and d) The smoothed mesh is reported.

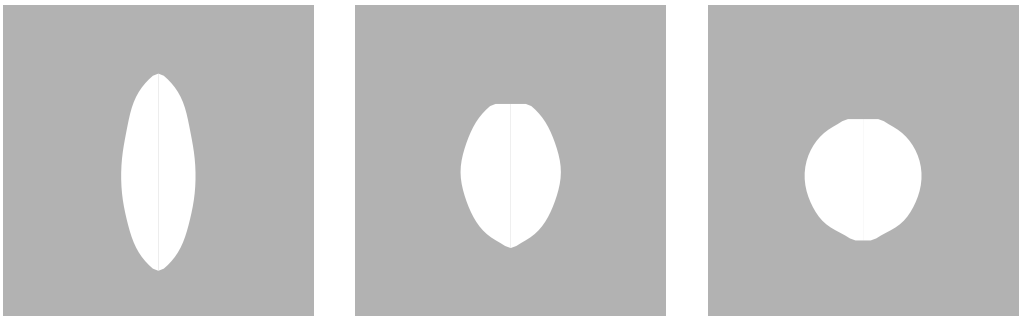

(a) $\sigma_3 = 0.4\sigma_1$ (b) $\sigma_3 = 0.7\sigma_1$ (c) $\sigma_3 = \sigma_1$

Figure 5.6 Smoothed shapes for tunnels under biaxial stress.

b respectively) of the optimum ellipse can be found as

$$a = \sqrt{\frac{A}{\lambda\pi}}, \quad b = \sqrt{\frac{\lambda A}{\pi}} \tag{5.4}$$

where $\lambda = \frac{\sigma_3}{\sigma_1}$ is the stress ratio. For the stress ratios used in the solved example, the values of the major and minor axes of the optimum ellipse and the obtained shapes are compared in Table 5.1. As reported in this table, the numerical results are close to the analytical solutions.

Table 5.1 Comparing the size of major and minor axes of numerical and analytical solutions for the example of tunnel under biaxial stresses.

	Analytical results		Numerical results		
λ	minor axis ($2b$)	major axis ($2a$)	minor axis	major axis	aspect ratio
0.4	2.008	5.021	1.957	5.191	0.377
0.7	2.657	3.795	2.641	3.794	0.696
1.0	3.176	3.176	3.075	3.195	0.963

The optimum ellipses are compared to the obtained results in Figure 5.7. It can be seen that the numerical results match well with analytical solutions.

5.3.3 Obtaining a flat floor

In many cases it is required that tunnels have flat floors. The optimum shape of such tunnels can be achieved by setting a group of non-designable rock elements underneath the tunnel's floor. Moreover, serviceability and other design requirements may impose some restrictions on the dimensions of the tunnel. These restrictions can also be included by setting some non-designable elements. To illustrate these kind of problems, a tunnel under

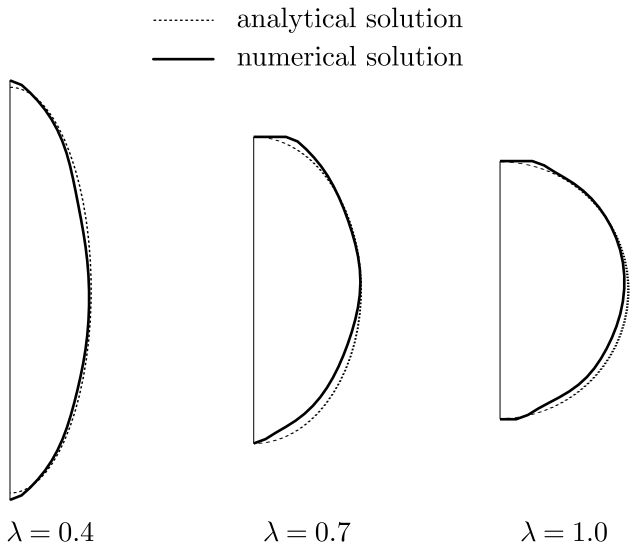

Figure 5.7 Comparing the numerical and the analytical results for tunnels under biaxial stresses.

biaxial stresses is considered which needs to have a flat floor and a minimum size. The initial design is illustrated in Figure 5.9

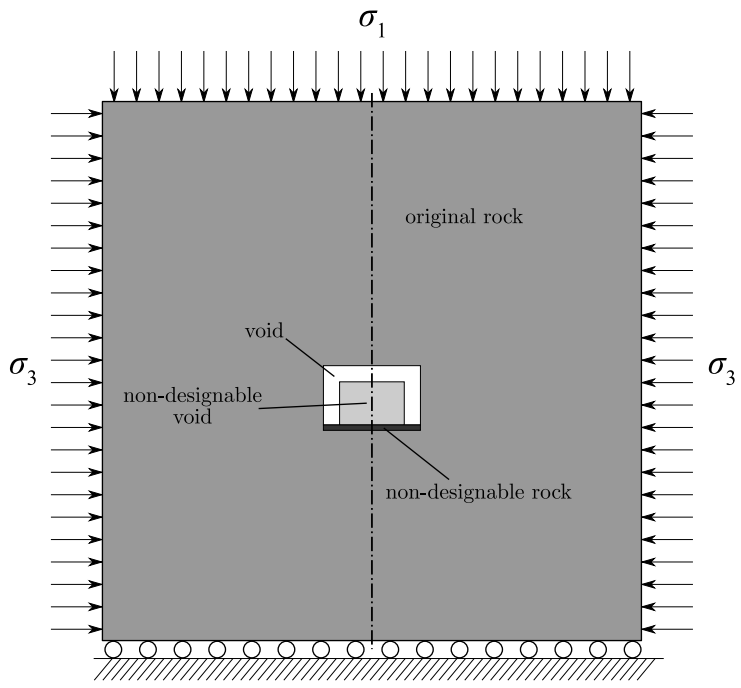

Figure 5.8 Initial design for a tunnel under biaxial stresses with a flat floor.

The minimum size of the tunnel is restricted to 12×8 elements by setting an area of non-designable voids. The optimum shapes for different values of $\frac{\sigma_3}{\sigma_1}$ are found and smoothed by Bézier curves. The results are reported in Figure 5.9.

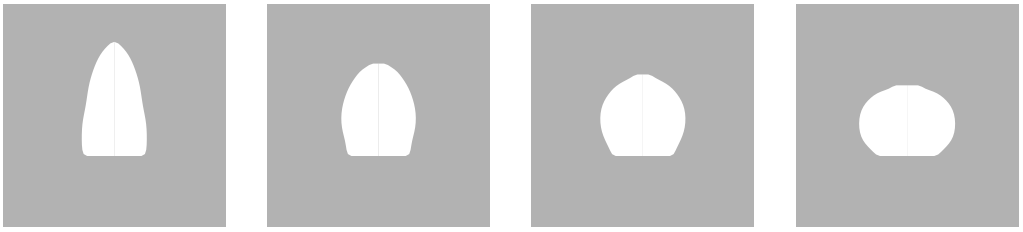

(a) $\sigma_3 = 0.4\sigma_1$ (b) $\sigma_3 = 0.7\sigma_1$ (c) $\sigma_3 = 1.0\sigma_1$ (d) $\sigma_3 = 1.3\sigma_1$

Figure 5.9 Optimum shapes for flat-floored tunnels under biaxial stress.

The optimum shapes all satisfy the imposed restrictions. It is observable that the aspect ratio of the optimal shape depends on the stress ratio. As the ratio of the horizontal to the vertical stress increases, the optimum shape becomes shorter and wider.

5.3.4 Adding traffic load

The previous flat-floored tunnel example is considered with a traffic load acting on the tunnel's floor. The intensity of this traffic load is assumed as $\sigma_{tr} = 0.25\sigma_1$. The obtained results are reported in Figure 5.10.

Note the differences between optimum shapes with and without traffic load. Adding the (vertical) traffic load slightly decreases the height and increases the width of the optimal tunnel shapes. Also in the tunnels reported in Figure 5.10, the sides have higher curvatures and the crowns have lower

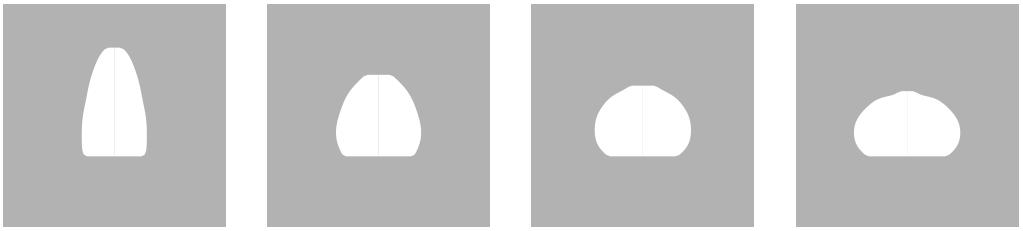

(a) $\sigma_3 = 0.4\sigma_1$ (b) $\sigma_3 = 0.7\sigma_1$ (c) $\sigma_3 = 1.0\sigma_1$ (d) $\sigma_3 = 1.3\sigma_1$

Figure 5.10 Optimum shapes for tunnels under biaxial stress and traffic load.

curvatures comparing to the shapes reported in Figure 5.9.

5.3.5 Two parallel tunnels

Shape optimisation of two parallel tunnels with flat floors, with and without traffic load is solved here as the last example. The initial design is depicted in Figure 5.11.

For a single tunnel, the area of the opening and its minimum size are restricted to 100 elements and 6×7 elements respectively. The final topologies without and with traffic load are illustrated in Figure 5.12 and Figure 5.13 respectively.

Like all previous examples the aspect ratio of the final optimal shapes depends on the in-situ stress ratio. It is interesting to note that the closer sides of the optimal tunnel pairs are less curved than their outer sides. The differences in the optimal shapes with and without traffic load which were observed between Figure 5.10 and Figure 5.9 can also be observed by comparing Figure 5.12 and Figure 5.13.

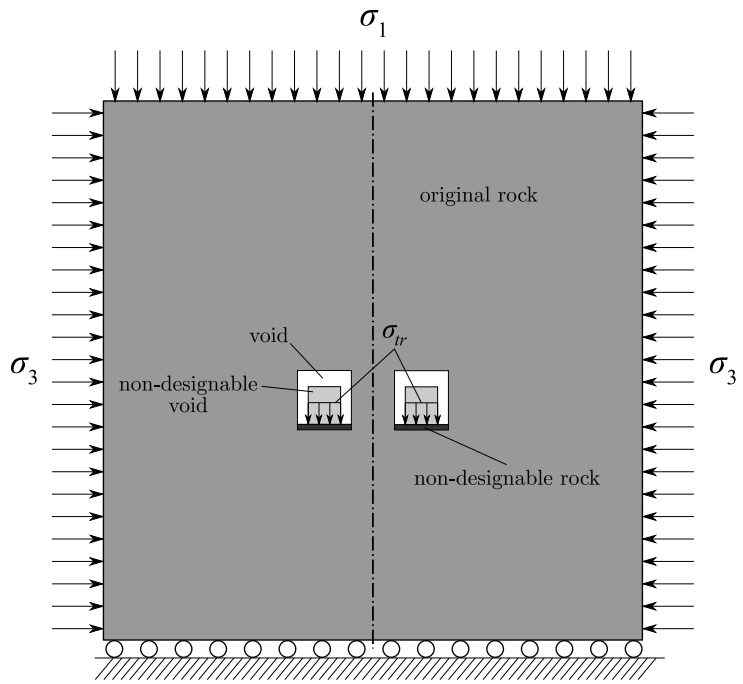

Figure 5.11 Initial design for two tunnels under biaxial stresses.

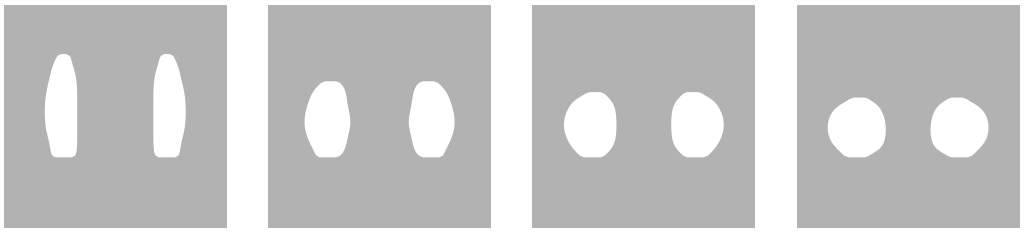

(a) $\sigma_3 = 0.4\sigma_1$ (b) $\sigma_3 = 0.7\sigma_1$ (c) $\sigma_3 = 1.0\sigma_1$ (d) $\sigma_3 = 1.3\sigma_1$

Figure 5.12 Optimum shapes for two tunnels under biaxial stress.

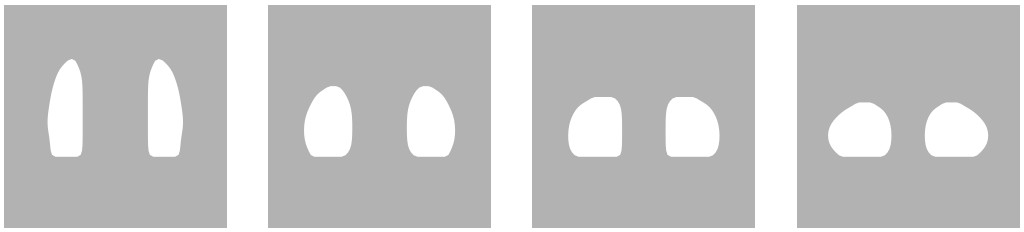

(a) $\sigma_3 = 0.4\sigma_1$ (b) $\sigma_3 = 0.7\sigma_1$ (c) $\sigma_3 = 1.0\sigma_1$ (d) $\sigma_3 = 1.3\sigma_1$

Figure 5.13 Optimum shapes for two tunnels under biaxial stress and traffic load.

5.4 Reinforcement optimisation for tunnels

Reinforcement optimisation of tunnels in linear elastic media was solved for different objective functions by Yin et al. (2000), Yin and Yang (2000a,b), and Liu et al. (2008). Here we implement the proposed BESO approach to solve this problem for a number of objective functions. The BESO technique to be used here is different from the one used by Liu et al. (2008) mainly in that a filtering scheme is used instead of fixed grid finite element to overcome the numerical instabilities. The proposed approach is much easier to implement and faster to calculate.

A tunnel under biaxial stresses is considered here for reinforcement optimisation. The design domain and initial distribution of reinforcement are depicted in Figure 5.14.

A layer of elements surrounding the opening are fixed to reinforced rock. This represents a shotcrete layer with similar mechanical properties to reinforced rock. The volume of reinforced area is fixed to 3.7% of the domain size. The ratio of moduli of elasticity of the reinforced and the original rock is considered as $\frac{E^R}{E^O} = \frac{10}{3}$.

Because of symmetry only half of the domain is modelled for finite element analysis. The filtering radius is chosen as $r_f = 2.5h$ with h denoting the element size. The move limit is selected as $m = 40$ elements which is equivalent to 0.8% of the domain size. The modified linear interpolation (4.23) is used for material interpolation.

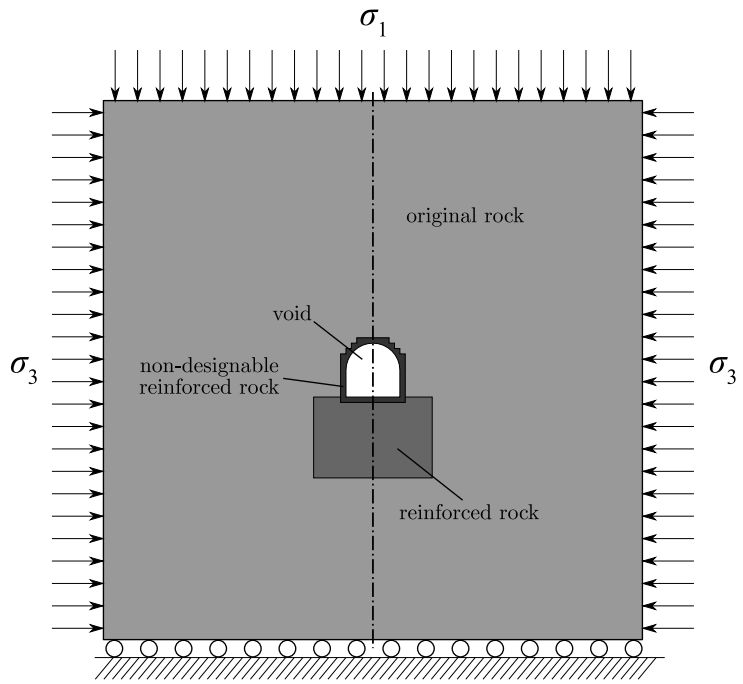

Figure 5.14 Initial reinforcement distribution of a tunnel under biaxial stresses.

5.4.1 Minimum compliance design

Using the mean compliance as the objective function the optimisation problem can be stated as

$$\begin{aligned} \min_{x_1,x_2,\ldots,x_n} \quad & c = \mathbf{f}^T\mathbf{u} \\ \text{such that} \quad & \mathbf{K}\mathbf{u} = \mathbf{f}, \\ & V_R = \sum_{i=1}^{n} x_i V_i = \bar{V}_R, \\ & x_i \in \{0,1\} \end{aligned} \tag{5.5}$$

where V_i is the volume of the i-th element and $\bar{V}_R$ is the prescribed reinforcement volume. The value of zero for design variables indicate original rock

material and $x_i = 1$ shows that the i-th element is reinforced. The number of total designable elements is denoted by n.

The optimum reinforcement distribution corresponding to minimum compliance for different stress ratios are shown in Figure 5.15.

The evolution of objective function shows a smooth and monotonic trend specially for the first three cases (Fig. 5.15a-c). The reinforcement distribution changes from vertically aligned for the case of $\frac{\sigma_3}{\sigma_1} = 0.4$ to horizontally aligned shapes for $\frac{\sigma_3}{\sigma_1} = 1.3$. It can be seen that the minimum compliance reinforcement design highly depends on the in-site stress ratio.

5.4.2 Minimising floor heaves

One of common objectives in tunnel design is minimising floor heaves. To obtain such designs we define the following objective function

$$h = \frac{2u_c - u_r - u_l}{2} \tag{5.6}$$

where u_c, u_l, and u_r are the vertical displacement of the centre, the left corner and the right corner of the tunnel floor. Unlike the mean compliance, floor heave is a local objective.

In order to calculate the sensitivities of the floor heave a new load case is introduced with an upward unit load at the centre of the floor and two downward half unit loads at the right and the left floor corners. This load case is illustrated in Figure 5.16.

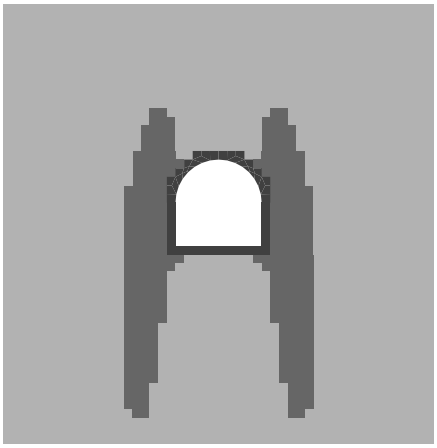

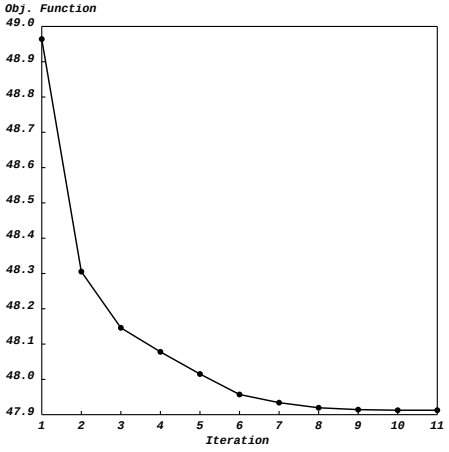

(a) $\sigma_3 = 0.4\sigma_1$

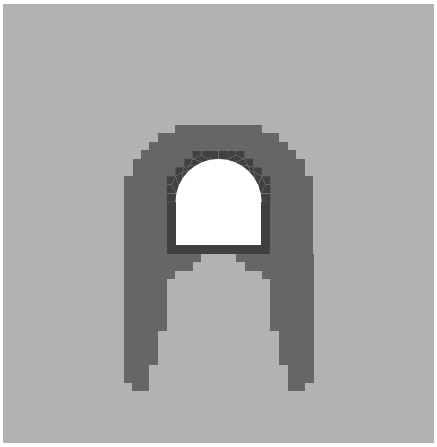

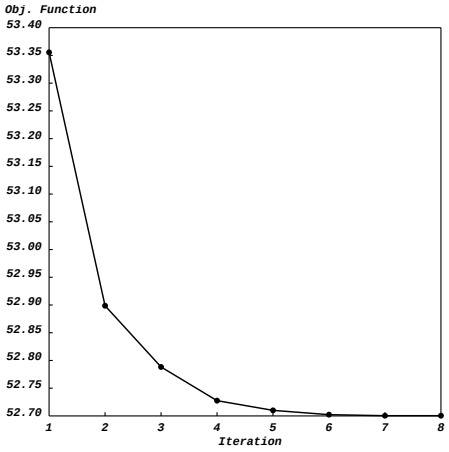

(b) $\sigma_3 = 0.7\sigma_1$

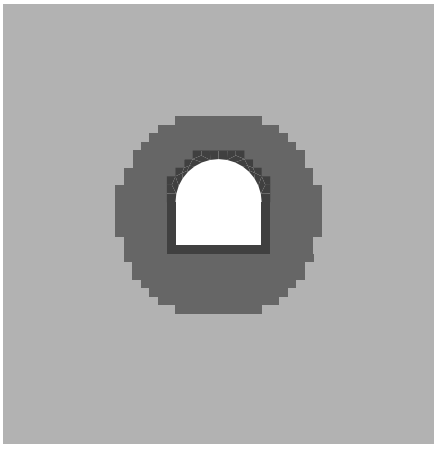

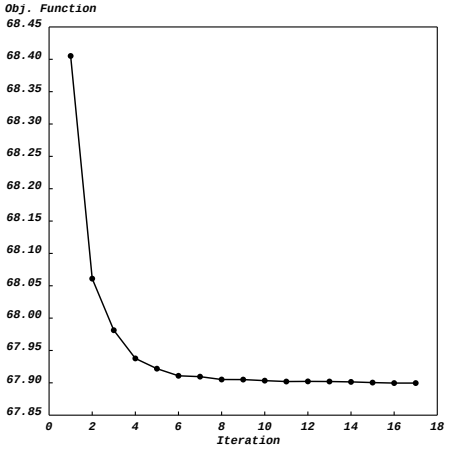

(c) $\sigma_3 = \sigma_1$

Figure 5.15 Optimum reinforcement for minimising compliance.

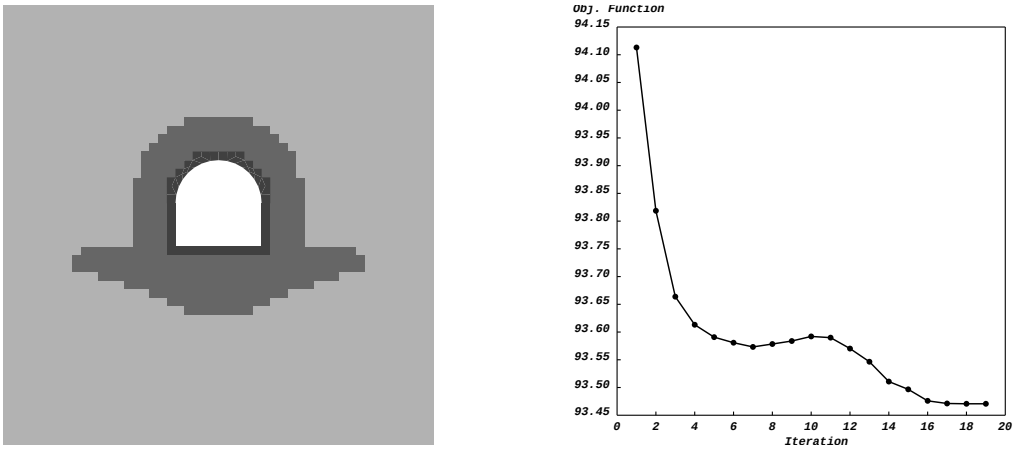

(d) $\sigma_3 = 1.3\sigma_1$

Figure 5.15 Optimum reinforcement for minimising compliance (continued).

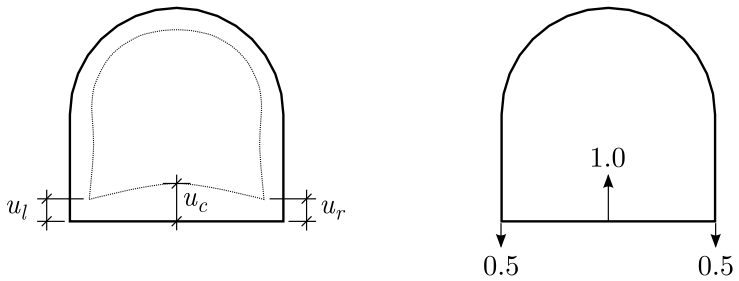

Figure 5.16 The new load case to evaluate floor heaves.

The floor heave, h, can then be expressed as

$$h = \tilde{\mathbf{f}}^T \mathbf{u} \tag{5.7}$$

where $\tilde{\mathbf{f}}$ and $\tilde{\mathbf{u}}$ are the nodal force and displacement vectors associated with the new load case. The minimisation problem can then be expressed as

$$\begin{aligned} \min_{x_1,x_2,\ldots,x_n} \quad & h = \tilde{\mathbf{f}}^T \mathbf{u} \\ \text{such that} \quad & \mathbf{K}\mathbf{u} = \mathbf{f}, \\ & \mathbf{K}\tilde{\mathbf{u}} = \tilde{\mathbf{f}}, \\ & V_R = \sum_{i=1}^{n} x_i V_i = \bar{V}_R, \\ & x_i \in \{0, 1\} \end{aligned} \tag{5.8}$$

As the system is linear elastic, the stiffness matrix $\mathbf{K}$ is constant and does not depend on the load case.

Like the case of mean compliance, sensitivity analysis for floor heave can be achieved through the adjoint method or direct differentiation. The former approach has been used in §2.3.2 for sensitivity analysis of the mean compliance. To illustrate the latter approach, here we derive the sensitivities of floor heave by direct differentiation.

Differentiating (5.7) and noting that the force vector is constant, one can write

$$\frac{\partial h}{\partial x_i} = \tilde{\mathbf{f}}^T \frac{\partial \mathbf{u}}{\partial x_i} \tag{5.9}$$

Now differentiating the original equilibrium equation $\mathbf{K}\mathbf{u} = \mathbf{f}$, and again

noting the constant force vector, the following equation can be achieved

$$\frac{\partial \mathbf{K}}{\partial x_i}\mathbf{u} + \mathbf{K}\frac{\partial \mathbf{u}}{\partial x_i} = \mathbf{0} \tag{5.10}$$

which can be solved for $\frac{\partial \mathbf{u}}{\partial x_i}$ to yield

$$\frac{\partial \mathbf{u}}{\partial x_i} = -\mathbf{K}^{-1}\frac{\partial \mathbf{K}}{\partial x_i}\mathbf{u} \tag{5.11}$$

Substituting (5.11) in (5.9), the latter can be rewritten as

$$\frac{\partial h}{\partial x_i} = -\tilde{\mathbf{f}}^T\mathbf{K}^{-1}\frac{\partial \mathbf{K}}{\partial x_i}\mathbf{u} \tag{5.12}$$

which can be simplified to yield the following sensitivities

$$\frac{\partial h}{\partial x_i} = -\tilde{\mathbf{u}}_i{}^T\frac{\partial \mathbf{K}_i}{\partial x_i}\mathbf{u}_i \tag{5.13}$$

Here the subscript i indicates the element level values associated with the i-th element. Note that unlike mean compliance sensitivities (2.14), the above sensitivities are not necessarily always negative. However unlike what Liu et al. (2008) have stated, this issue will not cause any problem for the BESO algorithm.

Having the gradient vector calculated, the sensitivity numbers for BESO can be easily evaluated by following the procedures introduced in Chapter 4. Particularly, the sensitivity numbers for floor heave can be achieved by substituting $\mathbf{u}_i^T\mathbf{K}_i\mathbf{u}_i$ in compliance sensitivity numbers with $\tilde{\mathbf{u}}_i{}^T\mathbf{K}_i\mathbf{u}_i$.

Using the sensitivity analysis results, the problem (5.8) is solved to find

the optimum distribution of reinforcement minimising the floor heave. The results are reported in Figure 5.17.

A good consistency can be found between the results in Figure 5.17 and the topologies reported by Liu et al. (2008). As expected, most of the reinforced materials are distributed underneath the tunnel. It can be seen that the minimum floor heave designs are highly dependent on in-situ stress ratios.

5.4.3 Minimising tunnel convergence

As another objective, the decrement of the tunnel volume due to stress release after excavation is considered. This objective can be formulated as

$$v = \sum_{j \in \mathcal{B}_h} \mathbf{n}_j \cdot \mathbf{u}_j \tag{5.14}$$

where $\mathbf{n}_j$ denotes the normal (inward) vector of the opening boundary at node j. Similar to floor heave, the tunnel convergence can also be evaluated using an auxiliary load case. This load case consists of an inward distributed pressure load on the opening boundary. An illustration is given in Figure 5.18.

Denoting the related nodal force vector by $\tilde{\mathbf{f}}$ and the resulted nodal displacements by $\tilde{\mathbf{u}}$, the tunnel convergence can be rewritten as

$$v = \tilde{\mathbf{f}}^T \mathbf{u} \tag{5.15}$$

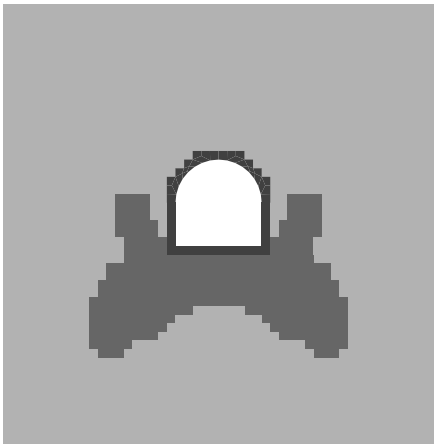

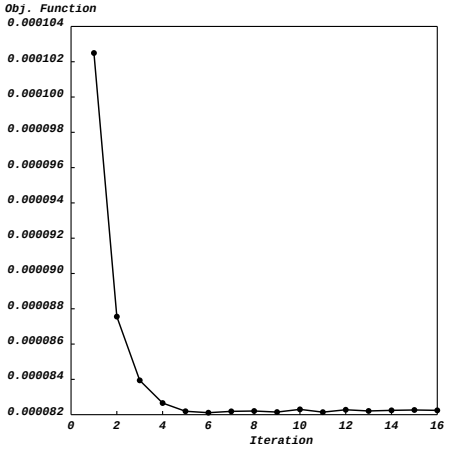

(a) $\sigma_3 = 0.4\sigma_1$

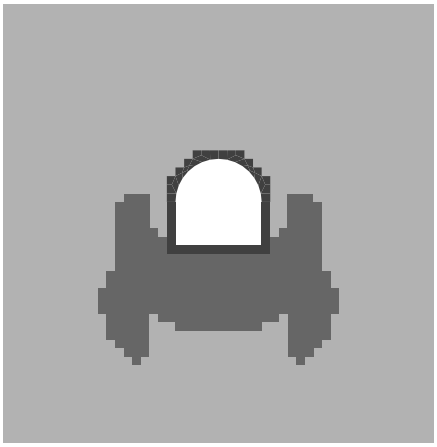

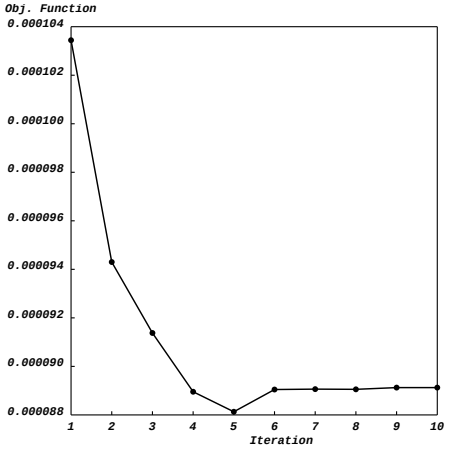

(b) $\sigma_3 = 0.7\sigma_1$

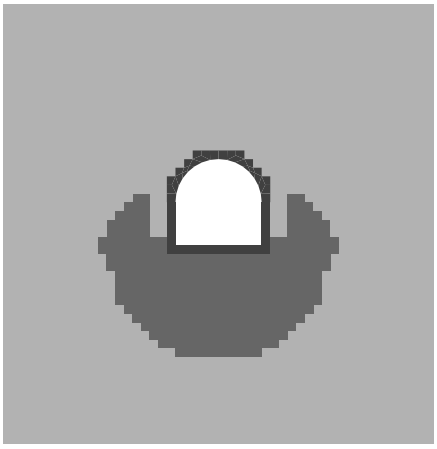

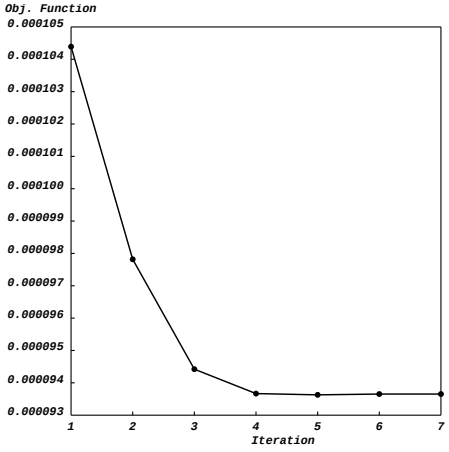

(c) $\sigma_3 = \sigma_1$

Figure 5.17 Optimum reinforcement for minimising floor heave.

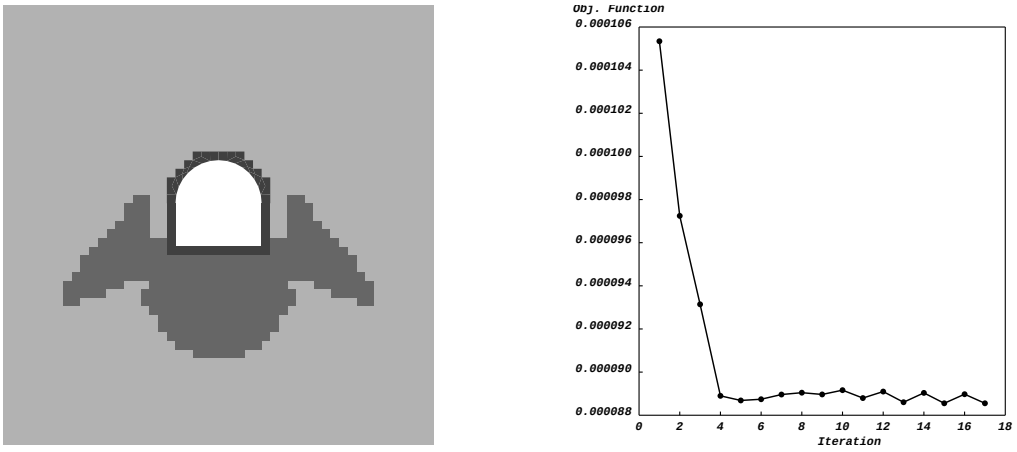

(d) $\sigma_3 = 1.3\sigma_1$

Figure 5.17 Optimum reinforcement for minimising floor heave (continued).

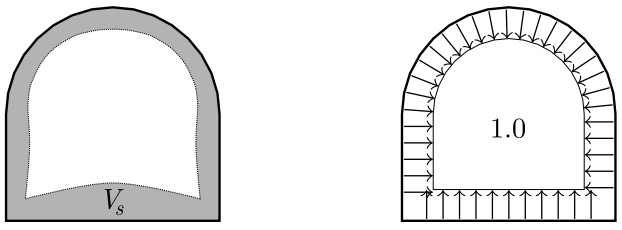

Figure 5.18 The new load case to evaluate tunnel convergence.

Similarly the sensitivities of v can be expressed as

$$\frac{\partial v}{\partial x_i} = -\tilde{\mathbf{u}}_i{}^T \frac{\partial \mathbf{K}_i}{\partial x_i} \mathbf{u}_i \tag{5.16}$$

Implementing these results, the tunnel convergence minimisation problem is solved to find the optimum distribution of reinforcement. The results are reported in Figure 5.19.

Although the optimum designs are varying for different in-situ stress ratios, unlike the other two objectives, the convergence minimisation results are not very sensitive to the in-situ stress ratios. In all designs, the tunnel is surrounded by a nearly uniform reinforcement distribution. The value of the objective function is changing smoothly and monotonically in all cases and a clear convergence can be observed.

In floor heave and convergence minimisation problems, in each iteration two models should be analysed by the finite element solver. The solution time is thus longer than compliance minimisation. This advantage of mean compliance is due to its self-adjoint property. However, the stiffness matrix for both models in each iteration remains the same. Hence, in floor heave and tunnel convergence minimisations, one can store this stiffness matrix (or even its inverse) to reduce the solution time.

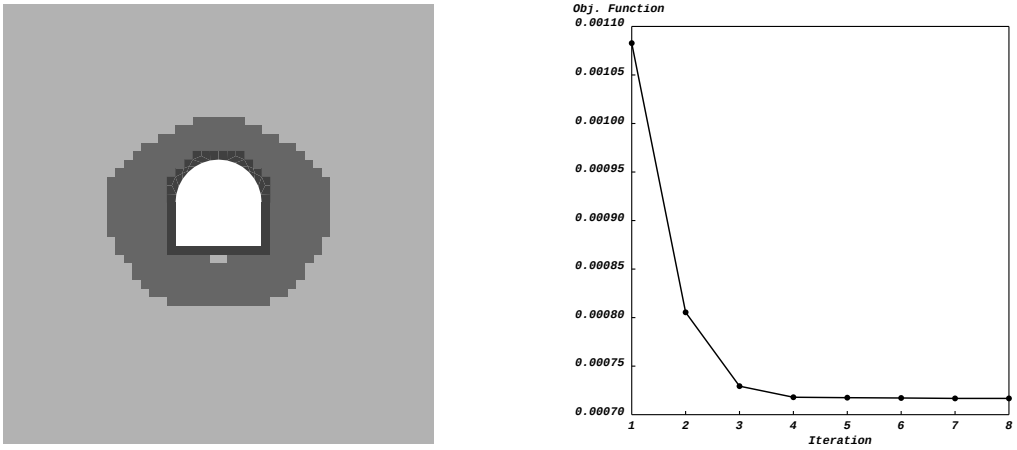

(a) $\sigma_3 = 0.4\sigma_1$

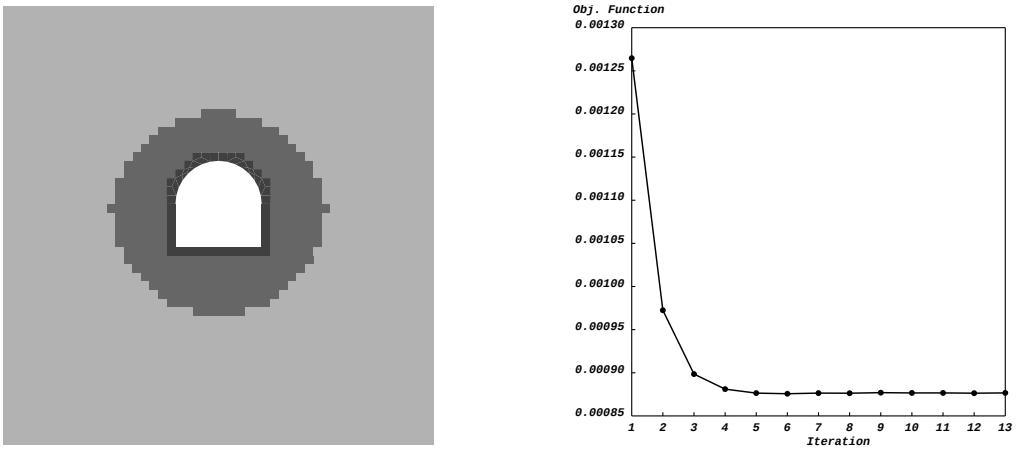

(b) $\sigma_3 = 0.7\sigma_1$

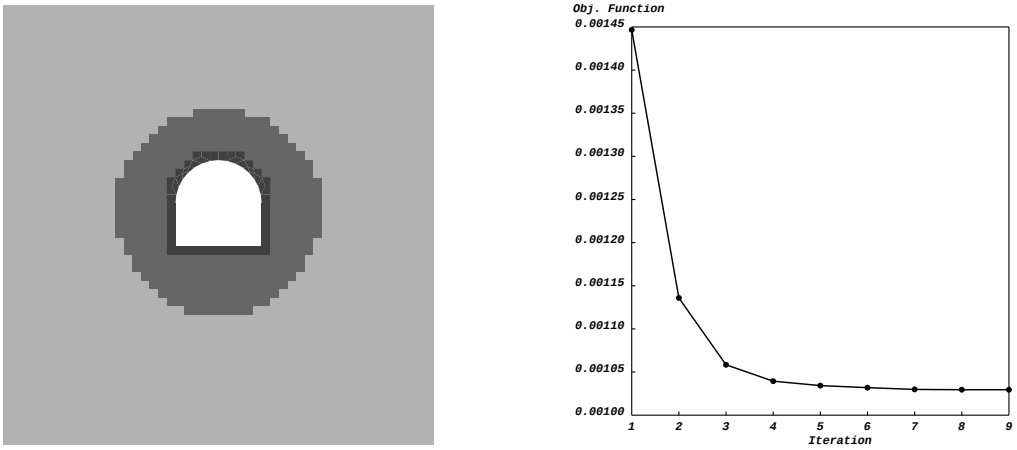

(c) $\sigma_3 = \sigma_1$

Figure 5.19 Optimum reinforcement for minimising tunnel convergence.

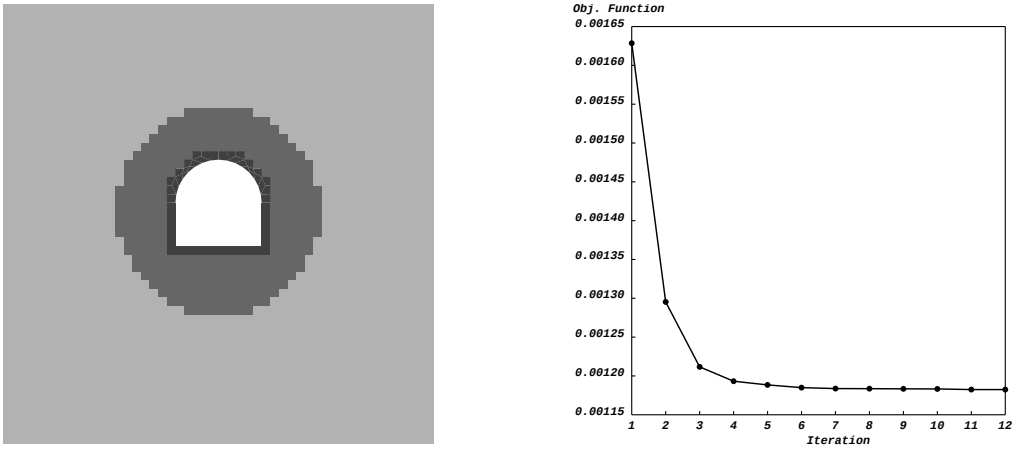

(d) $\sigma_3 = 1.3\sigma_1$

Figure 5.19 Optimum reinforcement for minimising tunnel convergence (continued).

5.5 Simultaneous shape and reinforcement optimisation

In the previous sections the proposed BESO algorithm proved to be successful in dealing with shape and reinforcement optimisation of tunnels. Noting that both problems have been solved as material distribution problems, one may try to solve them simultaneously.

In this case a three phase material can be assumed changing between voids, original rock, and reinforced rock. The moduli of elasticity of these material phases are respectively denoted by E^V, E^O, and E^R with $\frac{E^V}{E^O} = 0.001$ and $\frac{E^O}{E^R} = 0.3$. The Poisson's ratio is assumed to be similar for all the three materials and equal to 0.3.

The mean compliance is assumed as the objective function. Note that the tunnel convergence can not be used as the objective for shape optimisation

as the shape of the tunnel is going to change. Considering the floor heave as the objective function is also not possible for shape optimisation. Even if one fixes the tunnel's floor, because the floor heave function takes only a few points into account, the final shape of the tunnel will be an impractical flat shape.

Considering the mean compliance as the objective function, the optimisation problem can be stated as

$$\begin{aligned} &\min_{\mathbf{x},\mathbf{y}} c = \mathbf{f}^T\mathbf{u} \\ \text{such that } &\mathbf{K}\mathbf{u} = \mathbf{f}, \\ &V_R = \sum_{i=1}^{n} x_i V_i = \bar{V}_R, \\ &V_V = \sum_{i=1}^{n} (1-y_i) V_i = \bar{V}_V, \\ &x_i, y_i \in \{0,1\} \end{aligned} \tag{5.17}$$

where $\mathbf{x}$ and $\mathbf{y}$ are vectors of the two sets of design variables for reinforcement and shape optimisation respectively. For the i-th element, $x_i = 0$ denotes original rock and $x_i = 1$ denotes reinforced rock properties. For the same element, $y_i = 0$ represents void and $y_i = 1$ represents solid (either reinforced or original rock).

Like reinforcement optimisation, a layer of shotcrete is assumed around the tunnel. The shotcrete mechanical properties are taken similar to reinforced rock. The shotcrete layer is added to the model by changing the boundary elements of the tunnel to reinforced elements at each iteration. The active set for the shape optimisation thus merely consists of voids and

reinforced elements. Hence the material phases for the shape optimisation procedure reduce to voids and reinforced rock only.

The shape optimisation follows by reinforcement optimisation in each iteration. At this level some inefficient reinforced elements loose their reinforcement and some efficient rock elements are reinforced. In order to maintain the shotcrete layer after shape optimisation, the reinforced boundary elements are freezed and are not allowed to change in the reinforcement optimisation in that iteration. As the shape changes, the number of boundary elements might change. This can modify the reinforcement volume after shape optimisation violating reinforcement volume constraint. To maintain the volume constraint, the number of strengthening and weakening elements are then adjusted in the reinforcement optimisation procedure.

Mixing the two optimisation problems and solving them together theoretically results in better designs than solving one after the other. Furthermore, noting the formulation of sensitivity numbers for the two optimisation problems one can see that they are only different in their coefficients. Precisely speaking, the term $\mathbf{u}_i^T \mathbf{K}_i \mathbf{u}_i$ is the same in sensitivity number of the i-th element in both shape and reinforcement optimisation. The remaining part of the sensitivity numbers is merely a function of Young's moduli and penalisation factors and thus can be readily calculated. Hence, using this approach, the two optimisation problems are being solved for the price of one.

To illustrate the capabilities of the proposed BESO algorithm, the problem (5.17) is solved for different load cases and initial designs. The modified linear interpolation scheme is used for both shape and reinforcement optimisations. Using (4.24), this material interpolation is equivalent to using

the alternative interpolation (4.19) with $q = \frac{10000}{3} - 1 = 3332.3$ for shape optimisation and with $q = \frac{10}{3} - 1 = 2.33$ for reinforcement optimisation. The filtering technique is employed to prevent numerical anomalies and provide smoother boundaries. The filtering radius is assumed to be $r_f = 2h$ for both shape and reinforcement optimisation. The move limit is selected as $m = 10$ for shape optimisation and $m = 100$ for reinforcement optimisation.

5.5.1 Tunnel under biaxial stresses

Figure 5.20 shows the initial design as well as the applied loads and supports.

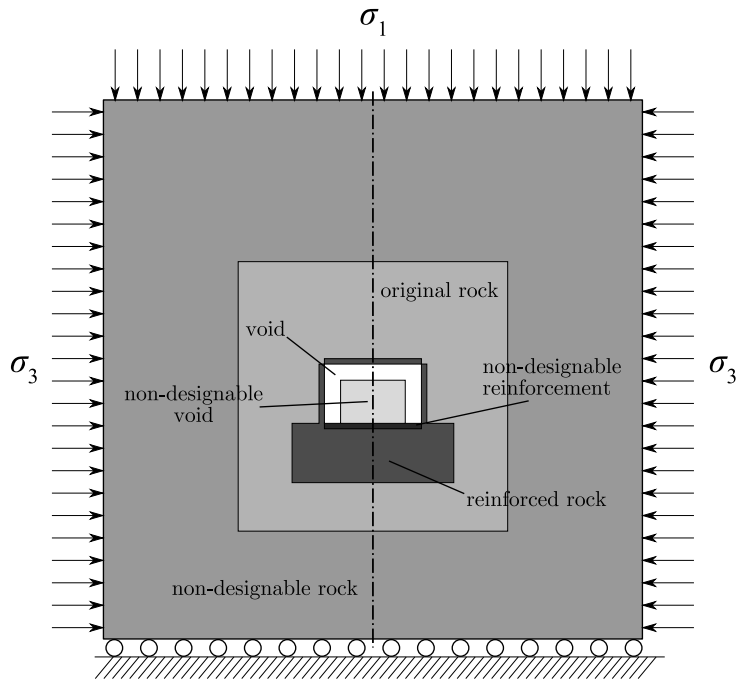

Figure 5.20 Initial design of a reinforced tunnel under biaxial stresses.

The obtained results are reported in Figure 5.21.

The smoothing procedure described in §5.3.2 can be employed here to smooth the cavity shapes. The smoothed version of the results reported in

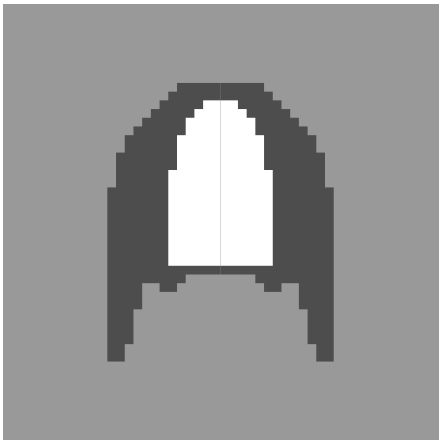

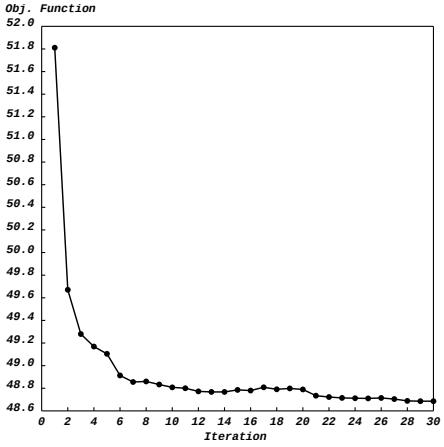

(a) $\sigma_3 = 0.4\sigma_1$

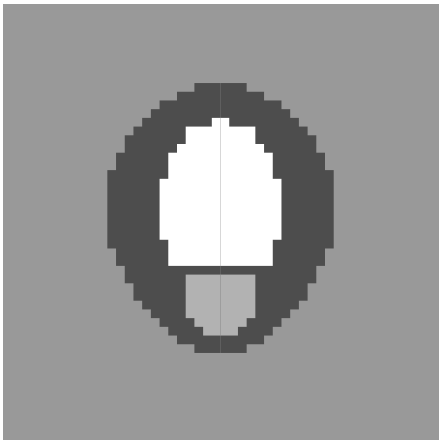

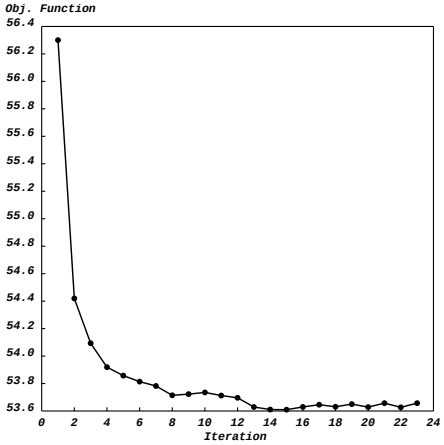

(b) $\sigma_3 = 0.7\sigma_1$

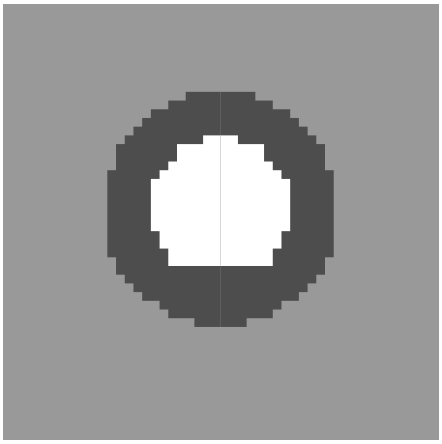

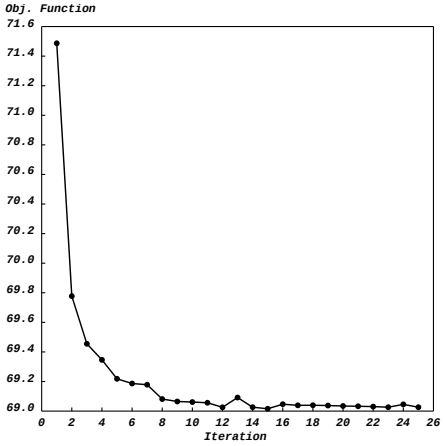

(c) $\sigma_3 = \sigma_1$

Figure 5.21 Optimum shape and reinforcement of tunnels under biaxial stresses.

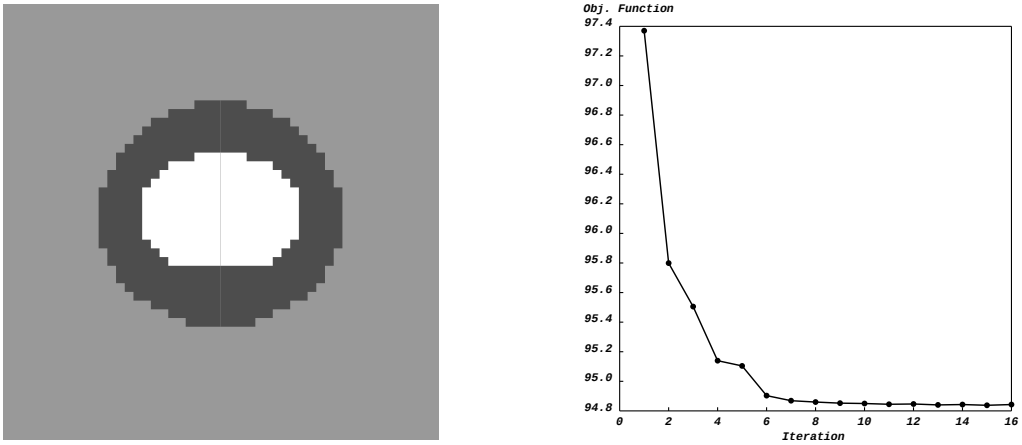

(d) $\sigma_3 = 1.3\sigma_1$

Figure 5.21 Optimum shape and reinforcement of tunnels under biaxial stresses (continued).

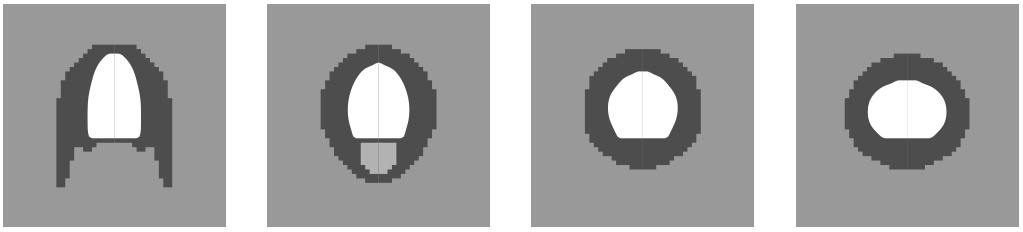

(a) $\sigma_3 = 0.4\sigma_1$ (b) $\sigma_3 = 0.7\sigma_1$ (c) $\sigma_3 = 1.0\sigma_1$ (d) $\sigma_3 = 1.3\sigma_1$

Figure 5.22 Smoothed shape for the results reported Figure 5.21.

Figure 5.21 are given in Figure 5.22.

The relatively smooth and monotonic decrease of the objective function values shows that the procedure works well. Note the similarities between the shape of the cavities in Figure 5.22 and the optimum shapes reported in Figure 5.9. However, the obtained reinforcement designs are not very similar to the designs reported in Figure 5.15. This suggests that the shape of the opening is more critical than the reinforcement distribution in minimum compliance design.

The similar problem is considered with a traffic load applying on the

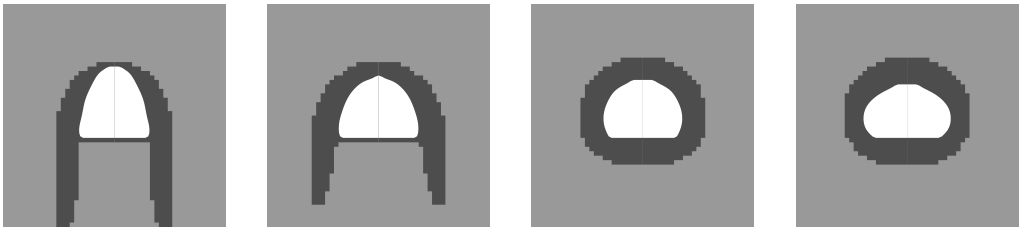

(a) $\sigma_3 = 0.4\sigma_1$ (b) $\sigma_3 = 0.7\sigma_1$ (c) $\sigma_3 = 1.0\sigma_1$ (d) $\sigma_3 = 1.3\sigma_1$

Figure 5.23 Optimum shape and reinforcement of tunnels with traffic load.

tunnel's floor. The intensity of the traffic load is assumed as $\sigma_{tr} = 0.25\sigma_1$. The opening shapes are smoothed using Bézier curves after optimisation. The optimum designs are shown in Figure 5.23.

Like the previous examples, applying the traffic load makes the shapes shorter and wider.

5.5.2 Two parallel tunnels

The shape and reinforcement design of two parallel tunnels are considered here as another example. The design domain and the initial distribution of materials are depicted in Figure 5.24.

The problem is first considered without traffic load ($\sigma_{tf} = 0.0$). The optimum results are reported in Figure 5.25 after smoothing the opening shapes.

The last example involves applying a traffic load of $\sigma_{tr} = 0.25\sigma_1$ on the tunnels' floor. The final results are reported in Figure 5.26.

It is interesting to note that the reinforcement of the two tunnels tend to join as the horizontal stress increases.

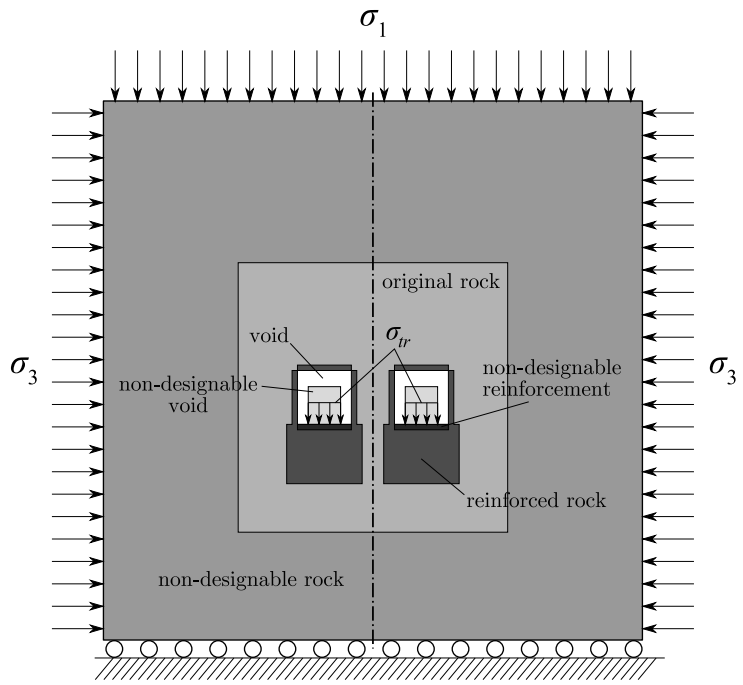

Figure 5.24 Initial design of two reinforced parallel tunnels.

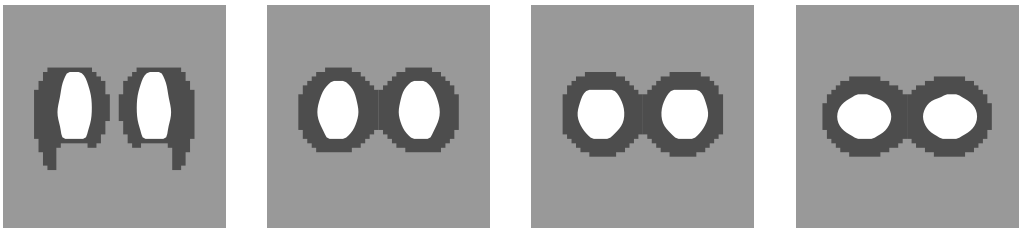

(a) $\sigma_3 = 0.4\sigma_1$ (b) $\sigma_3 = 0.7\sigma_1$ (c) $\sigma_3 = 1.0\sigma_1$ (d) $\sigma_3 = 1.3\sigma_1$

Figure 5.25 Optimum shape and reinforcement of two parallel tunnels.

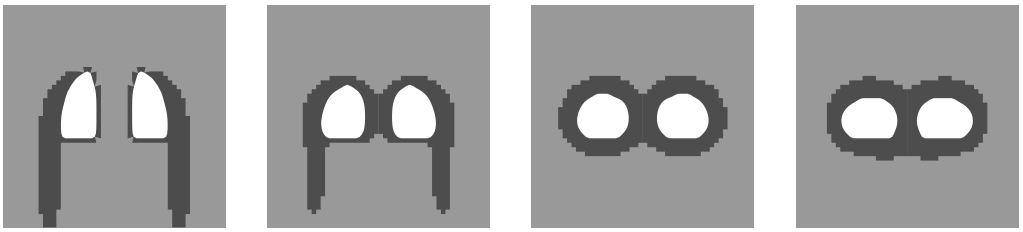

(a) $\sigma_3 = 0.4\sigma_1$ (b) $\sigma_3 = 0.7\sigma_1$ (c) $\sigma_3 = 1.0\sigma_1$ (d) $\sigma_3 = 1.3\sigma_1$

Figure 5.26 Optimum shape and reinforcement of two parallel tunnels with traffic load.

5.6 Concluding remarks

The optimisation technique previously proposed in Chapter 4 has been used to find the optimum shape of underground excavations and the optimum reinforcement around them in linear elastic media. Although linear elastic models in many cases can not model the behaviour of ground materials with appropriate accuracy, as a first step, implementing such material model can be instructive. Also the linear results can be found useful in verifying empirical designs and in considering the effects of time-dependent creep in rock mass.

Shape optimisation of excavations has been demonstrated through a series of examples. A smoothing post-processor has been proposed using the Bézier curves. A simple example has been used to verify the obtained results by comparing them to analytical solutions. More examples have been presented to show the capability of the proposed method to deal with different types of problems.

The next part of the chapter has focused on reinforcement optimisation of tunnels. Three different objective functions have been introduced and used including the mean compliance, floor heave, and tunnel convergence. In the case of floor heave minimisation, a good correlation has been observed between the obtained results and the results published in the literature.

The proposed optimisation method has been found to be capable of dealing with both shape and reinforcement optimisation of tunnels. As the next step these two optimisation problems have been solved simultaneously using this method. Some examples have been solved to show the capability of the

proposed method in solving this new mixed optimisation problem.

Although all the examples solved here are in plane strain situation, it should be noted that theoretically there is no limitation in applying the proposed method to three dimensional cases.

The main limitation of the current approach is its linear elastic behaviour assumption. In next chapters we will focus on dealing with this limitation mainly. Apart from this research path, further studies can be conducted on using other objective functions and solving more detailed examples.

CHAPTER 6

Introducing discontinuities

6.1 Introduction

In the previous chapter the rock mass has been modelled as a homogeneous, isotropic, linear elastic material. This assumption limits the applicability of the proposed approach to the intact rocks or heavily jointed rock masses where the isotropic and homogeneous behaviour can be justified. In many cases, however, the mechanical behaviour of rock mass is highly affected by few major discontinuities. In these kind of rock masses the separation and slippage of major discontinuities should be explicitly considered in numerical modelling. The reinforcement optimisation for underground openings in such rock masses is the subject of this chapter. The discontinuities are assumed to have no tensile strength and slip according to Coulomb's friction criterion.

6.2 Modelling excavation in massive rock

In massive rocks the overall behaviour of the rock mass is influenced by one or two major discontinuities. These discontinuities create some weakness planes

along which the shear strength is effectively reduced. The tensile strength normal to discontinuities generally vanishes, but the compressive strength does not alter from intact rock. The following linear Coulomb's friction criterion can be used to predict the shear strength along discontinuities.

$$|\tau| = \sigma_n \tan \phi_d \tag{6.1}$$

with compressive stresses being defined as positive values. Here τ and σ_n are the shear and normal stresses tangent and normal to the discontinuity line respectively. The friction angle ϕ_d depends on the roughness of discontinuity surfaces and mineralogy of the rock material.

The overall behaviour of massive rocks is not homogeneous or isotropic due to possible slippage and separation of discontinuities. However, if one prevents any sort of separation or slippage on discontinuity lines, the cracked parts of the rock mass can transfer loads just same as intact rock and hence these simplifying assumptions can still be validated. In this case a linear elastic solution can give a first order approximation of actual responses. To ensure that no slippage or separation may occur, the slipping or separating spots should be located along discontinuities and properly reinforced. In this manner the overall rock mass can be viewed as a continuum. Using the linear analysis considerably reduces the convergence time of the topology optimisation which usually requires tens of finite element analyses. Moreover the loading sequence is not important in linear analysis which simplifies the numerical modelling. Finally, as the linear analysis results are an approximation of the more realistic elasto-plastic models, optimisations based on linear

elastic analysis can considerably improve the empirical designs, although to find the actual global optimum, more sophisticated models are required.

6.3 Analysing discontinuity lines

In the algorithm proposed here, any discontinuity line segment is introduced with the coordinates of its two end points. Having these coordinates, the pre-processor routine can recognise the elements through which this crack segment passes. We refer to these elements as *cracked elements*. The cracked elements are defined as the elements having at least one common point with the discontinuity line. The discontinuity line intersects with the boundary of the cracked elements in one or two points. One node intersection can happen in two cases. One of these cases is when the crack line is started from within an element. The other is the case where the discontinuity line passes through one of the element's nodes. In this case all elements sharing that node will be considered as cracked elements. Some examples of cracked elements are illustrated in Figure 6.1.

Any discontinuity line is divided by its associated cracked elements into some *crack segments*. Any of the cracked elements contain one crack segment which can be a line segment or a single node (Fig. 6.1a). If any slippage or separation occurs along a crack segment, the containing cracked element should be stabilised. To analyse a crack segment, its mid-point is considered as the representative point. That is, a crack segment is considered unstable if and only if its mid-point is unstable. These mid-points are termed as *crack*

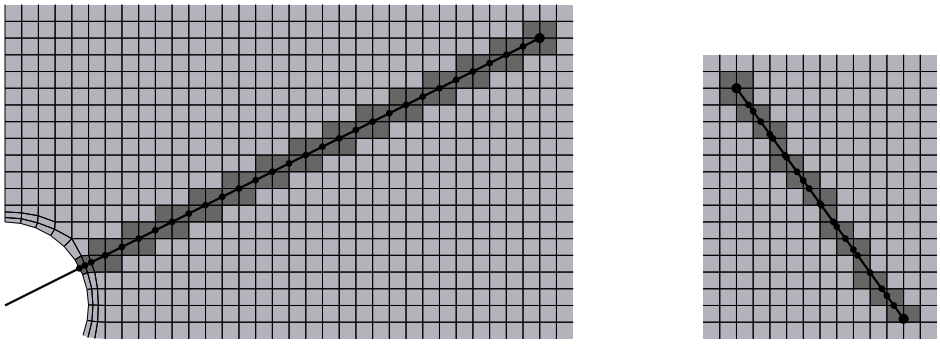

a) Cracked elements and crack segments

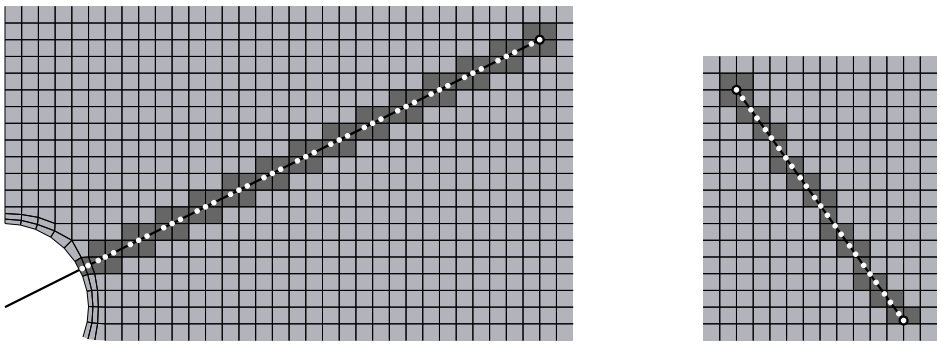

b) Crack points

Figure 6.1 Cracked elements, crack segments and crack points.

points (Fig. 6.1b). In this manner, any discontinuity line passing through n_c cracked elements is represented by n_c crack points each lying in one cracked element. Figure 6.2 shows some possible configuration of crack points.

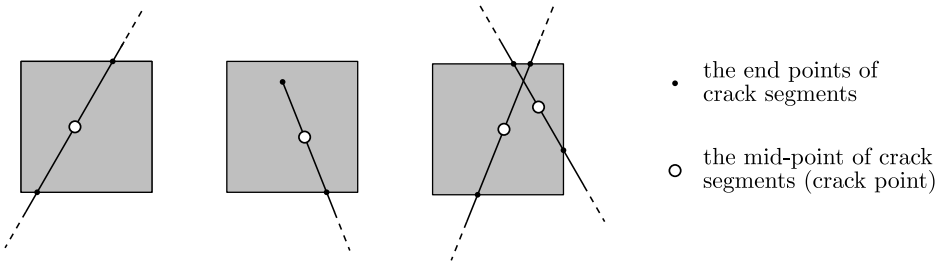

Figure 6.2 Some possible configurations of crack segments and crack points within elements.

For each discontinuity line, the list of cracked elements and their crack points are stored along with the direction angle of the discontinuity line. The stability checks will be performed on the crack points after the finite element analysis in each iteration. The principal stresses at the crack points will be derived from the finite element analysis results. The values of the normal and shear stresses along the crack direction will then be calculated from the principal stresses. For separation, as no tensile strength is assumed for discontinuities, the value of the normal tensile stress is taken as the separation indicator. This relationship is expressed as

$$I_{spr} = \max\{0, -\sigma_n\} \tag{6.2}$$

The crack points with higher separation indicator are assumed to be more critical against separation. For slipping, based on (6.1), the slippage indicator is defined as

$$I_{slp} = \max\{0, |\tau| - \sigma_n \tan\phi\} \tag{6.3}$$

The crack points with higher slipping indicator are assumed to be more prone to slippage. The elements containing crack points with higher value of $I_{spr} + I_{slp}$ are reinforced first. If for a crack point $I_{spr} + I_{slp} = 0$ that point is considered safe without reinforcement.

The stabilisation procedure stabilises the crack elements by reinforcing them. This reinforcement alters the initial problem. Consequently the state of stability of the system might change after this reinforcement and the system might become unstable. To bypass this problem one should stabilise the system gradually and iteratively. In this way the stabilisation algorithm is permitted to only stabilise a limited number of unstable elements in each iteration. This limits the alteration of the system. Then the model is re-analysed and stabilised again. This process continues until all unstable elements are treated. The maximum number of stabilising elements in an iteration is denoted by m_s henceforth and referred to as *stabilisation move limit*.

To stabilise a location on a discontinuity plane, the two surfaces should be fixed together. In practise this can be achieved by using anchored rock bolts acting perpendicular to the discontinuity plane. However, it is not always possible to install the rock bolts normal to the discontinuity plane. In such cases one should try to install them as perpendicular as possible so that their performance would be maximised.

In the reinforcement distribution design considered in topology optimisation, the reinforced rocks are modelled using a homogenised material and the orientation of rock bolts is assumed to have no effects. However in case of discontinuity stabilisation one should note that which parts of the discontinuity need to be stabilised and what the best orientation of rock bolts

is. Figure 6.3 illustrates this issue. The algorithm thus needs to clearly distinguish between the normal and stabilising reinforcement although the material used to model them might be similar.

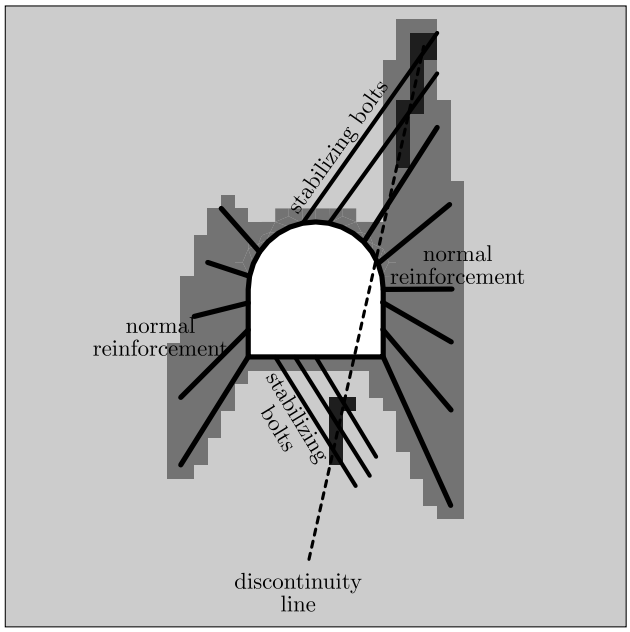

Figure 6.3 Orientation of stabilising rock bolts. Unstable cracked elements are filled with darker grey.

6.4 Verification

Brady and Brown (2006) have studied the effect of discontinuities on elastic stress distribution around circular excavations. This problem is considered here to verify the proposed stabilisation approach.

Consider a circular opening in elastic rock with initial vertical and horizontal stresses of p and Kp as shown in Figure 6.4. Stress distribution around

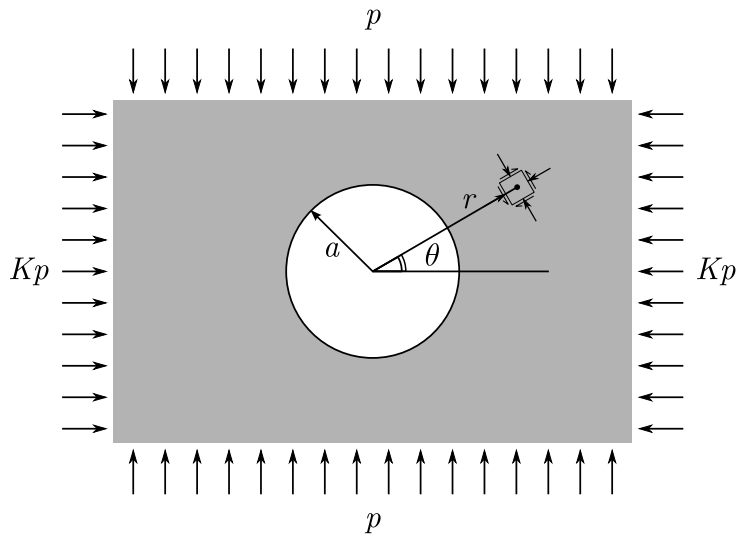

Figure 6.4 A circular excavation in homogeneous rock.

this cavity can be calculated as (Yu 2000)

$$\sigma_{rr} = \frac{p}{2}\left[(1+K)\left(1-\tfrac{a^2}{r^2}\right) - (1-K)\left(1-4\tfrac{a^2}{r^2}+3\tfrac{a^4}{r^4}\right)\cos 2\theta\right] \tag{6.4a}$$

$$\sigma_{\theta\theta} = \frac{p}{2}\left[(1+K)\left(1+\tfrac{a^2}{r^2}\right) + (1-K)\left(1+3\tfrac{a^4}{r^4}\right)\cos 2\theta\right] \tag{6.4b}$$

$$\sigma_{r\theta} = \frac{p}{2}\left[(1-K)\left(1+2\tfrac{a^2}{r^2}-3\tfrac{a^4}{r^4}\right)\sin 2\theta\right] \tag{6.4c}$$

where positive values denote compression stress in (6.4a) and (6.4b), and a is the radius of the cavity.

Three different cases with a single discontinuity line are considered here for verification. These cases are depicted in Figure 6.5.

To verify the proposed stabilisation procedure, these three cases are solved with this procedure and the results obtained after few iterations are compared with analytical solutions. It should be noted that the proposed stabilisation algorithm uses a stiffer material to stabilise the unstable crack elements. This alters the initial model and hence the numerical results might not completely

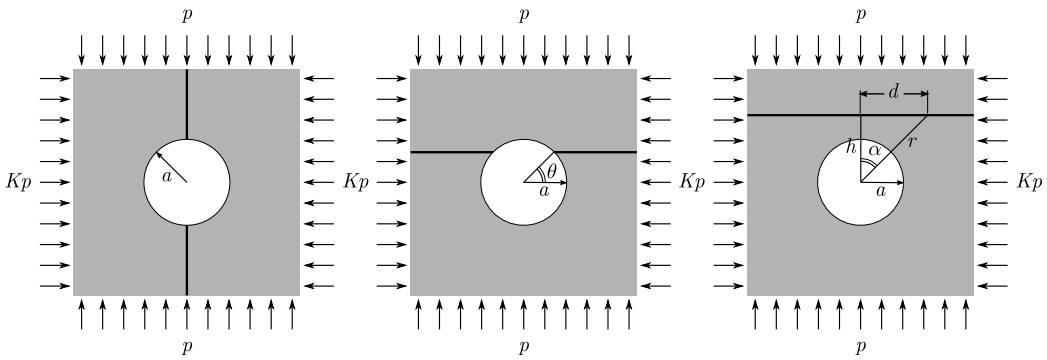

a) case 1 b) case 2 c) case 3

Figure 6.5 Geometry of the three verification cases: a) a vertical radial joint; b) a horizontal joint passing through the opening; c) a non-intersecting horizontal joint.

match the analytical solutions. Moreover, the finite element discretisation error in numerical models affects the numerical results.

Case 1

For the vertical discontinuity, $\theta = 90°$ and thus according to (6.4c) shear stress vanishes along the discontinuity line. So this discontinuity is not prone to slippage. However separation can occur due to tensile stress normal to the crack line. From (6.4b) one can deduce that a tension can develop on the discontinuity line in the crown of the opening ($r = a$) when

$$\sigma_{\theta\theta} = p\,[(1 + K) - 2(1 - K)] = p(3K - 1) \leq 0 \tag{6.5}$$

which simplifies to $K \leq \frac{1}{3}$. Therefore, in this case the discontinuity line is safe when lateral stress is bigger than a third of vertical stress. For smaller values of K rock separation may occur in the crown of the opening.

To check the proposed stabilisation algorithm for this case, a linear elastic

media with a circular hole is discretised to form a finite element mesh. The friction angle of the discontinuity is set to $\phi_d = 10°$ although this value does not affect the possible separation. To produce comparable results with analytical solutions, no reinforcement is added. The model is solved for different values of K being $\frac{1}{6}$, $\frac{1}{3}$, and $\frac{1}{2}$. The obtained results can be found in Figure 6.6

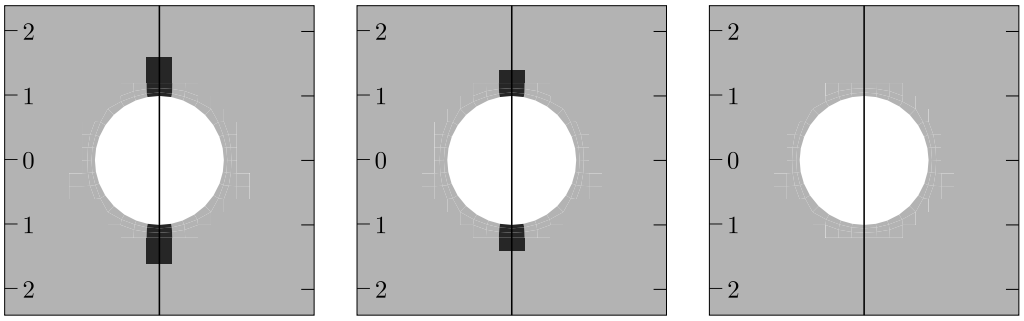

(a) $K = \frac{1}{6}$ (b) $K = \frac{1}{3}$ (c) $K = \frac{1}{2}$

Figure 6.6 Numerical results for case 1.

The obtained results show a good consistency with the analytical solutions. It can be seen that the separation zone enlarges as K decreases and no separation occurs when $K > \frac{1}{3}$.

Case 2

For the case shown in Figure 6.5b, the normal and the shear stress acting on the plane of weakness can be found from the following equations.

$$\sigma_n = \sigma_{\theta\theta} \cos^2 \theta \tag{6.6a}$$

$$\tau = \sigma_{\theta\theta} \sin \theta \cos \theta \tag{6.6b}$$

Substituting these values into (6.1), the limiting condition for slipping can be found as $\tan\theta = \tan\phi_d$. Hence slipping happens if $\theta \geq \phi_d$. The slipping zone would develop at the intersection of the opening and the plane of weakness.

For verification, a circular hole with the radius of unity is considered. A horizontal discontinuity line is added which cuts the opening at half of the radius above the opening's centre. Hence $\theta = \sin^{-1}\frac{1}{2} = 30^\circ$ in this case. Using (6.6a) the values of τ/σ_n are calculable for different distances from the cavity centre along the discontinuity line. The variation of this parameter is depicted in Figure 6.7.

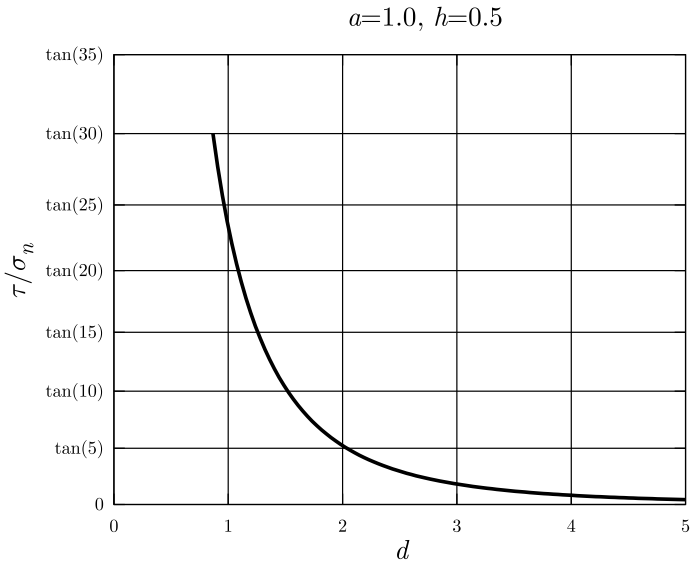

Figure 6.7 Values of τ/σ_n along the discontinuity line for case 2.

Using (6.1), slippage takes place along the discontinuity line wherever $\tau/\sigma_n \geq \phi_d$. It can be seen that τ/σ_n reaches its maximum value at the horizontal distance of $d = \cos(30^\circ) = 0.866$ from the opening's centre which is at the boundary of the opening. As we move farther from the opening, this value decreases. It can be concluded from Figure 6.7 that slipping zone

develops at the intersection of the opening and the plane of weakness as ϕ_d falls below 30°. The slipping zone enlarges as ϕ_d decreases. For the case of $\phi_d > 30°$ no slipping is spotted and the discontinuity does not need any stabilisation.

To verify the algorithm in this case, the model is tested with three different values of ϕ_d. Figure 6.8 illustrates the results.

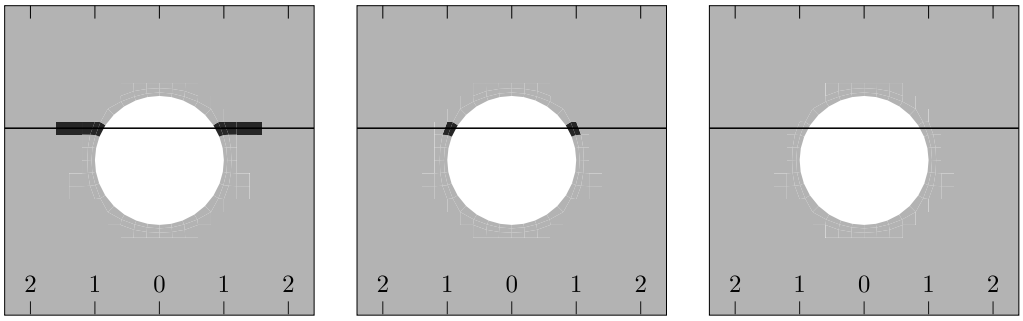

(a) $\phi_d = 10°$ (b) $\phi_d = 20°$ (c) $\phi_d = 30°$

Figure 6.8 Numerical results for case 2.

It can be seen that numerical results match reasonably with the graph in Figure 6.7. Note that in Figure 6.8b the numerical result does not show any slippage. This is due to the error caused by finite element discretisation. Precisely speaking, the reason is that the crack point in the first cracked element is not exactly at the boundary of the hole.

Case 3

The geometry of the third case is illustrated in Figure 6.5c. Implementing the notation used in Figure 6.5c, the normal and the shear stress acting on

the plane of weakness can be formulated as

$$\sigma_n = \tfrac{1}{2}(\sigma_{rr} + \sigma_{\theta\theta}) + \tfrac{1}{2}(\sigma_{rr} - \sigma_{\theta\theta})\cos 2\alpha \tag{6.7a}$$

$$\tau = \sigma_{r\theta}\cos 2\alpha - \tfrac{1}{2}(\sigma_{rr} - \sigma_{\theta\theta})\sin 2\alpha \tag{6.7b}$$

For simplicity a hydrostatic stress field is assumed ($K = 1.0$). The above equations thus reduce to

$$\sigma_n = p\left(1 - \tfrac{a^2}{r^2}\cos 2\alpha\right) \tag{6.8a}$$

$$\tau = p\tfrac{a^2}{r^2}\sin 2\alpha \tag{6.8b}$$

Like case 2, one can evaluate the ratio of τ/σ_n for different values of $d = r\sin\alpha$ and compare it with $\tan\phi_d$. The values of $\tau/\sigma_n \geq \tan\phi_d$ would indicate slippage. The graph depicted in Figure 6.9 shows the variation of this ratio along the discontinuity line for $h = 1.5$ and $a = 1.0$.

According to this graph the shear stress is zero just above the opening's centre and then reaches its maximum value at a horizontal distance less than the opening radius. It can be seen that the discontinuity line is totally stable for ϕ_d being slightly greater than 20° *.

The proposed stabilising approach is tested on case 3 for values of $\phi_d = 10^\circ$, $\phi_d = 15^\circ$, and $\phi_d = 20^\circ$. The numerical results are shown in Figure 6.10

Again the slight difference between numerical and analytical results is due to the finite element discretisation error. Apart from that the numerical results in Figure 6.10 are consistent with the graph in Figure 6.10.

*Using (6.8) the exact position of the maximum is calculable as $d = 0.645$ and $\tau/\sigma_n = \tan 20.149^\circ$.

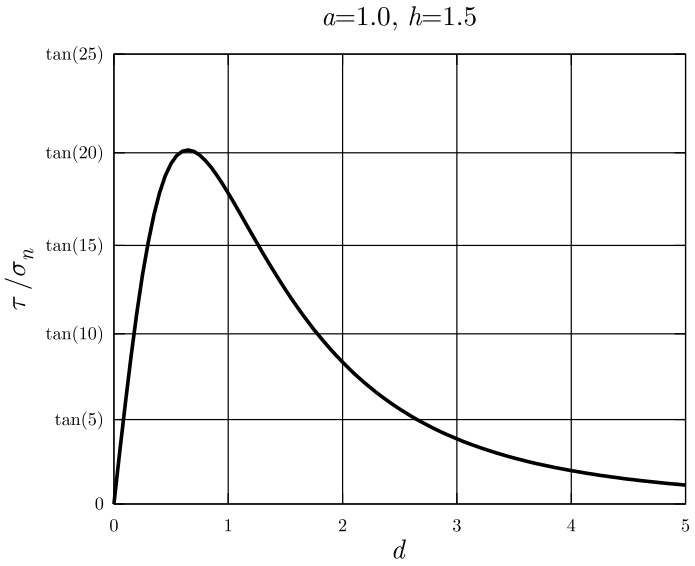

Figure 6.9 Values of τ/σ_n along the discontinuity line for case 3.

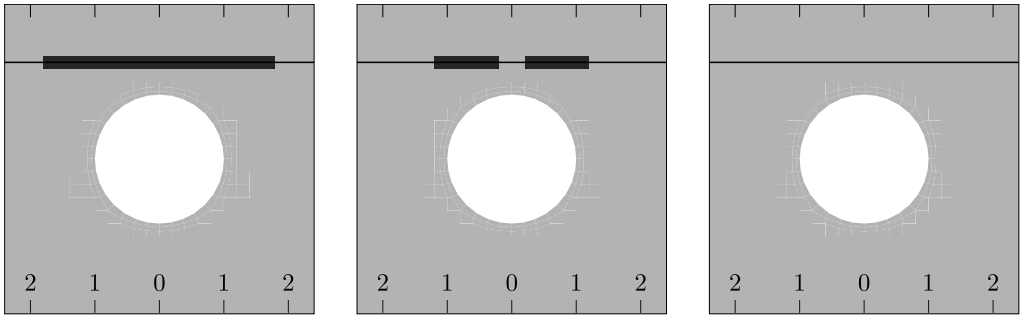

(a) $\phi_d = 10°$ (b) $\phi_d = 15°$ (c) $\phi_d = 20°$

Figure 6.10 Numerical results for case 3.

Although in these verification cases the analytical solutions were fairly easily achievable, this is not the case in most of situations. Notably the slipping or separation zone might considerably change when reinforcement is added. To illustrate this the resulted design in Figure 6.10b is reinforced by swapping some rock elements to reinforced rock. Figure 6.11 compares the stabled results obtained before and after adding additional reinforcement.

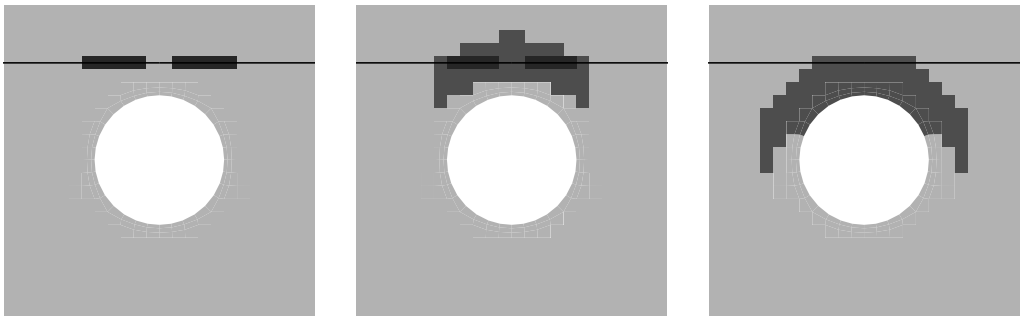

(a) no additional reinforcement (10 reinforced elements)

(b) with 50 reinforced elements

(c) with 80 reinforced elements

Figure 6.11 Unstable zone before and after adding additional reinforcement.

It can be seen that the slipping zone becomes smaller after using 50 reinforced elements. Adding more reinforcement, this area completely disappears with 80 reinforced elements.

6.5 Optimisation procedure

After stabilising possible unstable zones on weakness planes, linear elastic behaviour can be assumed for the rock media. In this case, the optimisation procedure proposed in previous chapter (§5.4) can be employed to optimise the reinforcement around the opening. To ensure that the system is stable in

all iterations, the proposed stabilisation algorithm is called in each iteration before calculating the sensitivity numbers.

In order to prevent the optimisation engine from removing the reinforcement of critical crack points, the reinforcement of the elements containing these points should be frozen for one iteration. In the following iterations, however, these reinforced elements will be again considered designable if their crack points are found to be safe.

This process is in accordance to the procedure proposed by Brady and Brown (2006) for excavation design in elastic massive rocks.

After stabilising the system, the sensitivity numbers of all designable elements are calculated. Based on these sensitivity numbers some inefficient reinforced elements lose their reinforcement and a number of efficient rock elements are reinforced. The maximum number of elements that can be changed in an iteration is limited to the predefined move limit. After updating the design, the system goes through the stabilisation process again. This process continues until the results converge to a final solution.

6.6 Examples

In this section the capability of the proposed method is demonstrated through numerical examples. A tunnel is considered under biaxial stresses and plane strain condition. The design domain and initial distribution of reinforcement are depicted in Figure 6.12.

A shotcrete layer surrounds the opening with similar mechanical proper-

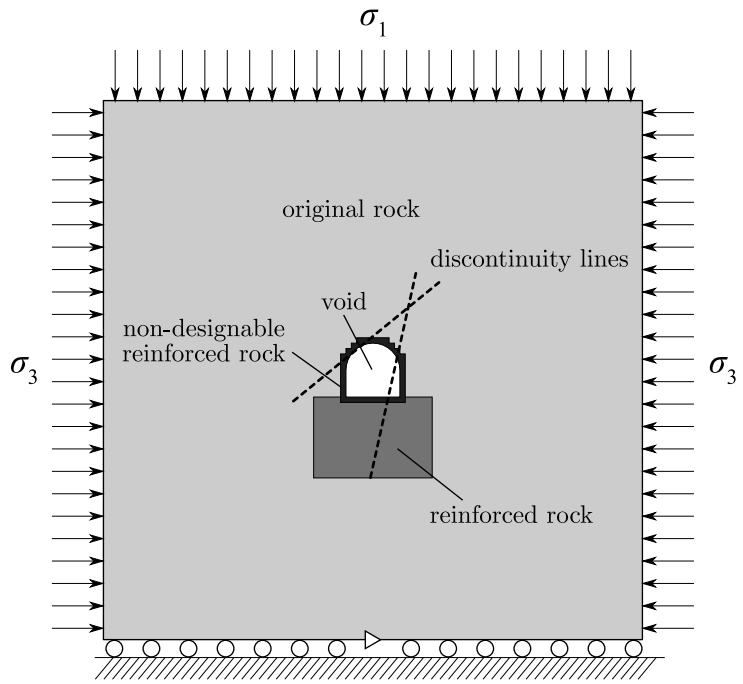

Figure 6.12 Initial reinforcement distribution of a tunnel in a rock mass with few discontinuities.

ties to reinforced rock. This layer is fixed to reinforced rock. The volume of reinforced area is fixed to 3.7% of the domain size. The ratio of moduli of elasticity of the reinforced and the original rock is considered as $\frac{E^R}{E^O} = \frac{10}{3}$. Because of discontinuities the domain is not symmetric and the full model should be used for finite element analysis. The filtering radius is chosen as $r_f = 2.5h$ with h denoting the element size. The move limit and the stabilisation move limit are selected as $m = 40$ and $m_s = 2$ elements respectively. Like previous chapter, the modified linear interpolation is used for material interpolation. The applied stress ratio is assumed as $\frac{\sigma_3}{\sigma_1} = \frac{1}{2}$.

6.6.1 Minimum compliance design

In the first example the initial design in Figure 6.12 is optimised to yield the minimum compliance. The minimum compliance design problem is defined in (5.5). The friction angle for discontinuities is assumed as $\phi_d = 15°$. The final solution is depicted in Figure 6.13.

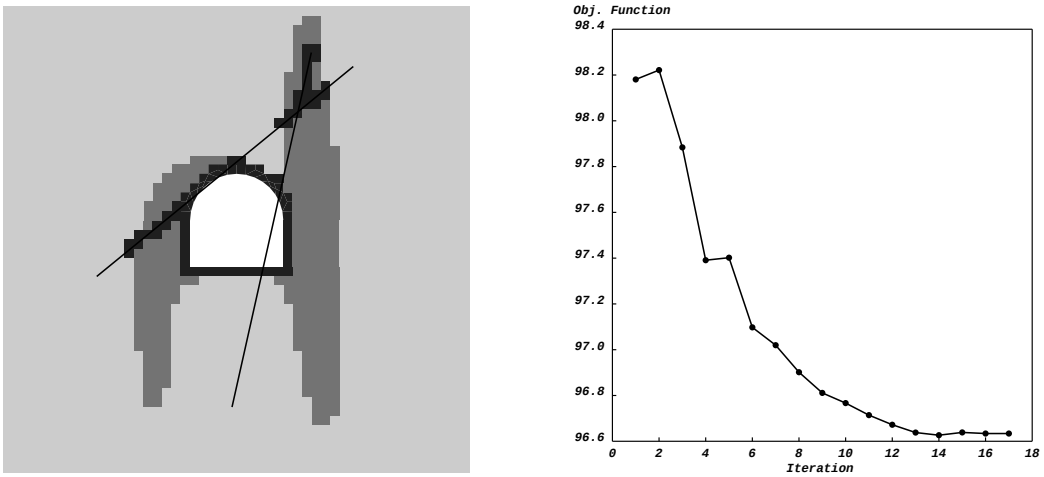

Figure 6.13 Optimum reinforcement for minimising compliance in tunnel with discontinuities, $\phi_d = 15°$.

Comparing Figure 6.13 with Figure 5.15, it can be seen that the evolution of the value of the objective function is not as monotonic as it was without discontinuities. This is due to stabilisation process that unavoidably disturbs the optimisation path.

To show the effect of discontinuities on the final topology, the problem is solved with $\phi_d = 20°$, $\phi_d = 30°$, and without discontinuities as well. Figure 6.14 compares the final topologies obtained. It can be seen that the final topology might change considerably if one involves the effect of discontinuities in the model.

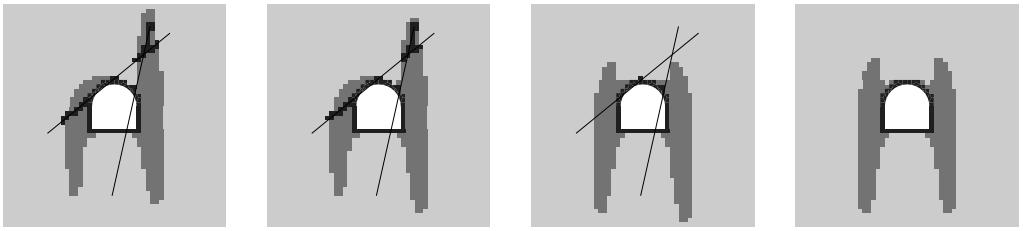

(a) $\phi_d = 15°$ (b) $\phi_d = 20°$ (c) $\phi_d = 30°$ (d) no crack

Figure 6.14 The effect of discontinuities in the final topology after compliance minimisation.

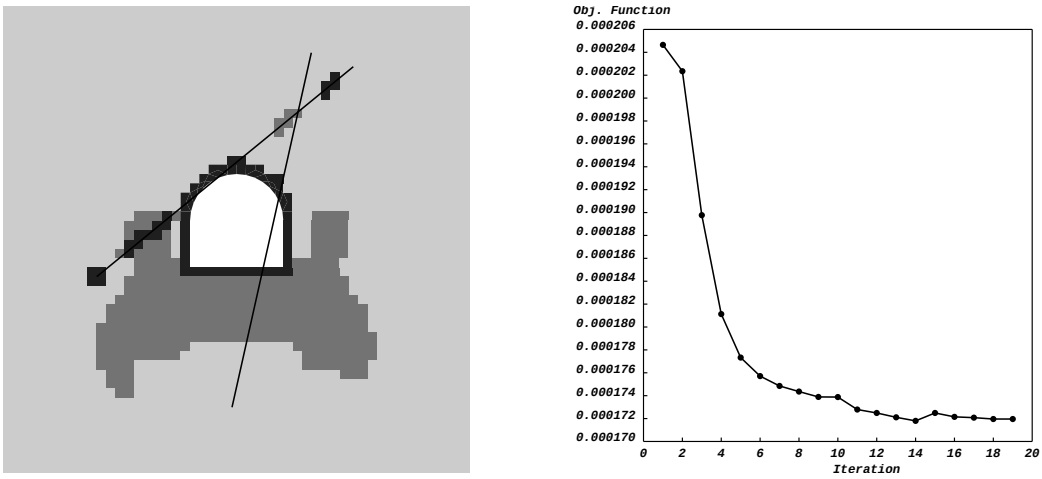

Figure 6.15 Optimum reinforcement for minimising floor heave in tunnel with discontinuities, $\phi_d = 15°$.

6.6.2 Minimising the floor heave

The floor heave minimisation problem has been defined in (5.8) with $\tilde{\mathbf{f}}$ defined in Figure 5.16. The initial design depicted in Figure 6.12 is optimised for minimising the floor heave. Figure 6.15 illustrates the results with $\phi_d = 15°$.

The effect of the friction angle of discontinuities is demonstrated in Figure 6.16 where the final topologies with $\phi_d = 15°$, $\phi_d = 20°$, $\phi_d = 30°$ and without discontinuities are compared to each other.

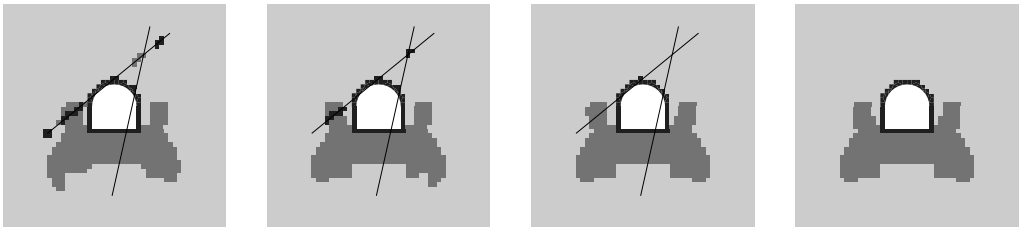

(a) $\phi_d = 15°$ (b) $\phi_d = 20°$ (c) $\phi_d = 30°$ (d) no crack

Figure 6.16 The effect of discontinuities in the final topology after minimising the floor heave.

6.6.3 Minimising the tunnel convergence

The third example deals with tunnel convergence as the objective function. The tunnel convergence minimisation problem is defined as

$$\begin{aligned} \min_{x_1,x_2,\ldots,x_n} \quad & v = \tilde{\mathbf{f}}^T \mathbf{u} \\ \text{such that} \quad & \mathbf{K}\mathbf{u} = \mathbf{f}, \\ & \mathbf{K}\tilde{\mathbf{u}} = \tilde{\mathbf{f}}, \\ & V_R = \sum_{i=1}^{n} x_i V_i = \bar{V}_R, \\ & x_i \in \{0, 1\} \end{aligned} \tag{6.9}$$

with $\tilde{\mathbf{f}}$ defined in Figure 5.18.

The initial design depicted in Figure 6.12 is optimised for minimising the tunnel convergence and the results are reported in Figure 6.17. Again the value of $\phi_d = 15°$ is adopted for friction angle of discontinuities.

Figure 6.18 illustrates the effect of discontinuities' friction angle on the final topology.

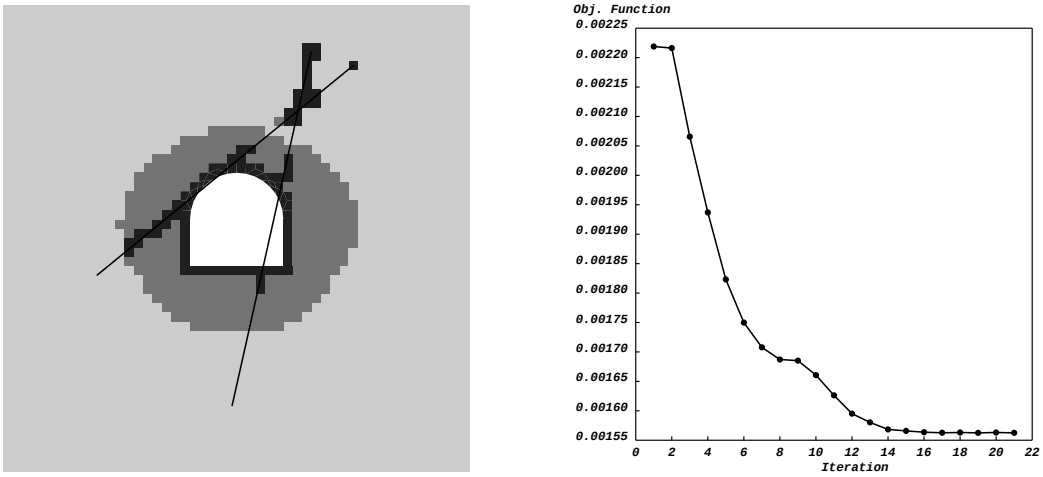

Figure 6.17 Optimum reinforcement for minimising tunnel convergence in tunnel with discontinuities, $\phi_d = 15°$.

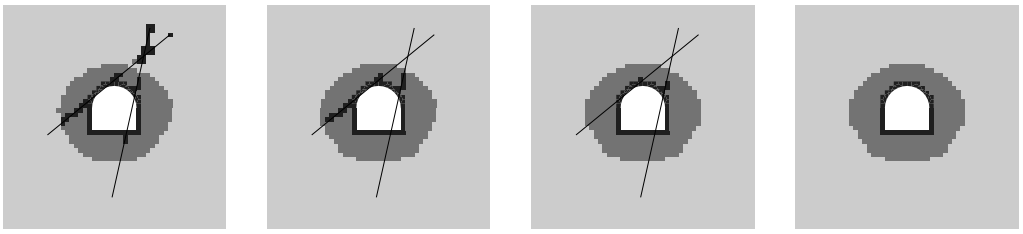

(a) $\phi_d = 15°$ (b) $\phi_d = 20°$ (c) $\phi_d = 30°$ (d) no crack

Figure 6.18 The effect of discontinuities in the final topology after minimising the tunnel convergence.

6.6.4 Considering multiple objective functions

In order to minimise two or more objective functions together one should define a multi-objective optimisation problem. Suppose two objective functions f and g must be minimised together. To do so, one can define the following multiple objective function

$$r(\mathbf{x}) = w_f \cdot f(\mathbf{x}) + w_g \cdot g(\mathbf{x}) \tag{6.10}$$

where $\mathbf{x}$ indicates the vector of design variables. The two scalar weighting factors w_f and w_g can be used to apply different weights to f and g.

Two examples are solved using this kind of multiple objective definition. The friction angle of discontinuities is taken as $\phi = 15°$ in these examples. The initial reinforcement distribution in Figure 6.12 is used in these examples as well. In the first example the objective function is defined as $f = 0.0001c + 0.9999h$ where c and h are mean compliance and floor heave respectively. The relatively large weight factor chosen for floor heave is due to the fact that the values of floor heave are much smaller than values of mean compliance. The final topology and the evolution of c and h are illustrated in Figure 6.19.

It can be seen that the two objective functions have both reduced and converged. However, the evolution of the objective functions is not very smooth and not monotonic which is expected in multi-objective problems. The final topology differs from results of any of these functions alone (Fig. 6.13 and Fig. 6.15).

Next example deals with minimising $f = 0.001c + 0.999v$ where v is tunnel convergence. A large weight factor is used for tunnel convergence to

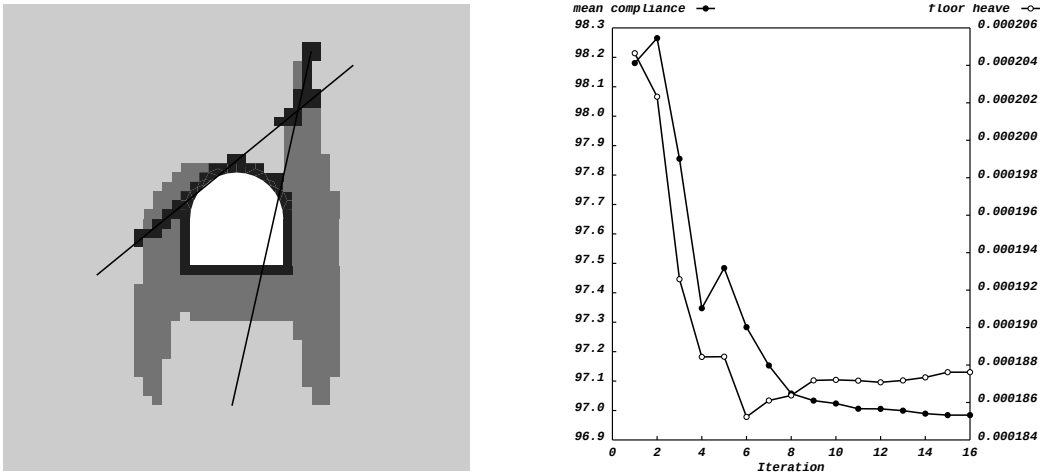

Figure 6.19 Optimum reinforcement for minimising $f = 0.0001c + 0.9999h$, $\phi_d = 15°$.

balance its smaller values when mixed with larger values of mean compliance. Figure 6.20 shows the final topology and the evolution of the two objective functions.

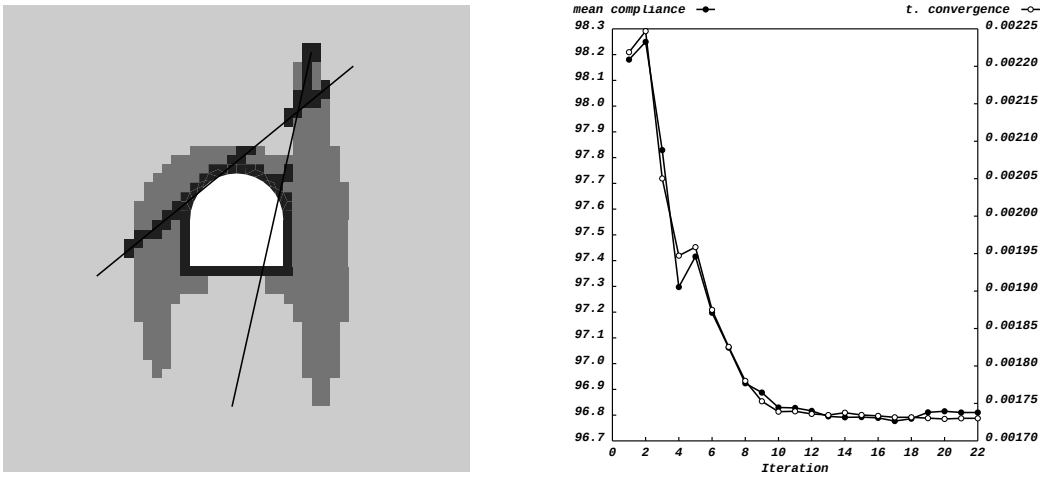

Figure 6.20 Optimum reinforcement for minimising $f = 0.001c + 0.999v$, $\phi_d = 15°$.

The reduction in the two objective functions is relatively monotonic. The final solution is different from the results of either of these functions alone

(Fig. 6.13 and Fig. 6.17), but is more close to the minimum compliance design (Fig. 6.13).

If the two objective functions are always positive, one can also use a simpler multiple objective function definition as follows

$$r(\mathbf{x}) = f(\mathbf{x})g(\mathbf{x}) \tag{6.11}$$

This definition does not need weighting factors. As in our case all the objective functions are always positive, it is possible to use this definition. The sensitivities of this multiple objective function can be then calculated as

$$\frac{\partial r}{\partial x_i} = f(\mathbf{x})\frac{\partial g}{\partial x_i} + g(\mathbf{x})\frac{\partial f}{\partial x_i} \tag{6.12}$$

After finding the sensitivities with respect to design variables, the sensitivity numbers can be easily calculated based on the assumed material interpolation scheme (see Chapter 4).

Two examples are solved here to illustrate the use of this multiple objective definition. The initial reinforcement distribution in Figure 6.12 is used for these examples and the friction angle of discontinuities is assumed as $\phi = 15°$. The first example minimises the floor heave and the mean compliance together. The final topology and the evolution of the objective functions are depicted in Figure 6.21. The second example involves minimising the tunnel convergence and the mean compliance together. The results are shown in Figure 6.22.

The final topology in Figure 6.21 is more close to the floor heave min-

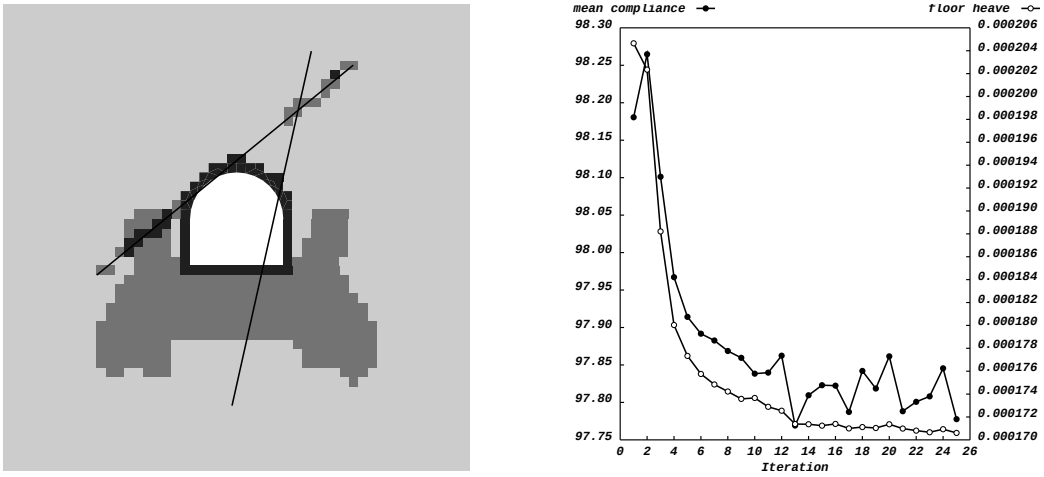

Figure 6.21 Optimum reinforcement for minimising $f = c \cdot h$, $\phi_d = 15°$.

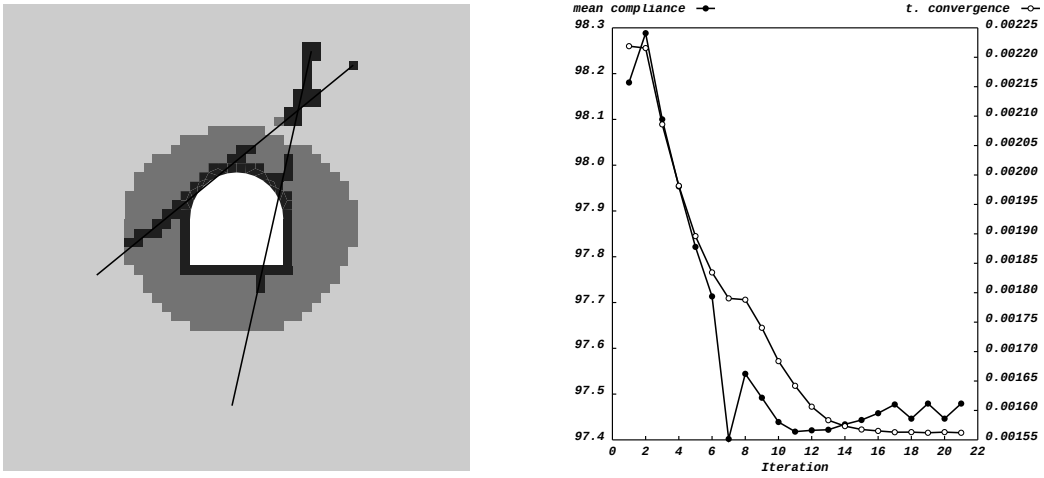

Figure 6.22 Optimum reinforcement for minimising $f = c \cdot v$, $\phi_d = 15°$.

imisation result (Fig. 6.15). Also the final topology in Figure 6.22 is more close to the tunnel convergence minimisation solution (Fig. 6.17). However in both cases it can be seen that both of the objective functions ultimately decrease.

6.7 Concluding remarks

This chapter has been devoted to reinforcement optimisation of tunnels in rocks with discontinuities. The rock material has been assumed linear elastic. However because of the discontinuities the homogeneity and isotropy assumptions are not valid in this case. To overcome this one can reinforce the discontinuities accordingly to prevent any sort of slippage and separation. After this stabilisation, the rock mass can be viewed as a continuum media.

A stabilisation algorithm has been introduced in this chapter to ensure that no slippage or separation occurs along discontinuities. This algorithm stabilises the rock mass iteratively. The results of this algorithm have been verified by comparing its results with analytical solutions in some simple cases.

The stabilising algorithm has been embedded inside the optimisation algorithm. The capabilities of the new algorithm has been demonstrated via some numerical examples. The optimum design of tunnels to achieve the minimum compliance, the minimum floor heave, and the minimum tunnel convergence have been obtained.

Finally two formulations for multi-objective optimisation problems have

been introduced. Two numerical examples have been solved to demonstrate the concept.

The next chapter deals with shape optimisation of tunnels in elasto-plastic media.

CHAPTER 7

Optimising tunnels in elasto-plastic media

7.1 Introduction

In this section the shape optimisation of excavations in elasto-plastic soils is addressed. Ren et al. (2005) considered this problem in linear elastic media. We first review this work and then extend it to non-linear material models.

The ESO method has been used by Ren et al. (2005) to optimise the shape of the openings. This method suits this sorts of problem as its material removal can model the actual excavation process. Here the same method will be used to find the optimum shape of the openings.

7.1.1 Difficulties when considering inelastic behaviour

The behaviour of geomaterials is usually non-linear. However using such material models in topology optimisation may lead to several limitations and difficulties. The extremely high computational effort required to solve such examples is one of the barriers. This becomes more significant if one recalls that topology optimisation techniques normally require tens of finite

element runs.

But there are more important difficulties in considering inelastic behaviours. Including inelastic behaviour, geomechanical responses will depend on the loading path. In this case if one wants to consider the sequences of excavating a tunnel, sensitivity analysis will become extremely difficult if not impossible. Furthermore, as the inelastic responses depend on the loading path, the final topologies may not be comparable to each other.

To bypass the sensitivity analysis difficulty, here we use the ESO method with an intuitively defined efficiency measure.

7.2 Previous works

The ESO method has been described in §2.6. A key concept in this method is the definition of the rejection criterion. The rejection criterion assigns a scalar value to elements which will be compared with a threshold value to determine whether the element should be removed or not. One of the flexibilities of this method is that the rejection criterion in the method can be either defined intuitively or calculated rigorously. In their paper, Ren et al. (2005) used an intuitive stress-based ESO and defined the following rejection criterion.

$$\bar{\sigma} = \frac{\sigma_1 + \sigma_2 + \sigma_3}{3} \tag{7.1}$$

where σ_1, σ_2, and σ_3 are principal stresses. The mean stress value $\bar{\sigma}$ is used to evaluate the efficiency of the elements.

The threshold stress level is then defined based on two controlling param-

eters. The first one is the rejection ratio, denoted as RR. This parameter has been described in §2.6. In order to limit the number of removing elements, Ren et al. (2005) defined another parameter named as volume removal rate, VR. This is defined as the ratio of the maximum allowable number of removing elements to the total number of elements in each iteration.

Two threshold values are defined based on these two parameters as

$$\sigma_{th1} = \bar{\sigma}_{max} \cdot RR \tag{7.2}$$

and

$$\sigma_{th2} = \bar{\sigma}(n(1 - VR)) \tag{7.3}$$

where n is the number of elements in each iteration; $\bar{\sigma}(n(1 - VR))$ denotes the value of the $(n(1 - VR))$-th highest mean stress among all designable elements. Ren et al. (2005) then defined the threshold stress level as the minimum of these two values

$$\sigma_{th} = \min\{\sigma_{th1}, \sigma_{th2}\} \tag{7.4}$$

After finding the threshold stress level the elements are removed wherever the mean stress value is found to be less than the threshold stress level.

Ren et al. (2005) solved some numerical examples in two and three dimensions and verified their results with analytical solutions. Moreover, through a 3D example of two intersecting tunnels, they showed that the solution can be considerably different if one uses the von Mises stress as the rejection criterion.

7.3 A rejection criterion for Mohr-Coulomb material model

The Mohr-Coulomb model is one of the most common material models used to model the behaviour of soils. It is reasonable to define the rejection criterion based on the material model in use. Here we define a new rejection criterion based on the Mohr-Coulomb material model.

As mentioned before in §3.2, the Mohr-Coulomb yield function can be expressed in terms of principal stresses $\sigma_1 \geq \sigma_2 \geq \sigma_3$ as

$$f = (\sigma_1 - \sigma_3) - (\sigma_1 + \sigma_3)\sin\phi - 2c\cos\phi \qquad [3.3]$$

where ϕ and c are the friction angle and the cohesion of soil material respectively and compressive stresses are considered positive. In this model the stress-strain relationship is linear elastic wherever the yield function is negative. The value of zero for the yield function indicates yielding and the strains induced after this level are no more reversible.

Figure 7.1 shows the Mohr-Coulomb yield function in the $\sigma - \tau$ space together with a possible stress state $(\sigma_1, \sigma_2, \sigma_3)$ which is illustrated using the Mohr's circles. If the largest circle touches the Mohr-Coulomb envelope the soil element will yield. Clearly, as the confining stress $(\sigma_1 + \sigma_3)/2$ increases, the centre of the largest circle shifts to the right side and the soil element can endure higher stresses before yielding. The 'distance' between the largest circle and the Mohr-Coulomb envelope is denoted by x in Figure 7.1. This

distance can be calculated as (Ghabraie et al. 2008)

$$x = c\cos\phi + \left(\frac{\sigma_1 + \sigma_3}{2}\right)\sin\phi - \left(\frac{\sigma_1 - \sigma_3}{2}\right) \tag{7.5}$$

The radius of the largest Mohr circle can be expressed as

$$r = \frac{\sigma_1 - \sigma_3}{2} \tag{7.6}$$

Now we define an efficiency measure, or sensitivity number, as

$$\alpha = \frac{r}{r + x} = \frac{\sigma_1 - \sigma_3}{2c\cos\phi + (\sigma_1 + \sigma_3)\sin\phi} \tag{7.7}$$

This value shows the ratio of the maximum possible radius of the Mohr's circle to the current largest radius for a stress state.

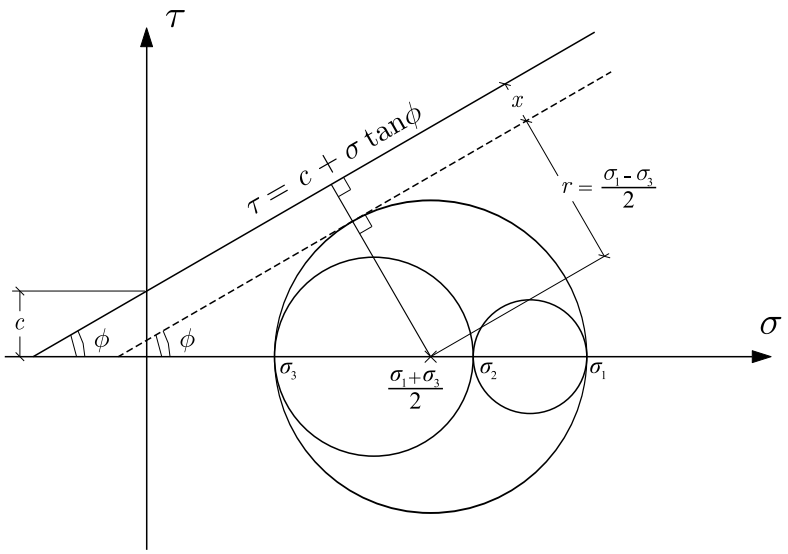

Figure 7.1 The distance between the largest Mohr's circle and the Mohr-Coulomb envelope.

This definition provides a dimensionless parameter varying between zero

(the least efficient case) and one (the most efficient case).

7.4 The ESO procedure for excavation problem

In excavation problem due to the nature of the problem, the classical ESO process should be amended to well fit the problem.

7.4.1 Defining the front layer

Since the shape optimisation of the opening is of concern, at each step we can only remove elements from the boundary of the opening, the *front layer*. This is also in consistency with the real procedure of excavating a hole in the ground. In 2D problems, an existing element is regarded as a member of the front layer if and only if it has at least two common nodes with at least one of the previously removed elements. This concept is similar to the active set ($\mathcal{A}$) described in detail in §4.9. However, unlike the active set, the front layer only contains solid elements. If we denote the set of removed and existing elements by $\mathcal{V}$ and $\mathcal{M}$ respectively, then the front layer can be defined as

$$\mathcal{F} = \{e \in \mathcal{M} | \exists e_v \in \mathcal{V} : e \cap e_v = \{i, j\}\} \tag{7.8}$$

The front layer (active set) at each iteration is defined using the hole generated in the previous iterations. Hence, for the first step we need an initial hole to start with which should be removed manually.

7.4.2 Removing elements

In the ESO method, the rejection ratio (RR) is traditionally used to define a threshold stress level as a ratio of the maximum stress level in the form (Xie and Steven 1993; Ren et al. 2005)

$$\sigma_{th} = \sigma_{max} \cdot RR \tag{7.9}$$

In our case, however, because of the definition of sensitivity number as a dimensionless value, instead of using a ratio, an explicit rejection level (RL) is used. Elements with sensitivity number lower than this rejection level ($\alpha \leq RL$) will be nominated for removal. Obviously rejection level should be greater than zero and smaller than one. Similar to Ren et al. (2005) a second control parameter, volume removal rate (VR), is defined here as the ratio of the maximum allowable amount of deletion over the design domain volume.

The optimisation algorithm controls the number of removing elements by means of RL and VR. To find the removing elements, first all the elements in the front layer are sorted based on their sensitivity number calculated from (7.7). Then the number of elements with the sensitivity lower than rejection level are found and stored in N_1. The maximum allowed number of removing elements is then determined as

$$N_2 = \lfloor VR \cdot N_f \rfloor \tag{7.10}$$

in which N_f stands for the number of elements in front layer. The number

of removing elements (N_r) is calculated as follows

$$N_r = \max\{\min\{N_1, N_2\}, 1\} \tag{7.11}$$

This guarantees that at least one element is removed at each iteration.

In case of symmetry, if the relative error between sensitivity numbers of the last removing element and the next (remaining) one becomes less than a predefined tolerance (0.05% throughout this chapter) then both of them should be deleted.

As a general rule, using lower control parameters, may lead to a better result but requires more iterations. For all examples presented in this chapter the values of $RL = 0.3$ and $VR = 10\%$ are adopted.

7.4.3 Termination criteria

To evaluate the performance of the hole generated after each iteration, the following performance index (PI) is defined based on the definition of the sensitivity number in (7.7)

$$PI = \frac{\sum_{i \in \mathcal{F}} \alpha_i}{N_f} \tag{7.12}$$

The limited number of removing elements in each step results in different shapes after each optimisation loop. Thus performance index will fluctuate during optimisation process making several peaks. These peaks resemble relatively similar shapes but in different sizes (Fig. 7.2).

The ESO algorithm utilised here terminates the procedure when the pre-

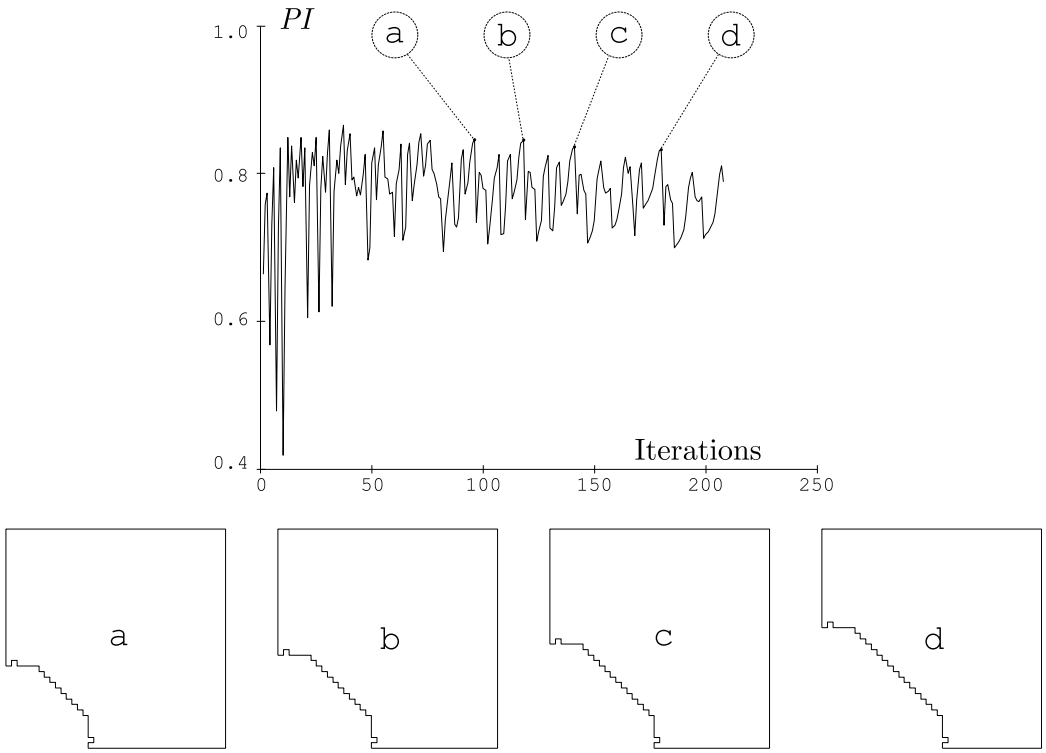

Figure 7.2 Fluctuations of the PI value with several peaks related to similar shapes in different sizes.

defined size of the hole is achieved and the performance index reaches one of its peaks. Thus after reaching the desired hole size, the procedure continues removing elements, but at the first iteration where PI drops after a raise, the procedure is terminated and the last hole obtained is reported as the final result.

The complete algorithm is described in Figure 7.3

1: Discretise the problem's domain.
2: Initialise RL and VR
3: **repeat**
4: Find the front layer
5: Perform FE analysis and calculate the sensitivity numbers for the front layer elements using (7.7).
6: $N_1 \leftarrow$ number of elements with $\alpha \leq RL$
7: $N_2 \leftarrow \lfloor VR \cdot N_f \rfloor$
8: $N_r \leftarrow \max\{\min\{N_1, N_2\}, 1\}$
9: Remove N_r elements with lowest values of α
10: **until** Desired volume has been achieved and PI has reached one of its peaks
11: **print** the results
12: **end**

Figure 7.3 Algorithm for shape optimisation of tunnels using ESO.

7.5 Examples

Two examples are solved using the proposed method. The first example is a simple example used here to compare the obtained results and the elastic linear results. The second one is a tunnel in soil where the only load is the weight of the soil mass.

7.5.1 Comparing the linear and non-linear results

The problem's geometry is shown in Figure 7.4. For linear elastic weightless materials, the optimal shape is elliptical with its aspect ratio matching the in-situ stress ratio (Hoek and Brown 1980; Cherkaev et al. 1998; Pedersen 2000). This shape provides the stiffest design. Also the tangential stress and the energy density along the boundary of this shape are uniform (Pedersen 2000).

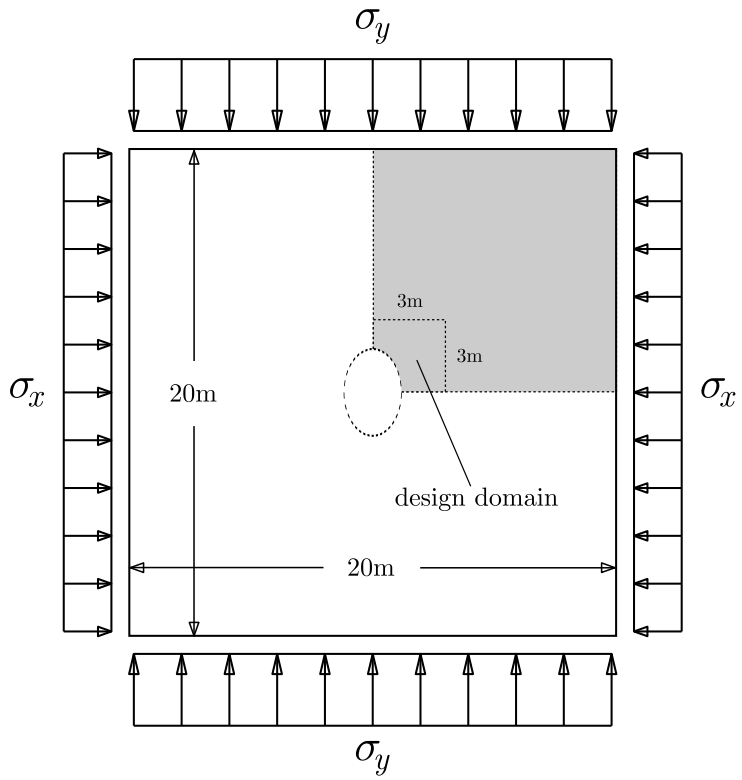

Figure 7.4 The sketch of the 2D problem used in the first example.

For this example four load cases are considered as described in Table 7.1. The first and the third cases correspond to a hydrostatical stress field, while the second and the fourth cases are biaxial stress cases with the applied stress

ratio of 2. As a result the linear elastic optimum solutions include a circular hole for the first and the third cases and an elliptical hole with aspect ratio of 2 for the second and the fourth cases. Figure 7.5 shows these optimum shapes.

Table 7.1 Load cases for the first example.

Case	σ_x (kPa)	σ_y (kPa)
1	20	20
2	10	20
3	40	40
4	20	40

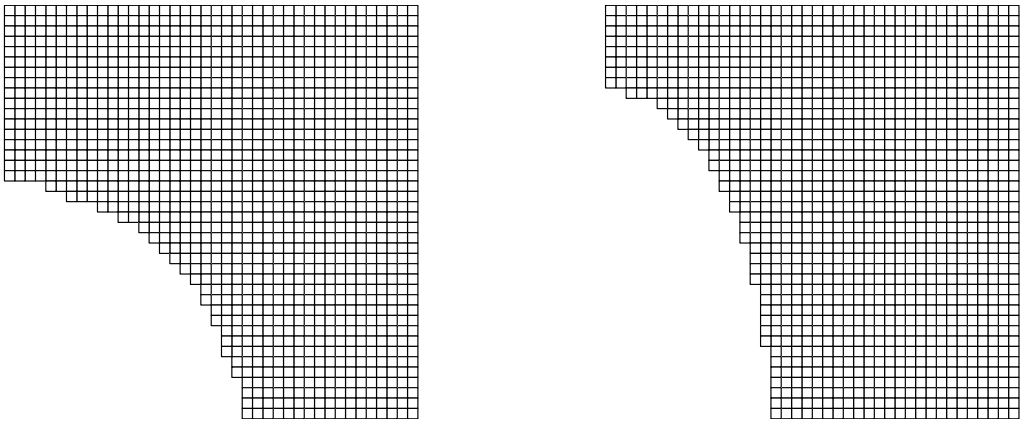

(a) Quarter circle

(b) Quarter ellipse with aspect ratio of 2

Figure 7.5 The optimum results with linear elastic material: a) for Cases 1 and 3; b) for Cases 2 and 4.

Mechanical properties of the soil material are reported in Table 7.2. Note that the optimum results with linear elastic material do not depend on the mechanical properties of the media.

Because of symmetry only one quarter of the square is modelled (the shaded area in Figure 7.4). A 3m $\times$ 3m square area at the corner of the

Table 7.2 Mechanical properties of the soil material used in the first example.

Property	Value
Modulus of elasticity	$E = 10\text{MPa}$
Poisson's ratio	$\nu = 0.3$
Cohesion	$c = 10\text{kPa}$
Friction angle	$\phi = 35^\circ$

quarter model is chosen as design domain (Fig. 7.4) and discretised using 150×150 equally sized 4-node elements. The first initial hole is created by removing one element at the corner Figure 7.6. Minimum hole area for termination of the process is set at 400 elements.

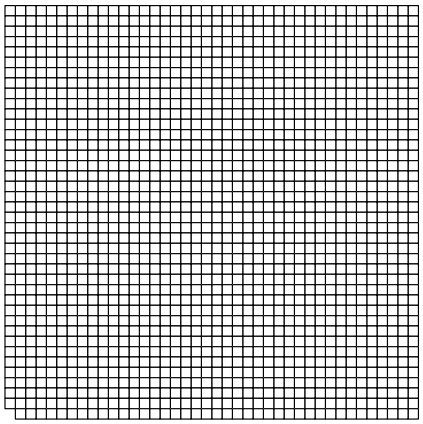

Figure 7.6 The initial shape for the first example.

Figure 7.7 illustrates the final shapes of the hole obtained by ESO for each load case. It can be seen that unlike the linear elastic case, the final shape also depends on the magnitude of the applied force. It is also notable that for lower amounts of force (Cases 1 and 2) the final shape is made of some straight lines while for greater forces (Cases 3 and 4) the shapes take arched and curved forms. It should be noted that the hole size of the obtained results, due to termination conditions, are bigger than 400 elements which

is the size of the two linear elastic optimal shapes (Fig. 7.5). The size of the hole for ESO results in Cases 1, 2, 3, and 4 are 401, 407, 409, and 404 elements respectively.

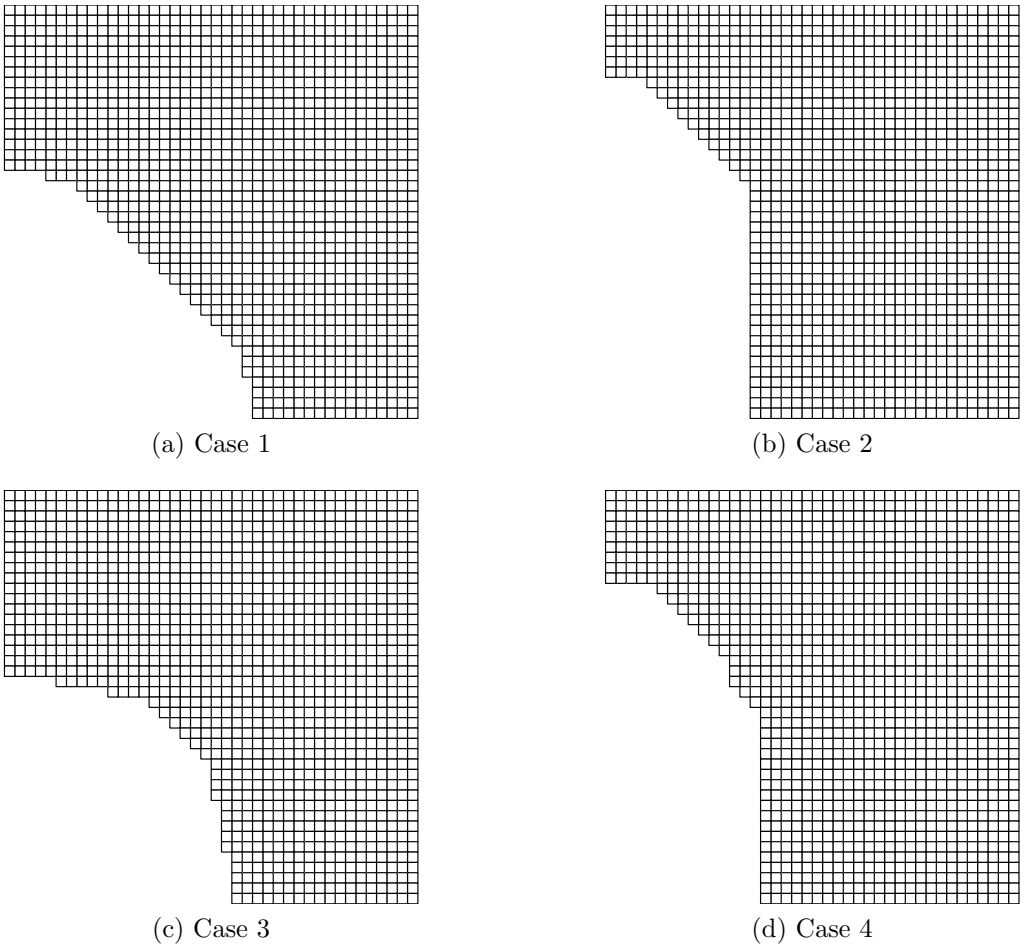

(a) Case 1 (b) Case 2

(c) Case 3 (d) Case 4

Figure 7.7 The optimum results for non-linear material obtained by the ESO method.

To compare the results, two non-linear models are made with circular and elliptical holes as shown in Figure 7.5. The inelastic responses depend on the loading path and thus the responses of the linear elastic solutions can not be compared with obtained shapes directly. In order to have a reasonable

Table 7.3 Performance index values for the first example.

Case	Linear result	ESO result	Difference
1	0.8677	0.8098 (Circle)	6.68%
2	0.7980	0.7649 (Ellipse)	4.14%
3	0.9229	0.8435 (Circle)	8.60%
4	0.9565	0.8746 (Ellipse)	8.56%

comparison all of these shapes are modelled using same elasto-plastic material and then after applying the boundary loads the complete shape is excavated all at once. Then for any of these shapes the value of the performance index is calculated. Table 7.3 reports these values.

It can be seen in Table 7.3 that the obtained results give better performance indices compared to linear optimum shapes in all cases. This can be seen as a direct verification because PI is the average of the defined efficiency in the proposed method and thus higher PI means more efficient design in this method.

7.5.2 Considering the weight of soil

The second example is a very simple and common problem: finding the best shape of an underground opening in a semi infinite media. Problem definition is sketched in Figure 7.8. Unlike the first example, the weight of materials is not neglected here. Apart from materials' self weight, there is no other load applied. The properties of the material used in this example are listed in Table 7.4. The minimum hole size for termination of the process is set at 400 elements, like the first example.

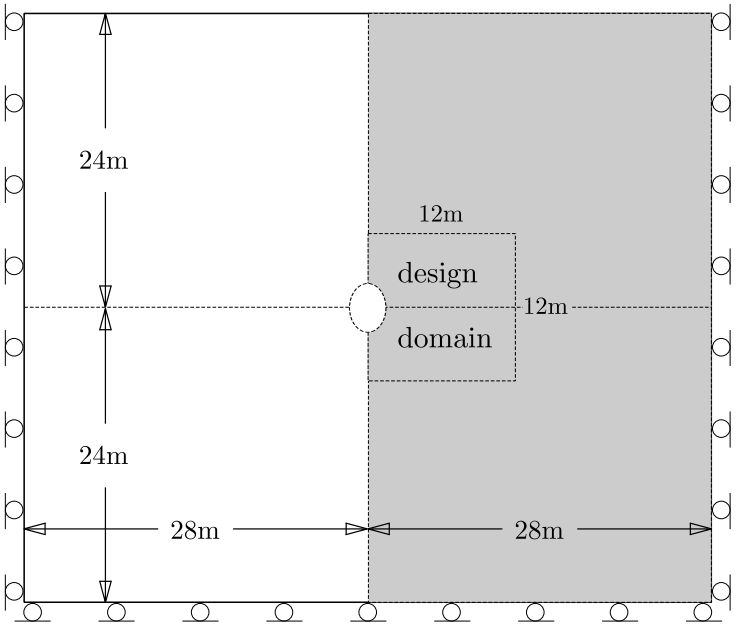

Figure 7.8 The sketch of the 2D problem used in the second example.

Table 7.4 Mechanical properties of the soil material used in the second example.

Property	Value
Modulus of elasticity	$E = 20\text{MPa}$
Poisson's ratio	$\nu = 0.4$
Cohesion	$c = 100\text{kPa}$
Friction angle	$\phi = 25^\circ$
Dry unit weight	$\gamma_d = 16\text{kN/m}^3$

Because of symmetry, only half of the area is modelled (the shaded area in Figure 7.8). The design domain is defined as a square around the initial hole of size 12m × 12m. A mesh of 100 × 100 similar sized square elements is used to discretise this domain. The initial hole consists of four elements (Fig. 7.9a).

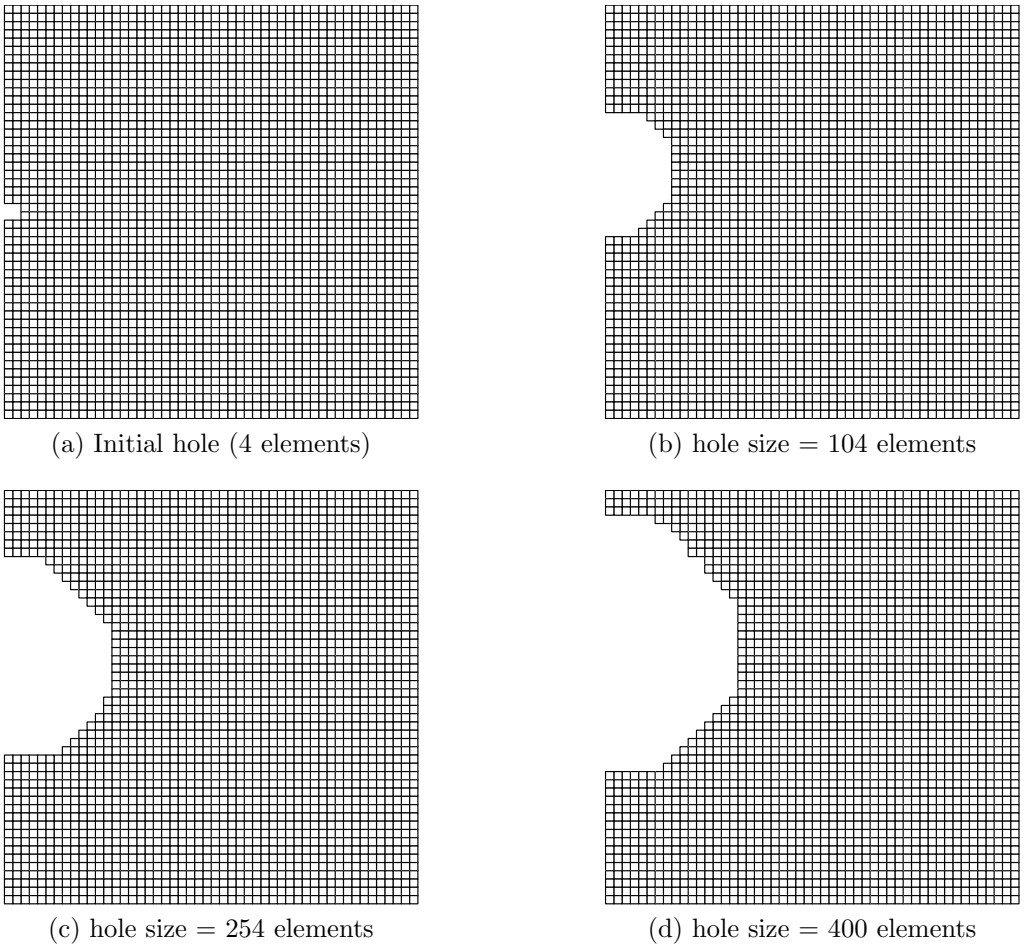

(a) Initial hole (4 elements)

(b) hole size = 104 elements

(c) hole size = 254 elements

(d) hole size = 400 elements

Figure 7.9 The initial hole and the obtained results for the second example.

Some of the shapes produced during the optimisation process are illustrated in Figure 7.9b-d. It can be seen from these illustrations that the majority of the elements were removed from the upper side of the initial

hole. This is because of the self weight loading.

7.6 Concluding remarks

The ESO procedure has been used to optimise the shape of underground openings in excavation problems. An elastic-perfectly plastic model has been used for modelling soil (and rock) behaviour based on Mohr-Coulomb yield function. A new sensitivity number formula relevant to Mohr-Coulomb yield function has been derived and has been used as the rejection criterion.

The proposed procedure has been used to solve some simple 2D problems. The obtained results have been compared with the optimum shapes of the problem in linear elastic media. Results showed that, in terms of fully stressed design (which the ESO method is based on), the proposed procedure gives better results.

It has been demonstrated that the magnitudes of applied forces affect the final design which is due to non-linear nature of the problem. Under small forces the final shapes show more of straight lines. Raising the magnitude of forces, however, makes the opening shapes smoother and more curved.

The proposed method can be easily extended to solve 3D problems. It is also possible to redefine the rejection criterion for other material models using a similar concept.

CHAPTER 8

Conclusions

In this thesis it has been tried to open a pathway on applying the state-of-the-art topology and shape optimisation techniques in shape and reinforcement design of underground excavations. These optimisation techniques have been proved useful in structural and material design. Also they have been successfully applied in a range of physical problems from heat transfer to stokes flows. However despite a great potential in underground excavation design, only few studies have been conducted to use these new optimisation techniques in this field. This thesis have taken a further step by introducing complexities like discontinuities in the ground media and using elasto-plastic material model.

The thesis involves literature review on topology optimisation techniques. Four more commonly used techniques have been presented in details. Their algorithms have been described and their applications have been illustrated by means of numerical examples.

An introduction on the rock and soil mechanics has been added. The differences between structural and excavation design have been pointed out. The potential applications of the topology optimisation techniques in excavation design have been discussed. A brief review of previous works in this

field has been also presented to complete the literature review.

A whole chapter has been devoted to tailoring a suitable topology optimisation technique to be used in excavation shape and reinforcement design. Different material interpolation schemes have been introduced and tested. The procedure to extract the sensitivity numbers from sensitivity analysis results has been discussed. The filtering scheme has been described and applied to overcome the numerical instabilities and to smoothen the results. The considerations in shape optimisation have been addressed. The steps to switch the elements to update the material distribution have been described. The mathematical background of the proposed optimisation method has been discussed. Finally, at the end of this chapter, the effects of using different material interpolations and different controlling parameters have been demonstrated through numerical examples.

The shape and reinforcement optimisation of excavations have been addressed in the following chapters starting with excavation optimisation in linear elastic homogeneous media. These assumptions limit the application of the results to intact rock or highly weathered rock massess where linear elastic model can sufficiently simulate the rock mass behaviour. The optimum shapes of tunnels have been found for some numerical examples. A post-processor algorithm has been presented based on Bézier curves to smoothen the final shapes. The results have been verified by analytical solutions in simple cases. The reinforcement optimisation has been introduced next. Three objective functions have been considered, namely the mean compliance, the floor heave, and the tunnel convergence. Some numerical examples have been solved to illustrate the optimum designs achieved by minimising each of these

objective functions. A combined shape-reinforcement optimisation problem has been formulated next. The capability of the proposed method has been tested against this mixed optimisation problem as well. Numerical examples have been solved and the results have been presented. It has been shown that the computational effort needed to solve this mixed optimisation problem is nearly the same as each of the single optimisation problems alone.

In the next step, a more complicated problem has been considered by considering discontinuities in the host rock. The presence of discontinuities falsifies the homogeneity and isotropy assumptions. However, it has been demonstrated that these simplifying assumptions can be still validated if one ensures that any possible separation and slippage is prevented along discontinuities. Based on this fact, a stabilising algorithm has been presented to stabilise the design before optimising it. The behaviour of this algorithm has been tested and verified by analytical solutions. Through some more numerical examples, the application and capabilities of the proposed method have been demonstrated. Also an introduction to multi-objective optimisation problems has been presented with illustrative examples.

Finally shape optimisation of openings in elasto-plastic soil has been considered. To simulate the excavation procedure, the ESO method has been used to tackle this problem. To bypass the difficulties of sensitivity analysis in this complex case, an intuitive efficiency measure has been formulated for Mohr-Coulomb material based on stress values. The algorithm has been described in detail. Numerical examples have been solved to demonstrate the application of the proposed method. The results have been found to be dependent on the magnitude of the in-situ stresses. A performance index has

been defined based on the definition of the rejection criterion. It has been shown that the obtained solutions result in better performance index values compared to linear elastic solutions. An example considering the soil weight has been also solved.

The problems considered in this thesis are mostly simplified cases. In practise there are many considerations and limitations which vary case to case and there are many uncertainties which limit the application and the validity of the excavation designs. However the solved examples in this thesis demonstrate that the state-of-the-art topology optimisation techniques can actually improve the shape and reinforcement design of excavations in most of the cases.

Apparently there are many details in excavation designs that were not and could not be considered in this thesis. The application of topology optimisation techniques in excavation design is still at its preliminary stages. There are many limitations to be overcome. These limitations and further improvements can be addressed in further studies.

Considering more practical material models for both ground material and reinforcement material is a possible improvement. The reinforcement optimisation in elasto-plastic media can be considered for further studies. This can be achieved by defining an intuitive sensitivity number, like the approach used in Chapter 7. For example Hoek-Brown material model can be considered to simulate the elasto-plastic rock mass media and a sensitivity number based on this material model can be extracted. Alternatively one can simplify such non-linear problems by ignoring the excavation sequence and assuming that the whole opening is excavated at once. This study can also

be extended by considering other support systems rather than grouted bolts. Further studies can concentrate on optimising the external support systems, for example the shape optimisation of the supporting steel frames. Considering a practical case study and applying topology optimisation techniques to improve the design can be the next step. Implementing other topology optimisation techniques can also be considered for further studies.

At the end the author wishes that his results can open a new field of research and ultimately the topology optimisation techniques become valuable practical tools in hand of tunnel designers.

Bibliography

Ambrosio, L. and Buttazzo, G. (1993). An optimal design problem with perimeter penalization. *Calculus of Variations and Partial Differential Equations*, 1(1):55–69.

Barton, N., Lien, R., and Lunde, J. (1974). Engineering classification of rock masses for the design of tunnel support. *Rock Mechanics*, 6(4):189–236.

Belytschko, T., Xiao, S. P., and Parimi, C. (2003). Topology optimization with implicit functions and regularization. *Topology optimization with implicit functions and regularization*, 57(8):1177–1196.

Bendsøe, M. P. (1989). Optimal shape design as a material distribution problem. *Structural Optimization*, 1(4):193–202.

Bendsøe, M. P. and Kikuchi, N. (1988). Generating optimal topologies in structural design using a homogenization method. *Computer Methods in Applied Mechanics and Engineering*, 71(2):197–224.

Bendsøe, M. P. and Kikuchi, N. (1993). Topology and generalized layout optimization of elastic structures. In Bendsoe, M. P. and Soares, C. A. M., editors, *Topology Design of Structures: Proceedings of the NATO Advanced Research Workshop on Topology Design of Structures, Sesimbra, Portugal, June 20-June 26, 1992*, pages 159–205. Kluwer Academic Publishers.

Bendsøe, M. P. and Sigmund, O. (1999). Material interpolation schemes in topology optimization. *Archive of Applied Mechanics*, 69(9-10):635–654.

Bendsøe, M. P. and Sigmund, O. (2003). *Topology Optimization - Theory, Methods, and Applications*. Springer, Berlin.

Bernaud, D., de Buhan, P., and Maghous, S. (1995). Numerical simulation of the convergence of a bolt-supported tunnel through a homogenization method. *Internationa Journal for Numerical and Analytical Methods in Geomechanics*, 19(4):267–288.

Bernaud, D., Maghous, S., de Buhan, P., and Couto, E. (2009). A numerical approach for design of bolt-supported tunnels regarded as homogenized structures. *Tunnelling and Underground Space Technology*, 24(5):533–546.

Bieniawski, Z. T. (1976). Rock mass classification in rock engineering. In Bieniawski, Z. T., editor, *Proceedings of the Symposium on Exploration for Rock Engineering*, volume 1, pages 97–106, Cape Town. A. A. Balkema.

Bieniawski, Z. T. (1989). *Engineering Rock Mass Classifications - A Complete Manual for Engineers and Geologists in Mining, Civil, and Petroleum Engineering*. John Wiley and Sons, New York.

Bourdin, B. (2001). Filters in topology optimization. *International Journal for Numerical Methods in Engineering*, 50(9):2143–2158.

Brady, B. H. G. and Brown, E. T. (2006). *Rock Mechanics for Underground Mining*. Springer, Dordrecht, The Netherlands, third edition.

Cheng, K.-T. and Olhoff, N. (1981). An investigation concerning optimal design of solid elastic plates. *International Journal of Solids and Structures*, 17(3):305–323.

Cherepanov, G. (1974). Inverse problems of a plane theory of elasticity. *Journal of Applied Mathematics and Mechanics*, 38(6):915–931. (English translation of the Russian Prikladnaya Matematika i Mekhanika 1974, 38(6):963–979).

Cherkaev, A., Grabovsky, Y., Movchan, A. B., and Serkov, S. K. (1998). The cavity of the optimal shape under the shear stresses. *International Journal of Solids and Structures*, 35(33):4391–4410.

Chu, D. N., Xie, Y. M., Hira, A., and Steven, G. P. (1996). Evolutionary structural optimization for problems with stiffness constraints. *Finite Elements in Analysis and Design*, 21(4):239–251.

Coulomb, C. A. (1773). Essai sur une application des régles de maximis et minimis à quelques problémes de statique relatifs à l'architecture. *Mémoires de mathématiques et de physique présentés à l'Académie royale des sciences par divers savants, et lus sans ses assemblées*, 7:343–382.

Craig, R. F. (2004). *Craig's Soil Mechanics*. Spon Press, London, 7th edition.

Culmann, K. (1866). *Die graphische Statik*. Mayer und Zeller, Zürich.

Deere, D. U., Hendron, A. J., J., Patton, F. D., and Cording, E. J. (1967). Design of surface and near-surface construction in rock. In Fairhurst, C., editor, *Failure And Breakage Of Rock - Eighth Symposium On Rock Mechanics*, pages 237–302, New York. Soc. Min. Engineers Am. Inst. Min. Metall. Petrolm Engrs.

Díaz, A. and Sigmund, O. (1995). Checkerboard patterns in layout optimization. *Structural Optimization*, 10(1):40–45.

Eschenauer, H. A. and Olhoff, N. (2001). Topology optimization of continuum structures: A review. *Applied Mechanics Reviews*, 54(4):331–390.

Ford, K. W. (1991). The large and the small. In Ferris, T., editor, *The world treasury of physics, astronomy, and mathematics*. Little, brown and company, New York. originally appeared in author's book *The World of Elementary Particles* published in 1963.

Fujii, D. and Kikuchi, N. (2000). Improvement of numerical instabilities in topology optimization using the slp method. *Structural and Multidisciplinary Optimization*, 19(2):113–121.

Ghabraie, K. (2005). Topology optimization of 2d continuous structures. Master's thesis, University of Tehran. In Persian.

Ghabraie, K., Xie, Y. M., and Huang, X. (2008). Shape optimization of underground excavation using ESO method. In Xie, Y. M. and Patnaikuni, I., editors, *Innovations in Structural Engineering and Construction: Proceedings of the 4th International Structural Engineering and ConstructiomConference (ISEC-4), 26-28 Sep. 2007, Melbourne, Australia*, pages 877–882, London. Taylor and Francis.

Greber, H. (1966). The philosophy of engineering. *IEEE Spectrum*, 3(10):112–115.

Guest, J. K., Prévost, and Belytschko, T. (2004). Achieving minimum length scale in topology optimization using nodal design variables and projection functions. *International Journal for Numerical Methods in Engineering*, 61(2):238–254.

Haber, R. B., Jog, C. S., and Bendsøe, M. P. (1996). A new approach to variable-topology shape design using a constraint on perimeter. *Structural Optimization*, 11(1–2):1–12.

Hassani, B. and Hinton, E. (1998a). A review of homogenization and topology optimization I - homogenization theory for media with periodic structure. *Computers and Structures*, 69(6):707–717.

Hassani, B. and Hinton, E. (1998b). A review of homogenization and topology optimization II - analytical and numerical solution of homogenization equations. *Computers and Structures*, 69(6):719–738.

Hassani, B. and Hinton, E. (1998c). A review of homogenization and topology optimization III - topology optimization using optimality criteria. *Computers and Structures*, 69(6):739–756.

Hassani, B. and Hinton, E. (1999). *Homogenization and Structural Topology Optimization - Theory, Practice and Software*. Springer, New York.

Herskovits, J. (1995). *Advances in Structural Optimization*, chapter "A view on nonlinear optimization", pages 71–116. Kluwer Academic Publishers, Holland.

Hinton, E. and Sienz, J. (1995). Fully stressed topological design of structures using an evolutionary procedure. *Engineering Computations*, 12(3):229–244.

Hoek, E. and Brown, E. T. (1980). *Underground Excavations in Rock*. The Institution of Mining and Metallurgy, London.

Hoek, E., Kaiser, P. K., and Bawden, W. F. (1997). *Support of Underground Excavations in Hard Rock*. A. A. Balkema, Rotterdam, the Netherlands.

Hoek, E., Wood, D., and Shah, S. (1992). A modified hoek-brown failure criterion for jointed rock masses. In Hudson, J. A., editor, *ISRM Symposium: Eurock 92 - Proceedings of the International ISRM Symposium on Rock Characterization*, pages 209–214, London. British Geotechnical Society.

Huang, X. and Xie, Y. M. (2007). Convergent and mesh-independent solutions for the bi-directional evolutionary structural optimization method. *Finite Elements in Analysis and Design*, 43(14):1039–1049.

Huang, X. and Xie, Y. M. (2009). Bi-directional evolutionary topology optimization of continuum structures with one or multiple materials. *Computational Mechanics*, 43(3):393–401.

Huang, X., Xie, Y. M., and Burry, M. C. (2006). A new algorithm for bi-directional evolutionary structural optimization. *Japan Society of Mechanical Engineers International Journal Series C*, 49(4):1091–1099.

Hudson, J. A. and Harrison, J. P. (1997). *Engineering Rock Mechanics - An Introduction to the Principles*. Pergamon, Oxford, UK.

Jáky, J. (1944). A nyugalmi nyomás tényezöje (the coefficient of earth pressure at rest). *Magyar Mérnok és Epitész Egylet Közlönye (Journal for Society of Hungarian Architects and Engineers)*, 78(22):355–358.

Jang, G.-W., Jeong, J. H., Kim, Y. Y., Sheen, D., Park, C., and Kim, M.-N. (2003). Checkerboard-free topology optimization using non-conforming finite elements. *International Journal for Numerical Methods in Engineering*, 57(12):1717–1735.

Jing, L. (2003). A review of techniques, advances and outstanding issues in numerical modelling for rock mechanics and rock engineering. *International Journal of Rock Mechanics and Mining Sciences*, 40(3):283–353.

Jing, L. and Hudson, J. A. (2002). Numerical methods in rock mechanics. *International Journal of Rock Mechanics and Mining Sciences*, 39(4):409–427.

Jog, C. S. and Haber, R. B. (1996). Stability of finite element models for distributed-parameter optimization and topology design. *Computer Methods in Applied Mechanics and Engineering*, 130(3-4):203–226.

Karush, W. (1939). Minima of functions of several variables with inequalities as side constraints. Master's thesis, Department of Mathematics, University of Chicago, Chicago, Illinois.

Kempfert, H.-G. and Gebreselassie, B. (2006). *Excavations and Foundations in Soft Soils*. Springer, The Netherlands.

Kim, H., Querin, O. M., Steven, G. P., and Xie, Y. M. (2000). A method for varying the number of cavities in an optimized topology using evolutionary structural optimization. *Structural and Multidisciplinary Optimization*, 19(2):140–147.

Kim, H., Querin, O. M., Steven, G. P., and Xie, Y. M. (2003). Improving efficiency of evolutionary structural optimization by implementing fixed grid mesh. *Structural and Multidisciplinary Optimization*, 24(6):441–448.

Kohn, R. V. and Strang, G. (1986). Optimal design and relaxation of variational problems, I, II, III. *Communications on Pure and Applied Mathematics*, 39(1–3):113–137, 139–182, 353–377.

Kuhn, H. W. and Tucker, A. W. (1951). Nonlinear programming. In *Proceedings of 2nd Berkeley Symposium*, pages 481–492, Berkeley. University of California Press.

Le Ricolais, R. (1973). quoted in: *Structures, Implicit and Explicit, Interviews with Robert Le Ricolais*. VIA, University of Pennsylvania.

Li, Q., Steven, G. P., Querin, O. M., and Xie, Y. M. (1999a). Evolutionary shape optimization for stress minimization. *Mechanics Research Communications*, 26(6):657–664.

Li, Q., Steven, G. P., and Xie, Y. M. (1999b). On equivalence between stress criterion and stiffness criterion in evolutionary structural optimization. *Structural Optimization*, 18(1):67–73.

Li, Q., Steven, G. P., and Xie, Y. M. (2001). A simple checkerboard suppression algorithm for evolutionary structural optimization. *Structural and Multidisciplinary Optimization*, 22(3):230–239.

Liu, Y., Jin, F., Li, Q., and Zhou, S. (2008). A fixed-grid bidirectional evolutionary structural optimization method and its applications in tunnelling engineering. *International Journal for Numerical Methods in Engineering*, 73(12):1788–1810.

Lurie, K. A., Cherkaev, A. V., and Fedorov, A. V. (1982). Regularization of optimal design problems for bars and plates, I, II. *Journal of Optimization Theory and Applications*, 37(4):499–522, 523–543.

Matsui, K. and Terada, K. (2004). Continuous approximation of material distribution for topology optimization. *International Journal for Numerical Methods in Engineering*, 59(14):1925–1944.

Mayne, P. W. and Kulhawy, F. H. (1982). K_o - OCR relationships in soil. *Journal of the Geotechnical Engineering Division, ASCE*, 108(6):851–872.

Michell, A. G. M. (1904). The limits of economy of material in frame structures. *Philosophical Magazine*, ser. 6, 8:589–597.

Mitchell, J. K. and Soga, K. (2005). *Fundamentals of Soil Behavior*. John Wiley and Sons, New Jersey, 3rd edition.

Pahl, G. and Beitz, W. (1988). *Engineering Design: A Systematic Approach*. Design Council/Springer-Verlag, London. Translated from German by A. Pomerans and K. Wallace.

Pedersen, P. (2000). On optimal shapes in materials and structures. *Structural and Multidisciplinary Optimization*, 19(3):169–182.

Petersson, J. and Sigmund, O. (1998). Slope constrained topology optimization. *International Journal for Numerical Methods in Engineering*, 41(8):1417–1434.

Poulsen, T. A. (2002). A simple scheme to prevent checkerboard patterns and one-node connected hinges in topology optimization. *Structural and Multidisciplinary Optimization*, 24(5):396–399.

Prager, W. (1969). Optimality criteria derived from classical extermum principles. Technical report, SM Studies Series, Solid Mechanics Division, University of Waterloo, Ontario, Canada.

Prager, W. (1974). A note on discretized michell structures. *Computer Methods in Applied Mechanics and Engineering*, 3(3):349–355.

Querin, O. M. (1997). *Evolutionary Structural Optimisation Stress Based Formulation and Implementation*. Ph.D. thesis, Department of Aeronautical Engineering, University of Sydney, Sydney, Australia.

Querin, O. M., Steven, G. P., and Xie, Y. M. (1998). Evolutionary structural optimisation ("eso") using a bidirectional algorithm. *Engineering Computations*, 15(8):1031–1048.

Querin, O. M., Young, V., Steven, G. P., and Xie, Y. M. (2000). Computational efficiency and validation of bi-directional evolutionary structural optimisation. *Computer Methods in Applied Mechanics and Engineering*, 189(2):559–573.

Rahmatalla, S. F. and Swan, C. C. (2004). A Q4/Q4 continuum structural topology optimization implementation. *Structural and Multidisciplinary Optimization*, 27(1–2):130–135.

Rao, S. S. (1996). *Engineering Optimization - Theory and Practice*. John Wiley and Sons, New York, 3rd edition.

Ren, G., Smith, J. V., Tang, J. W., and Xie, Y. M. (2005). Underground excavation shape optimization using an evolutionary procedure. *Computers and Geotechnics*, 32(2):122–132.

Rozvany, G. I. N. (1972a). Grillages of maximum strength and maximum stiffness. *International Journal of Mechanical Sciences*, 14(10):651–666.

Rozvany, G. I. N. (1972b). Optimal load transmission by flexure. *Computer Methods in Applied Mechanics and Engineering*, 1(3):253–263.

Rozvany, G. I. N. (2001). Aims, scope, methods, history and unified terminology of computer-aided topology optimization in structural mechanics. *Structural and Multidisciplinary Optimization*, 21(2):90–108.

Rozvany, G. I. N. and Prager, W. (1976). Optimal design of partially discretized grillages. *Journal of the Mechanics and Physics of Solids*, 24(2–3):125–136.

Rozvany, G. I. N., Zhou, M., and Birker, T. (1992). Generalized shape optimization without homogenization. *Structural Optimization*, 4(3-4):250–252.

Sigmund, O. (1994). *Design of material structures using topology optimization*. Ph.D. thesis, Department of Solid Mechanics, Technical University of Denmark, Lyngby, Denmark.

Sigmund, O. (1997). On the design of compliant mechanisms using topology optimization. *Mechanics Based Design of Structures and Machines*, 25(4):493–524.

Sigmund, O. (2001). A 99 line topology optimization code written in matlab. *Structural and Multidisciplinary Optimization*, 21(2):120–127.

Sigmund, O. and Petersson, J. (1998). Numerical instabilities in topology optimization: A survey on procedures dealing with checkerboards, mesh-dependencies and local minima. *Structural and Multidisciplinary Optimization*, 16(1):68–75.

Stolpe, M. and Svanberg, K. (2001). An alternative interpolation scheme for minimum compliance topology optimization. *Structural and Multidisciplinary Optimization*, 22(2):116–124.

Suzuki, K. and Kikuchi, N. (1991). A homogenization method for shape and topology optimization. *Computer Methods in Applied Mechanics and Engineering*, 93(3):291–318.

Tanskanen, P. (2002). The evolutionary structural optimization method: theoretical aspects. *Computer Methods in Applied Mechanics and Engineering*, 191(47-48):5485–5498.

Terzaghi, K. (1936). quoted in: Goodman, R. E. (1999). *Karl Terzaghi - The Engineer as Artist*. American Society of Civil Engineers (ASCE Press), Reston, VA.

Terzaghi, K., Peck, R. B., and Mesri, G. (1996). *Soil Mechanics in Engineering Practice*. John Wiley and Sons, New York.

Wang, M. Y., Wang, X., and Guo, D. (2003). A level set method for structural topology optimization. *Computer Methods in Applied Mechanics and Engineering*, 192(1-2):227–246.

Xie, Y. M. and Steven, G. P. (1993). A simple evolutionary procedure for structural optimization. *Computers & Structures*, 49(5):885–896.

Xie, Y. M. and Steven, G. P. (1997). *Evolutionary structural optimization*. Springer, London.

Yang, X. Y., Xie, Y. M., Liu, J. S., Parks, G. T., and Clarkson, P. J. (2003). Perimeter control in the bidirectional evolutionary optimization method. *Structural and Multidisciplinary Optimization*, 24(6):430–440.

Yang, X. Y., Xie, Y. M., Steven, G. P., and Querin, O. M. (1999). Bidirectional evolutionary method for stiffness optimization. *American Institute of Aeronautics and Astronautics Journal*, 37(11):1483–1488.

Yin, L. and Yang, W. (2000a). Topology optimization for tunnel support in layered geological structures. *International Journal for Numerical Methods in Engineering*, 47(12):1983–1996.

Yin, L. and Yang, W. (2000b). Topology optimization to prevent tunnel heaves under different stress biaxialities. *International Journal for Numerical and Analytical Methods in Geomechanics*, 24(9):783–792.

Yin, L., Yang, W., and Guo, T. (2000). Tunnel reinforcement via topology optimization. *International Journal for Numerical and Analytical Methods in Geomechanics*, 24(2):201–213.

Yu, H.-S. (2000). *Cavity Expansion Methods in Geomechanics*. Kluwer Academic Publishers, Dordrecht.

Yu, H.-S. (2006). *Plasticity and Geotechnics*, volume 13 of *Advances in Mechanics and Mathematics*. Springer, New York.

Yulin, M. and Xiaoming, W. (2004). A level set method for structural topology optimization and its applications. *Advances in Engineering Software*, 35(7):415–441.

Zhang, L. (2005). *Engineering Properties of Rocks*, volume 4 of *Elsevier geo-engineering book series*. Elsevier, London.